Multiscale modeling of metal additive manufacturing: Investigation into dendritic solidification, meltpool dynamics, and microstructure evolution

by

Kunal Bhagat

A dissertation submitted in partial fulfillment of
the requirements for the degree of

Doctor of Philosophy

(Mechanical Engineering)

at the

UNIVERSITY OF WISCONSIN–MADISON

2023

Date of final oral examination: 05/15/2023

The dissertation is approved by the following members of the Final Oral Committee:

Shiva Rudraraju, Assistant Professor, Mechanical Engineering (chair)
Dan Thoma, Professor, Material Science and Engineering
Krishnan Suresh, Professor, Mechanical Engineering
Lianyi Chen, Associate Professor, Mechanical Engineering
Jiamian Hu, Assistant Professor, Material Science Engineering

To mummy and papa

ACKNOWLEDGMENTS

I am indebted to the University of Wisconsin-Madison for providing an opportunity to conduct my doctoral research. Very grateful to my advisor Shiva Rudraraju for giving me a chance to work on wide-ranging research problems. I express my gratitude to our collaborator Prof. Dan Thoma and his research group for critical discussions and experimental data support. I am thankful to the PhD committee members for their valuable time, and constructive feedback. The numerical and computational component of my research work wouldn't have been possible without super-computing infrastructure and support provided by the Center for High Throughput Computing, compphys, and mighty "gandalf"- our lab cluster. I am thankful to my peers in CMMG groups for their valuable help in professional and personal capacities. Huge shout-out to friends to help me get through the thick and thins of my doctoral journey, uncertain pandemic, and lockdown. Much obliged to my mentors for their support, feedback, and mentorship at different stages of my career.

— Kunal Bhagat

CONTENTS

LIST OF TABLES

LIST OF FIGURES

MULTISCALE MODELING OF METAL ADDITIVE MANUFACTURING: INVESTIGATION INTO DENDRITIC SOLIDIFICATION, MELTPOOL DYNAMICS, AND MICROSTRUCTURE EVOLUTION

Kunal Bhagat

Under the supervision of Professor Shiva Rudraraju
At the University of Wisconsin-Madison

Microstructure evolution in metal additive manufacturing (AM) is a complex multi-physics and multi-scale problem. Understanding the impact of AM process conditions on the microstructure evolution and the resulting mechanical properties of the printed part is an active area of research. The investigation into understanding the microstructure evolution under AM conditions, at different length scales, is done as a three-part research program that is presented in this thesis.

In the first part, a high-fidelity numerical method at the mesoscale to model varied dendritic solidification morphologies is developed. A numerical framework encompassing the modeling of Stefan problem formulations relevant to dendritic evolution using a phase-field approach and a finite element method implementation is presented. Using this framework, numerous complex dendritic morphologies that are physically relevant to the solidification of pure melts and binary alloys are modeled. To the best of our knowledge, this is a first-of-its-kind study of numerical convergence of the phase-field equations of dendritic growth in a finite element method setting. Further, using this numerical framework, various types of physically relevant dendritic solidification patterns like single equiaxed, multi-equiaxed, single-columnar, and multi-columnar dendrites are modeled in two-dimensional and three-dimensional computational domains.

In the second part, the complex dynamics of meltpool formation during metal additive manufacturing are modeled using a thermo-fluidic numerical model. Statistical-based method of least-squares is exploited to characterize the role of dimensional numbers in the microstructure evolution process. A novel strategy using dimensional analysis and the method of linear least-squares regression to numerically investigate the thermo-fluidic governing equations of the Laser Powder Bed Fusion AM process is presented. First, the governing equations are solved using the finite element method, and the model predictions are validated with experimental and numerical results from the literature. Then, through dimensional analysis, an important dimensionless quantity - interpreted as a measure of heat absorbed by the powdered material and the meltpool, is identified. Key contributions of this work include the demonstration of the correlation between the dimensionless measure of heat absorbed, and classical dimensionless quantities such as Péclet, Marangoni, and Stefan numbers, with advective transport in the meltpool for different alloys, meltpool morphologies, and microstructure evolution-related variables

In the third part, the influence on the morphology of evolving dendritic microstructure due to the rapid thermal cycle and fluid convection in the meltpool during metal additive manufacturing is investigated. A finite-element formulation that solves a coupled Navier-Stokes flow model and a phase-field model of dendritic solidification is developed. Microstructure evolution modeled using purely heat and mass diffusion process may not capture the entire spectrum of the dendrite morphology observed in metal additive manufacturing. The impact of flow dynamics on the thermal gradients and momentum transfer that modulate dendritic shapes, along with the associated remelting are modeled using a coupled phase-field model of solidification. Further, the morphological changes to dendrites in the solidifying region beneath the meltpool fusion line are modeled by accounting for convective effects in the mass and heat diffusion process

in equiaxed, aligned equiaxed, and columnar dendrite growth for a pure metal and binary alloys. It is observed that for a meltpool formed under high laser power and scan speed conditions, where Marangoni convection is significant, enhanced growth of the secondary arms of columnar dendrite occurs as compared to dendrite growth observed in low convection regions of the meltpool.

Shiva Rudraraju

ABSTRACT

Microstructure evolution in metal additive manufacturing (AM) is a complex multi-physics and multi-scale problem. Understanding the impact of AM process conditions on the microstructure evolution and the resulting mechanical properties of the printed part is an active area of research. The investigation into understanding the microstructure evolution under AM conditions, at different length scales, is done as a three-part research program that is presented in this thesis.

In the first part, a high-fidelity numerical method at the mesoscale to model varied dendritic solidification morphologies is developed. A numerical framework encompassing the modeling of Stefan problem formulations relevant to dendritic evolution using a phase-field approach and a finite element method implementation is presented. Using this framework, numerous complex dendritic morphologies that are physically relevant to the solidification of pure melts and binary alloys are modeled. To the best of our knowledge, this is a first-of-its-kind study of numerical convergence of the phase-field equations of dendritic growth in a finite element method setting. Further, using this numerical framework, various types of physically relevant dendritic solidification patterns like single equiaxed, multi-equiaxed, single-columnar, and multi-columnar dendrites are modeled in two-dimensional and three-dimensional computational domains.

In the second part, the complex dynamics of meltpool formation during metal additive manufacturing are modeled using a thermo-fluidic numerical model. Statistical-based method of least-squares is exploited to characterize the role of dimensional numbers in the microstructure evolution process. A novel strategy using dimensional analysis and the method of linear least-squares regression to numerically investigate the thermo-fluidic governing equations of the Laser Powder Bed Fusion AM

process is presented. First, the governing equations are solved using the finite element method, and the model predictions are validated with experimental and numerical results from the literature. Then, through dimensional analysis, an important dimensionless quantity - interpreted as a measure of heat absorbed by the powdered material and the meltpool, is identified. Key contributions of this work include the demonstration of the correlation between the dimensionless measure of heat absorbed, and classical dimensionless quantities such as Péclet, Marangoni, and Stefan numbers, with advective transport in the meltpool for different alloys, meltpool morphologies, and microstructure evolution-related variables

In the third part, the influence on the morphology of evolving dendritic microstructure due to the rapid thermal cycle and fluid convection in the meltpool during metal additive manufacturing is investigated. A finite-element formulation that solves a coupled Navier-Stokes flow model and a phase-field model of dendritic solidification is developed. Microstructure evolution modeled using purely heat and mass diffusion process may not capture the entire spectrum of the dendrite morphology observed in metal additive manufacturing. The impact of flow dynamics on the thermal gradients and momentum transfer that modulate dendritic shapes, along with the associated remelting are modeled using a coupled phase-field model of solidification. Further, the morphological changes to dendrites in the solidifying region beneath the meltpool fusion line are modeled by accounting for convective effects in the mass and heat diffusion process in equiaxed, aligned equiaxed, and columnar dendrite growth for a pure metal and binary alloys. It is observed that for a meltpool formed under high laser power and scan speed conditions, where Marangoni convection is significant, enhanced growth of the secondary arms of columnar dendrite occurs as compared to dendrite growth observed in low convection regions of the meltpool.

1 INTRODUCTION

Dendritic solidification and phase-field method

Dendrites are tree-like patterns with complex multi-level branch structures that are observed across a wide spectrum of physical phenomena - from snow flakes to river basins; from bacterial colonies to lungs and vascular systems; and ubiquitously in solidification and growth patterns in metals and crystals. In the context of solidification problems involving a pure metal or metallic alloys, dendritic "trees" with primary and secondary branches grow from a nucleation point or a field perturbation. These solidification dendrites often initiate at random nucleation points or at domain boundaries at the initial stage, followed by anisotropic interface growth during the intermediate stage, eventually leading to grain formation and coarsening. The theoretical foundations of dendritic solidification lie in the classical Stefan problem, a moving boundary problem, that describes the evolution of a solid-liquid phase front (Rubinstein, 1971). The two-phase interface motion is obtained by solving the heat equation in each phase, coupled with an evolving interface boundary condition (Stefan condition) that explicitly sets the velocity of the moving interface. While the evolution of dendrites in pure melts with no dissolved solutes is well represented by the Stefan problem, for melts with dissolved solutes (like alloys), mass diffusion in the constituent phases should also be accounted for in the governing equations.

Many analytical and numerical approaches exist for treating the Stefan problem, albeit under various simplifying assumptions on the problem geometry, interface geometry and boundary conditions. In the numerical domain, front tracking methods (Meyer, 1978; Marshall, 1986) are useful in solving straight and curved interface evolution in one-dimensional problems. Other popular methods that explicitly track moving interface are the Landau transformation and the finite element mesh-based moving

node techniques. These methods are more suited when the movement of the interface is not far from the initial position (Dantzig and Rappaz, 2016), but bookkeeping of the interface movement can be an arduous task, especially for anisotropic interphase growth conditions. The level set method is another popular numerical technique that is extensively used to solve moving interface problems, including dendrite solidification using the Stefan problem (Chen et al., 1997).

The phase-field method has gained popularity in the last two decades as an alternate diffuse interface numerical technique to model solidification processes. The phase-field model modifies the equations represented by the Stefan problem by introducing an order parameter to distinguish between the solid and liquid phases. Further, the previously sharp interface is represented as a diffuse interface using this order parameter without sacrificing much of the accuracy. The earliest of the simplified isotropic phase-field model has been proposed by Fix (1983), and Collins and Levine (1985). Caginalp (1986, 1989) and Kobayashi (1993) introduced basic anisotropy into the phase-field model and numerically predicted dendritic patterns seen in the solidification of the pure melt. They also modeled the formation of the side branching by introducing noise into the phase-field models.

The potential of the so far surveyed phase-field models was limited due to constraints on the lattice size, undercooling, interface width, capillary length, and interface kinetics. A modified thin interface phase-field model proposed by Karma and Rappel (1996) overcame these limitations. The dendrite shape and tip velocities of the pure melt obtained from the thin interface phase-field model were in excellent agreement with the steady-state results reported in theoretical studies. Karma and Rappel (1999) studied dendrite side-branching by introducing a microscopic thermal noise, and the side branch characteristics were in line with the linear WKB theory based stability analysis. (Plapp and Karma, 2000) proposed a hybrid

technique where the phase-field model and diffusion-based Monte-Carlo algorithm were used in conjunction to simulate dendritic solidification at the low undercooling in two and three-dimensional geometry.

The phase-field model for the solidification of a binary alloy was presented by Warren and Boettinger (1995). Realistic patterns showing the primary and the secondary arms of the dendrite were simulated using the interface thickness far different from the asymptotic limit of the sharp interface models. Loginova et al. (2001) was the first to include the non-isothermal effects in binary alloy solidification. However, the computations were time-consuming. An artificial solute trapping was observed in the simulations with higher undercooling. This artificial solute trapping was the result of diffuse interface thickness. Karma (2001) developed a modified thin interface phase-field model for alloy solidification. Compared to the previous models, this model was applicable for varied interface thicknesses, zero non-equilibrium effects at the interface, and nearly zero diffusivity in the solid.

The thin interface phase-field model by Ramirez et al. (2004) considered both heat and solute diffusion along with zero kinetics at the interface. The interface thickness used was an order of magnitude less than the radius of curvature of the interface. Echebarria et al. (2004) modeled numerous numerical test cases and studied the convergence of the thin interface phase-field model. They discussed the final form of anti-trapping current that is often used in many alloy solidification models (Karma, 2001; Ramirez et al., 2004; Almgren, 1999). When the solid diffusivity of the alloys is non-negligible, the form of anti-trapping current previously used needs modification and this was rigorously derived in the work of Ohno and Matsuura (2009)

With the substantial review tracing Stefan problem and important theoretical development of the phase-field model, we review literature focusing on the numerical implementations of these models and error

analysis. Several important studies leveraged the finite-element and finite-difference method based numerical schemes and their application to the phase-field model of solidification. These studies focused on the accuracy and stability of proposed numerical schemes. In this regard, the work of Feng and Prohl (2004) is important. They made use of fully discrete finite element methods and obtained optimal error bounds in relation to the interface thickness for a phase-field method of solidification. Using the error estimates they showed convergence of finite element schemes to the solution to the phase field models in the limit of the sharp interface. Gonzalez-Ferreiro et al. (2014) presented a finite element discretization in space and mid-point discretization in time of a phase-field model that is consistent with both the thermodynamics laws. The thermodynamically consistent numerical model was developed to have better dendrite resolution and higher order accuracy in time. A first-order accurate in time and energy stable numerical method was presented by Chen and Yang (2019). The proposed method was applied to coupled Allen-Cahn, heat diffusion, and modified Navier-Stokes equations. They resort to techniques that decoupled these three equations with the use of implicit-explicit schemes in their numerical implementation.

Better spatial and temporal accuracy and smaller error estimates were reported in the work of Kessler and Scheid (2002). They applied a finite element method to the phase-field model of binary alloy solidification where the error convergence numerical tests were done on a physical example of Ni-Cu alloy solidification with a simpler and non-branched solidification structure. The adaptive meshing technique was used in many numerical studies of solidification using a phase-field model. Hu et al. (2009) presented a multi-mesh adaptive finite-element based numerical scheme to solve the phase-field method for the pure-melt solidification problem. The accuracy of their method was tested with its ability to predict dendrite tip velocities with a range of undercooling conditions. Work of Rosam

et al. (2007) using the mesh and time adaptive fully implicit numerical scheme utilizing finite-difference method applied to binary alloy solidification is very relevant. Such highly space-time adaptive techniques saved computational time. Their focus was on the implicit and explicit schemes error estimates using only derived variables such as dendrite tip position, radius, and velocity. However, error analysis reported in the literature did not explore the effect of basis continuity (i.e, C^n-continuous basis) on capturing dendrite kinetics and morphologies, and the convergence studied reported did not explicitly study the error in the primal fields, i.e., temperature and phase-field order parameter. As part of this research, these two aspects of error analysis will also be addressed.

A review by Tourret et al. (2022) highlights several studies that applied the phase-field methods to model solidification and obtained good comparisons with the experimental results. Present challenges and extensions of phase-field models were also discussed in their review. Wang et al. (2012) discovered the relation between lower and upper limit primary dendrite arm spacing to inter-dendritic solute distribution and inter-dendritic undercooling by solving phase-field models using finite-element method. Fallah et al. (2012) work showed the suitability of phase-field models coupled with heat transfer models to reproduce experimentally known complex dendrite morphology and accurate dendrite size of Ti-Nb alloys thereby demonstrating the suitability of the numerical methods to laser deposition and industrial scale casting process. More recently, microstructure evolution processes involving competitive grain growth of columnar dendrites and the grain growth along the converging grain boundary were modeled using the phase-field model by Tourret and Karma (2015), and Takaki et al. (2014). In manufacturing processes like welding and molding, phase-field models were used to study solidification cracking susceptibility in Al-Mg alloys by Geng et al. (2018), and dendrite morphology in the melt pool of Al-Cu alloys by Farzadi et al. (2008). Integrated

phase-field model and finite element methods are also used to study microstructure evolution especially formation of laves phase in additive manufacturing of IN718 Wang et al. (2019a). Phase-field models finds extensive applications in modeling rapid solidification conditions prevalent in the metal additive manufacturing Rolchigo et al. (2017); Ghosh et al. (2017); Gong and Chou (2015); Sahoo and Chou (2016); Keller et al. (2017).

A lot of existing studies on solidification and related phase-field models have focused only on either pure metals or alloys. However, in this work, unified treatment of both pure metals and alloys is presented in Chapter 2. A classical Stefan problems relevant to both these types of solidification is discussed, and their phase-field formulations and numerical implementations is presented. Further, novel numerical error estimates of dendritic tip velocity, and the convergence of error for the primal fields of temperature and order parameter with respect to the numerical discretization are also obtained. Lastly, using this numerical framework, various types of physically relevant dendritic solidification patterns like single equiaxed, multi-equiaxed, single columnar and multi-columnar dendrites are modeled in two-dimensional and three-dimensional computational domains.

Thermo-fluidic meltpool dynamics and dimensionless numbers

Additive manufacturing (AM) has proven to be a path-breaking manufacturing paradigm that has the potential to disrupt many of the traditional reductive-type manufacturing processes (Huang et al., 2015). A wide variety of AM techniques, suitable for printing metals, glasses, ceramics, and polymers (Gibson et al., 2021), are in use today and an optimal AM technique can be selected depending on the material, part complexity and design considerations (Konda Gokuldoss et al., 2017).Laser Powder Bed Fusion (LPBF) process of AM is the central focus of this work. This technique is widely used to print metallic components with intricate geometry

to their near-net shape. Components printed using the LPBF process have the potential to exhibit improved material properties as compared to the traditional manufacturing process. In particular, additively manufactured hierarchical stainless steels are not limited by strength-ductility tradeoff unlike traditionally manufactured stainless steel (Wang et al., 2018). Tensile and fatigue properties of additively built Ti-6Al-4V were shown to be superior to mill-annealed Ti-6Al-4V (Qian et al., 2016). However, the properties of the printed components are very sensitive to the choice of the LPBF process parameters and the execution of the printing process. Realization of the full potential of AM is not possible unless optimized process parameters can be identified for various alloys used in laser-based additive manufacturing (Rittinghaus et al., 2022).

The LPBF manufacturing technique is a multi-stage process. Initially, a moving blade of polymer edge (recoater) spreads a metal powder forming a layer of uniform thickness. A high-energy laser moves over a powder layer bed in a predefined path. This results in a localized melting of the powder metal followed by rapid cooling and fusion of melted powder material on the previously built part. A new layer of the powder is then deposited and the process repeats until the desired part is printed in a layer-by-layer fashion (Gibson et al., 2021). This multi-stage additive printing process involves melting and solidification of the material, formation of the localized meltpool, convection cells inside the pool, keyhole formation, improper fusion of the powder, building up of the residual stresses, and sometimes unwanted material deformation, etc. (King et al., 2015). Existing literature is focused on understanding the effects of additive process parameters on the properties of experimentally printed components such as the surface roughness of overhang structures (Fox et al., 2016), bead geometry and microstructure (Dinovitzer et al., 2019), tensile strength (Ning et al., 2017), and, width and penetration depth of single scan track (Makoana et al., 2018), etc. In addition to experimental

studies, various LPBF processes, especially meltpool behavior (Letenneur et al., 2019), build layers (Mirkoohi et al., 2018), laser heat source (Mirkoohi et al., 2019) effects have been analytically studied. Hybrid modeling that combines analytical models and machine learning-based models is useful in estimating desirable meltpool dimensions and optimized process variables (Mondal et al., 2020).

On the modeling front for LPBF, literature focused on the modeling of the rich multiphysics aspects of the process has been extensively published. Abolhasani et al. (2019) studied the effect of reinforced materials on the cooling rates and meltpool behavior of AlSI 304 stainless steel using finite element method simulations. Ansari et al. (2019) developed a 3D finite element method based thermal model using a volumetric Gaussian laser heat source to model the thermal profile and meltpool size in selective laser melting process. The heat diffusion models were reinforced by considering localized dynamic and unsteady fluid flow inside the meltpool. Dong et al. (2018) considered phase transformation, thermo-physical properties, heat transfer, and meltpool dynamics in their finite element model to investigate the effect of laser power and hatch spacing on the meltpool. Similar multiphysics model accounting for heat diffusion and fluid flow was presented by Ansari et al. (2021) to study the effect of laser power and spot diameter on meltpool temperature in the LPBF process. Gusarov et al. (2007) focused on heat transfer and radiation physics in their numerical model. More comprehensive numerical models of the LPBF considers temperature-dependent properties, powdered layer, fluid flow, laser scanning, etc. Mukherjee et al. (2018) used comprehensive LPBF numerical models to simulate fluid flow and heat diffusion dynamics for most commonly used alloys. Khairallah and Anderson (2014) provided richer insights into LPBF printing of stainless steel using various continuum numerical models. (Wang et al., 2019b) coupled finite volume, discrete element, and volume of fluid methods to rigorously model power

spreading, powder melting, and multi-layer effects during LPBF AM of Ti-6Al-4V alloy. In trying to capture all the important aspects of the LPBF process in a numerical model, challenges exist in terms of numerous variables, process parameters, and their complex interactions, and these are outlined in the work of Keshavarzkermani et al. (2019) and Fayazfar et al. (2018).

Physical processes with many independent parameters can be analyzed and investigated using dimensional analysis. Traditional areas of physics and engineering, especially fluid mechanics and heat transfer have used dimensional and scaling analysis extensively Ruzicka (2008). Researchers in AM-related problems have recently started incorporating dimensional analysis in their work. Van Elsen et al. (2008) provided a comprehensive list of dimensionless quantities that are relevant for the additive and rapid manufacturing process. They justified the usability of the dimensional analysis to investigate complex additive processes like LPBF. Dimensionless numbers were shown to assist in choosing previously unknown process parameters for the LPBF process to print Haynes 282, a nickel-based superalloy (Islam et al., 2022). Weaver et al. (2022) demonstrated the application of universal scaling laws to study the effect of process variables such as laser spot radius on the meltpool depth. Rankouhi et al. (2021) in their experimental work applied the Buckingham-π theorem in conjunction with Pawlowski matrix transformation to present dimensionless quantities that correlate well with the density or porosity of the built component. Their proposed non-dimensional quantity is shown to be applicable across different material properties and machine variables, thereby achieving desirable scaling. Another widely applicable dimensionless quantity called Keyhole number was proposed by Gan et al. (2021). They made use of dimensionless analysis in conjunction with multiphysics numerical models and high-tech X-ray imagining in their discovery. Keyhole number provides useful insights into the aspect ratio of the meltpool

and the transformation of the meltpool from a stable to a chaotic regime. Wang and Liu (2019) proposed four sets of dimensionless quantities combining process parameters and material properties. Their experimental analysis shows these numbers can effectively characterize phenomena like the continuity of the track and its size and the part porosity. Noh et al. (2022) showed that normalized enthalpy and relative penetration depth in the vertical direction can provide reliable process map for printing single track 3D geometries using selective laser melting process.

The published literature surveyed for this work either uses experimental or numerical methods to propose new dimensionless quantities which are specific to the AM process and are not always related to classical dimensionless numbers used in the fields of fluid mechanics and heat transfer. Classical dimensionless numbers like the Péclet number can provide a good understanding of the impact of process variables on the printed components. Nusselt, Fourier, and Marangoni number provide a good understanding of the mode of heat transport inside the meltpool for varying laser power and scan speed Ahsan et al. (2022)-Wu et al. (2022) .Cardaropoli et al. (2012) provided a map for Ti-6Al-4V alloy linking dimensionless quantities with the porosity of built parts. Mukherjee et al. (2017) used their established numerical models of the LPBF process to simulate the building of the different materials with varied process variables. Using a known set of dimensionless numbers representing heat input, Péclet, Marangoni, and Fourier numbers, they made sense of the impact of process parameters on important output variables like temperature field, cooling rates, fusion defects, etc.

Similar to the meltpool in the LPBF process, the traditional welding process also involves the formation of a weldpool which is the site of various multiphysics interactions and processes. Literature on the use of dimensional analysis to understand the flow patterns in the weldpool offers insights that are relevant to AM. This includes the work by Robert and

Debroy (2001) where they highlighted the importance of dimensionless numbers like Prandtl, Péclet, and Marangoni in understanding the aspect ratio of the weldpool. Using the numerical models to predict the weldpool shape for a range of materials, they presented the insightful role of these numbers in shaping the weldpool morphology. Similarly, Lu et al. (2004) also discusses the role of Marangoni convection in affecting the aspect ratio and shape of the weldpool. Their analysis shows that the effect of welding process conditions on the weld part can be understood by looking at the non-dimensional numbers like Péclet and Marangoni. Wei et al. (2009) showed that the formation of a wavy fusion boundary is linked with the critical values of the Marangoni and Prandtl numbers. Fusion boundaries and shapes have a significant impact on the microstructure of the material. Asztalos et al. (2022) applied dimensional analysis to study the polymer additive manufacturing processes.

As can be seen from the literature review presented, the use of dimensionless numbers to understand the complex interaction of physical processes is gaining attention. However, among the proposed dimensionless quantities, few are universally applicable. Some of them remain applicable only in the context of a specific study or alloy. A universal dimensionless variable or normalized graph can facilitate the comparison of results between different studies using different materials Chia et al. (2022). This leaves room for the development of novel approaches to characterize the LPBF process using dimensional analysis. The goal is to perform such a dimensional analysis and investigate the relation between meltpool morphology and to a lesser degree, microstructure evolution, and the underlying dimensionless quantities naturally manifested by the thermo-fluidic governing equations of the LPBF process. In this context, a novel numerical strategy is presented in Chapter 3, where the data generated using numerical simulations of the thermo-fluidic model for different alloys and different process parameters was used, along with

linear regression analysis, to characterize meltpool morphology in terms of the dimensionless numbers relevant to the meltpool heat and mass transport.

Effect of meltpool fluid convection and remelting on microstructure evolution

Material properties of metallic alloys are significantly dependent on the underlying grain structures at the microstructure scale. For example, in many applications, it is desirable to have an equiaxed solidification morphology that can result in a small grain structure. The equiaxed dendrite grows from nucleation created through liquid stirring or grain refinement additions. In the absence of such external measures, the growth of equiaxed dendrites could stem from dendrite fragments acting as nuclei. Hellawell et al. (1997) outlined the physics associated with the dendrite fragments process. This includes temperature and time-dependent steps such as a) formation of dendrite fragments from primary arms due to local remelting, b) fragment transport, c) melting or growth of dendrite fragments, d) sedimentation under the influence of gravity, and e) columnar to equiaxed transition. Local remelting of dendrite arms leading to grain refinement in the manufacturing of Magnesium alloy using welding arc oscillation is demonstrated in the work of Yuan et al. (2016). Dendrite fragmentation caused by local reheating was the leading cause of refined grain was the outcome of their work. This refined grain led to improved solidification-cracking resistance and mechanical properties. Yang et al. (2019) showed dense and homogeneous dendritic features in microstructure morphology resulting from remelting of layers, which has a favorable effect on the magnetization and mechanical properties of Fe-Co based alloy. Yasuda et al. (2019) experimentally studied dendrite fragmentation in Fe-C alloys and provided a detailed fragmentation mechanism where the role of heating and cooling per phase-equilibrium was pertinent.

The experimental studies demonstrating dendrite remelting and fragmentation led to a detailed investigation into the modeling of the dendrite remelting phenomenon. Burbelko et al. (2010) used the Cellular Automata Finite Difference method to model heat diffusion, mass diffusion, and anisotropic dendritic growth during the solidification process. A local remelting due to interaction between secondary arms and neighboring grains was demonstrated in their work. Zhang et al. (2017) developed a quantitative cellular automaton model to study the complex interaction between coarsening of dendrite along with local remelting. Their developed model incorporated temperature and concentration evolution with the role of curvature by rightly accounting for associated thermodynamics and kinetics process. Remelting processes such as dissolution of side arms, dendrite arm fragmentation, and solute enrichment leading to necking are correctly predicted using this model. Dendrite fragmentation in Al-Cu alloy was extensively studied using a phase-field model by Wesner et al. (2012). Fragmentation was modeled by the rise in the temperature above the melting point so temperature and temperature gradient history was critical in their modeling process. Two and three-dimensional dendrite fragmentation studies were carried out and interaction between melting and coarsening in the formation of fragments of secondary dendrite arm were discovered using the model developed. Pinching off and remelting of side branches of Magnesium alloy dendrite was studied in the work of Yue et al. (2022). They used a phase-field model and incorporated a reversal of the direction of the solid-liquid interface governed by the reheating and cooling caused by arc oscillation in the gas-tungsten arc welding process. The dendrite morphology generated using their model was consistent with experimental findings.

It is evident from the literature that dendrite remelting is an important phenomenon in the evolution of the final microstructure and resulting material properties. While the mechanism of remelting and its effects are

studied in the context of traditional manufacturing process such as arc welding, the effect of remelting of dendrite in metal additive manufactruing process is not critically focused upon. Metal additive manufacturing using a laser powder bed fusion process produces rapid heating and cooling temperature cycles. The solidifying region around the meltpool or solidified region in layers beneath the meltpool, when subjected to such cycles, will undergo reheating and solidification. The temperature cycle can have a profound impact on the microstructure evolution. Studying this impact of temperature remelting is one of the leading lines of inquiry in this work. In this regard, models such as phase-field method can be applied with appropriate modifications to temperature and concentration undercooling. Such modifications to the phase-field method and its applications to critical solidification conditions prevalent in the additive process to predict remelting of evolving of dendrite morphology is an important aspect of this work.

While the remelting results in the changes to the dendrite morphology, the changes to morphology due to convection in the liquid melt during solidification is another line of inquiry in studying microstructure evolution process. The combined convection and diffusion is a complex process that has not been studied adequately. In additive manufacturing processes such as laser powder bed fusion, the shape of the meltpool is influenced by the degree of Marangoni convection. The meltpool shapes in turn affect the grain growth process and ultimately influences the material properties of additively manufactured alloy. The impact on material properties can be closely studied by understanding microstructure morphology evolved during the solidification process. The following text explores the critical survey of literature that studied dendrite solidification and liquid melt convection during traditional process through theoretical, numerical, and experimental tools and motivate the need for focusing on the convection effects of solidification in the additive manufacturing process.

The microstructure evolution previously surveyed is the result of the heat and solute diffusion process accompanied by curvature effects and temperature-phase equilibrium conditions. Microstructure evolution and more specifically dendritic solidification under the influence of convection in the liquid is different from pure heat and mass-diffusion-based processes. An experimental work investigating the effect of natural and forced convection on solidification of Ga-In alloys using X-ray radiography techniques carried out by Shevchenko et al. (2015). Their study reveals complex interaction between dendritic growth and melt convection. In particular, local flow conditions such as arm spacing, orientation, local flow conditions and intensity are very critical for convection driven dendrite growth. One of the earlier theoretical works exploring the effect of fluid flow consist of studying the effects of buoyancy, forced flow, and volume-change convection on morphological changes during the directional solidification process is done by Davis (1990). The effect of macroscopic factors such as velocity on deviations to the anisotropic growth of dendrtic was analyzed in the theoretical work of Ben-Jacob and Garik (1990). The experimental observation by Mirihanage et al. (2012) done using synchrotron X-ray in the solidification of Al-Cu-Si alloy shows considerable convection effects on solute distribution and growth rate of dendrites. Murakami et al. (1983) carried out solidification of Al-Cu alloys in the presence of flowing melt and established the dependence of deflection angle of columnar dendrite and columnar grains on Cu content and fluid flow velocities. Similarly, experimental work of Min et al. (2011) explores the effect on primary dendrite arm spacing of dendrite grown in directional solidification with induced fluid flow through traveling magnetic fields. Dendite morphology evolved in different gravity environment is similar to changes brought out by convection in liquid flow. Motivated with the experimental findings on the impact of microgravity and effect of Marangoni convection on the dendrite solidification and microstructure, Nabavizadeh et al. (2020)

numerically explores the growth of dendrite features that shows bending and higher growth rate due to convection. Thus the evidence on the substantial impact of fluid convection on microstructure is apparent as suggested by several experimental studies.

The convection in the liquid melt along with dendrite growth in the solid phase is a challenging problem and need advanced numerical modeling approach. A combination of Navier-Stokes and phase-field, Lattice Boltzmann and phase-field, Navier-Stokes and interface tracking method have been applied in the literature. Some of these literature include a phase-field model for the solidification of pure metals with convection in the liquid phase was presented by Anderson et al. (2000). With the assumption of large viscosity in the solid phase, two critical cases mainly density change flow, and shear flow, and their impact on the solidification of the planar front was studied in their work. A three-part work on equiaxed dendrite morphology and convection effect exploring the development of volume average multi-phase model of solidification and fluid flow, its numerical implementation and validation with experiments are carried out in Wang and Beckermann (1996)-Beckermann and Wang (1996). A diffuse interface phase-field model coupled with convection in the liquid phase was introduced in the work of Beckermann et al. (1999). The no-slip boundary condition between the liquid and solid region interface was enforced using higher drag force in the diffuse interface region. Chen and Yang (2019) in their work developed a more numerically suitable form of modeling melt convection and pure melt solidification. Their form is modified from what is presented in the work of Beckermann et al. (1999). The presented numerical scheme by Chen and Yang (2019) is unconditionally stable that solves coupled fluid flow, and anisotropic phase field equations. Ren et al. (2020) modeled melt convection and dendritic growth of binary alloy as a Fluid-Structure interaction problem. They treated liquid and solid as an incompressible Newtonian fluid with a solid viscosity of

order as large as 10^{10}. This was possible with an efficient preconditioner developed to solve Navier-stokes and multi-phase field equations with large variations of viscosity in the liquid and solid phases. Advection of solid dendrites i.e. rotation, settlement, growth of multiple dendrites, and impingement of dendrites were modeled in their work. Navier-Stokes and phase-field methods although very challenging to implement but are effective in modeling the complex fluid flow process and coupled dendrite growth.

Another class of numerical methods widely used in modeling convection in the liquid melt with dendritic growth is coupled Lattice Boltzmann Method and Phase-field model. Implementation of Lattice Boltzmann Method to model fluid flow and rigid body motion in the solid phase is computationally less expensive than Navier-Stokes. Rojas et al. (2015) demonstrated the combined use phase-field method of solidification and the Lattice Boltzmann Method to model the fluid flow of the liquid melt, rigid body motion of solid dendrite, and diffusive growth of dendrite. The no-slip conditions at the solid interface were implemented using a diffusive forcing term in the LBM method. Fluid flow cases presented in their work show convection-driven dendritic growth and rigid body motion of solid dendrites. Complex dendrite interaction such as multiple equiaxed dendrite growth, collision, coalescence, and grain growth was modeled using a combination of a multi-phasic phase-field model of solidification accounting for the interaction between columnar and equiaxed grains, Lattice Boltzmann Method for fluid flow and equations of motion for solid phases in the work of Takaki et al. (2018). The model is an extension to the previous work of Rojas et al. (2015) which demonstrated the ability to model complex microstructure evolution conditions. Rátkai et al. (2019) studied a columnar to equiaxed transition for the Al-Ti system using a phase-field method of solidification and the Lattice Boltzmann Method. The implemented numerical model uses a global and local mesh to capture

the effect of gravity on moving particles, collisions among particles, solute and heat diffusion, and fluid flow. Similarly, the process of settlement, the collision of dendrites, and the coalescence of equiaxed dendrites were modeled using a multi-phasic phase-field model and Lattice Boltzmann method in the work of Liu et al. (2022). The implemented model clearly showed stark differences in the microstructure features such as dendrite size, spacing, morphology, and solute distribution in the presence and absence of melt flow during solidification growth. While phase-field methods are popular to study solidification, different solidification methods were also applied to study fluid flow and convection processes. A two and three-dimensional explicit front interface tracking method of dendrite solidification and Navier-stokes to model convection was presented in the work of Al-Rawahi and Tryggvason (2002)-Al-Rawahi and Tryggvason (2004). The velocities in the solid phase were specified as zero. Good comparison with other numerical models and realistic effect of fluid flow on the growth of dendrite and side branching was captured using their numerical model. Yuan and Lee (2010) also demonstrated the use interface-tracking method coupled with Navier-Stokes equations to model 2D and 3D equiaxed dendrite growth under the influence of forced flow and columnar dendrite growth under the influence of natural convection.

The extensive literature showcases the variety of experimental and numerical studies done to understand morphological changes to dendrites in traditional directional solidification process or manufacturing process such as welding. These studies are valuable to initiate similar inquiry into morphological changes to dendrites especially during additive manufacturing. While number of literature is growing in additive field, there is room for more focused attention to study dendritic solidification with convective effects magnified during additive manufacturing. The source of this magnification is favorable laser power characteristics that generate rapid heating and cooling cycles and meltpool with significant convection.

A study focusing on both the temperature remelting and convection effects on various dendritic morphologies such as equiaxed and columnar observed during pure metal and binary alloy solidification is attempted in the work described in Chapter 4.

2 HIGH FIDELITY NUMERICAL MODELING OF DENDRITIC SOLIDIFICATION

In Section 2.1 a detailed discussion of the numerical models used in this work to model dendritic growth is presented. Essentially, the appropriate Stefan problem formulations and their phase-field representations for modeling the solidification problem of pure melts and binary alloys. Then, in Section 2.2, the numerical framework and its computational implementation is discussed. Further, a numerical error analysis and the simulation results of various 2D and 3D dendritic solidification problems are presented.

2.1 Numerical models of dendritic growth

[1] In this section, the Stefan problem for modeling solidification of a pure metal and a binary alloy is discussed. The complexities of the Stefan problem and the physics associated with solidification are also elaborated. The Stefan problem is then re-written as a phase-field formulation. The primary goal of using a phase-field approach is to model the interface growth kinetics, particularly the velocity of interface motion and the complex morphologies of dendrites that occur during solidification, without the need to explicitly track the dendritic interfaces. The interface growth can be influenced by the surface anisotropy, heat diffusion, mass diffusion, interface curvature, and the interface attachment kinetics. In Sections 2.1.1-2.1.2, the classical Stefan problem and its phase-field representation relevant to solidification of pure melts is presented. Then, in Sections 2.1.3-2.1.4, the

[1] The work presented in Chapter 2 has been published as : Kunal Bhagat and Shiva Rudraraju,"Modeling of dendritic solidification and numerical analysis of the phase-field approach to model complex morphologies in alloys.", Engineering with Computers (2022): 1-19.

extensions needed in the Stefan problem and its phase-field representation for modeling solidification of binary alloys are discussed.

In general, a pure melt is a single-component material (pure solvent) without any solutes. Addition of one or more solute components results in an alloy. In this work, a binary alloy (two-component alloy with a solvent and one solute), is specifically considered as a representative of multi-component alloys. And as will be shown, during the solidification of a binary alloy, diffusion of this solute concentration in the solid and liquid phases is modeled.

2.1.1 Stefan problem for modeling solidification of a pure melt

The Stefan problem describing the solidification of an undercooled pure metal is presented. The set of Equations 2.1a-2.1c mathematically model the solidification of an undercooled pure melt. Equations 2.2a-2.2c represent the same governing equations in a non-dimensional form. Equation 2.1a models heat conduction in the bulk liquid and the bulk solid regions of the pure metal. At the solid-liquid interface, the balance of the heat flux from either of the bulk regions is balanced by the freezing of the melt, and thus additional solid bulk phase is formed. In other words, the solid-liquid interface moves. The energy balance at the interface is given by the Equation 2.1b. The temperature of the interface is not fixed and can be affected by multiple factors such as the undercooling effect on the interface due to its curvature (Gibbs-Thomson effect) and the interface attachment kinetics. These are captured in the equation 2.1c.

$$\frac{\partial T(\mathbf{x},t)}{\partial t} = \frac{k}{c_p}\nabla^2 T, \quad \mathbf{x} \in \Omega^s, \Omega^l \tag{2.1a}$$

$$\boldsymbol{\nu}_n L = k\big(\partial_n T(\mathbf{x})|^+ - \partial_n T(\mathbf{x})|^-\big), \quad \mathbf{x} \in \Gamma \tag{2.1b}$$

$$T_m - T_i = \Delta T_{\Gamma_g} + \Delta T_{\mu_k} = \Gamma_g \kappa + \frac{\nu_n}{\mu_k}, \quad x \in \Gamma \tag{2.1c}$$

Here, k and c_p are thermal conductivity and specific heat capacity for a pure solid or liquid metal. T_m ν_n, L is the melting temperature, interface velocity, and latent heat of the metal. $\partial_n T|^+$ and $\partial_n T|^-$ is the temperature gradient normal to the interface in the liquid and the solid phase respectively. Γ_g, κ, and μ_k are the Gibbs-Thomson coefficient, the curvature of the interface, and interface-attachment coefficient, respectively. These equations are re-written in their non-dimensional form, using the scaled temperature $u = \frac{c_p(T-T_m)}{L}$ (Dantzig and Rappaz, 2016).

$$\frac{\partial u(x,t)}{\partial t} = D\nabla^2 u, \quad x \in \Omega^s, \Omega^l \tag{2.2a}$$

$$\nu_n = D\left(\partial_n u(x)|^+ - \partial_n u(x)|^-\right), \quad x \in \Gamma \tag{2.2b}$$

$$u^* = -d(n)\kappa - \beta(n)\nu_n, \quad x \in \Gamma \tag{2.2c}$$

$D = \frac{k}{c_p}$ is the non-dimensional thermal diffusivity in the solid and liquid phases. $d(n) = \gamma(n)T_m c_p/L^2$ is the capillary length, $\gamma(n)$ is the surface tension, n is the unit vector denoting normal to the interface, $\beta(n)$ is the kinetic coefficient, and $\partial_n u|^+$ and $\partial_n u|^-$ are the non-dimensional derivatives normal to the interface in the solid and liquid region, respectively (Slavov et al., 2003). The driving force for this solidification is the initial undercooling, i.e., the initial temperature of the liquid melt below its melting temperature. The non-dimensional undercooling is given by $\Delta = -c_p(\frac{Tm-T_\infty}{L})$.

The Stefan problem described using Equation 2.1 does not have a known analytical solution, and its numerical implementation, as is the case with free boundary problems, is challenging. Numerical methods like time-dependent boundary integral formulations (Karma and Rappel, 1996), a variational algorithm with zero or non-zero interface kinetics, and methods that require the book-keeping of the solidifying front and

low grid anisotropy conditions have been used in the past. Modeling correct dendritic growth involves getting the correct operating dendritic tip conditions, mainly the tip radius and the tip velocity. Variationally derived phase-field models, like the one described in Section 2.1.2, are now the method of choice to model complex dendritic solidification problems.

2.1.2 Phase-field model describing the solidification of a pure melt

In this section, the phase-field method developed by Plapp and Karma (2000) to model solidification in a pure metal is described. The governing equations for the model are derived using variational principles. A phenomenological, isothermal free energy expression, $\Pi[\phi, u]$, in terms of a phase-field order parameter (ϕ) and temperature (u), is given by Equation 2.3.This functional form defines the thermodynamic state of a system, and has two terms - first is $f(\phi, u)$, the bulk energy term, and second is an interface term given by $\frac{1}{2}\lambda^2(\mathbf{n})|\boldsymbol{\nabla}\phi|^2$. The magnitude of the interface term is controlled by the interface parameter, λ, and the interface term is positive in the diffuse solid-liquid interface due to a non-zero gradient of the order parameter elsewhere, the interface term is zero.

$$\Pi[\phi, u] = \int_{\Omega} \left[f(\phi, u) + \frac{1}{2}\lambda^2(\mathbf{n})|\boldsymbol{\nabla}\phi|^2 \right] \, dV \tag{2.3a}$$

$$f(\phi, u) = -\frac{1}{2}\phi^2 + \frac{1}{4}\phi^4 + \xi u\phi \left(1 - \frac{2}{3}\phi^2 + \frac{1}{5}\phi^4\right) \tag{2.3b}$$

The bulk energy term $f(\phi, u)$ in Equation 2.3b is given by the double well potential that has a local minima at $\phi = 1$ and $\phi = -1$. $\Omega = \Omega_s \cup \Omega_l$ represents total volume encompassing the bulk solid, the bulk liquid and the interface region. The value of u then tilts the equilibrium value of $f(\phi, u)$. The form of $f(\phi, u) = g(\phi) + \xi u h(\phi)$ is given below. ξ is the coupling

parameter in the double well function. The governing equations for the phase-field model of solidification are obtained by minimizing the above functional with respect to the primal fields, ϕ. The governing equations for the temperature field, u, are obtained by taking the variational derivative of the Lyapunov functional: $\Pi_L[\phi, u] = \int_\Omega \left[g(\phi) + \xi u^2 + \frac{1}{2}\lambda^2(\mathbf{n})|\boldsymbol{\nabla}\phi|^2\right] dV$, whose isothermal form is given by Equation 2.3a. A detailed discussion on this functional and its isothermal form are beyond the scope of this manuscript, and interested readers are referred to the relevant literature Plapp and Karma (2000); Boettinger et al. (2002); Karma and Rappel (1998). The non-dimensional enthalpy, U, accounts for the change in temperature and the latent heat, $U = u - \frac{1}{2}\phi$. In terms of the enthalpy, the governing equations for the first-order kinetics are given by:

$$\frac{\partial U(\boldsymbol{x}, t)}{\partial t} = \boldsymbol{\nabla}.\left(D\boldsymbol{\nabla}\frac{\delta\Pi_L}{\delta u}\right), \quad \boldsymbol{x} \in \Omega \tag{2.4a}$$

$$\tau(\mathbf{n})\frac{\partial\phi(\boldsymbol{x}, t)}{\partial t} = -\frac{\delta\Pi}{\delta\phi}, \quad \boldsymbol{x} \in \Omega \tag{2.4b}$$

Rewriting these equations in terms of the primal fields, u and ϕ, yields Plapp and Karma (2000),

$$\frac{\partial u}{\partial t} = D\nabla^2 u + \frac{1}{2}\frac{\partial\phi}{\partial t}, \quad \boldsymbol{x} \in \Omega \tag{2.5a}$$

$$\begin{aligned}\tau(\mathbf{n})\frac{\partial\phi}{\partial t} = -\frac{\partial f}{\partial\phi} + \boldsymbol{\nabla}\cdot\left(\lambda^2(\mathbf{n})\boldsymbol{\nabla}\phi\right) + \frac{\partial}{\partial\boldsymbol{x}}\left[|\boldsymbol{\nabla}\phi|^2\lambda(\mathbf{n})\frac{\partial\lambda(\mathbf{n})}{\partial\left(\frac{\partial\phi}{\partial\boldsymbol{x}}\right)}\right] \\ + \frac{\partial}{\partial y}\left[|\boldsymbol{\nabla}\phi|^2\lambda(\mathbf{n})\frac{\partial\lambda(\mathbf{n})}{\partial\left(\frac{\partial\phi}{\partial y}\right)}\right], \boldsymbol{x} \in \Omega\end{aligned} \tag{2.5b}$$

where Ω denotes the problem domain. Anisotropy in the interface energy representation is considered. Thus, $\lambda(\mathbf{n}) = \lambda_0 a_s(\mathbf{n})$ and $\tau(\mathbf{n}) = \tau_0 a_s^2(\mathbf{n})$,

where τ_0 is the characteristic time scale of evolution of the order parameter. The anisotropy parameter is defined as $a_s = (1-3\epsilon_4)\Big[1 + \frac{4\epsilon_4}{(1-3\epsilon_4)}\frac{(\partial_x\phi)^4+(\partial_y\phi)^4}{|\phi|^4}\Big] = 1 + \epsilon_4 cos(m\theta)$. The equivalence is easily established by taking $\tan(\theta) = \frac{\partial\phi}{\partial y}/\frac{\partial\phi}{\partial x}$. ϵ_4 is the strength of anisotropy and m=4 corresponds to an anisotropy with four-fold symmetry. The interface between the solid and liquid phases is diffuse in the phase-field representation of a Stefan problem of solidification, but in the asymptotic limit of $\lambda(\mathbf{n}) \to 0$, the Stefan problem is recovered (Caginalp, 1986, 1989).

Weak formulation

The above governing equations in their weak (integral) form are posed here. This formulation is used to solve these equations within a standard finite element method framework.

Find the primal fields $\{u, \phi\}$, where,

$$u \in \mathscr{S}_u, \quad \mathscr{S}_u = \{u \in H^1(\Omega) \mid u = u' \; \forall \, \mathbf{X} \in \Gamma^u\},$$
$$\phi \in \mathscr{S}_\phi, \quad \mathscr{S}_\phi = \{\phi \in H^1(\Omega) \mid \phi = \phi' \; \forall \, \mathbf{X} \in \Gamma^\phi\}$$

such that,

$$\forall \, w_u \in \mathscr{V}_u, \quad \mathscr{V}_u = \{w_u \in H^1(\Omega) \mid w_u = 0 \; \forall \, \mathbf{X} \in \Gamma^u\},$$
$$\forall \, w_\phi \in \mathscr{V}_\phi, \quad \mathscr{V}_\phi = \{w_\phi \in H^1(\Omega) \mid w_\phi = 0 \; \forall \, \mathbf{X} \in \Gamma^\phi\}$$

we have,

$$\int_\Omega w_u \Big(\frac{\partial u}{\partial t} - \frac{1}{2}\frac{\partial \phi}{\partial t}\Big)\, dV + \int_\Omega D\big(\boldsymbol{\nabla} w_u . \boldsymbol{\nabla} u\big)\, dV = 0 \qquad (2.6a)$$

$$\int_{\Omega} w_{\phi}\left(\tau\frac{\partial\phi}{\partial t}+\frac{\partial f}{\partial\phi}\right)\,dV+\int_{\Omega}\lambda^{2}\boldsymbol{\nabla}w_{\phi}.\boldsymbol{\nabla}\phi\,dV+\int_{\Omega}|\boldsymbol{\nabla}\phi|^{2}\lambda\frac{\partial w_{\phi}}{\partial x}\frac{\partial\lambda}{\partial\left(\frac{\partial\phi}{\partial x}\right)}\,dV \tag{2.6b}$$
$$+\int_{\Omega}|\boldsymbol{\nabla}\phi|^{2}\lambda\frac{\partial w_{\phi}}{\partial y}\frac{\partial\lambda}{\partial\left(\frac{\partial\phi}{\partial y}\right)}\,dV=0$$

here, $\Omega=\Omega_{s}\cup\Omega_{l}$, where Ω_{s} is the solid phase and Ω_{l} is the liquid phase, respectively. The variations, ω_{u} and ω_{ϕ}, belong to $H^{1}(\Omega)$ - the Sobolev space of functions that are square-integrable and have a square-integrable derivatives.

2.1.3 Stefan problem for modeling solidification of a binary alloy

The Stefan problem describing the solidification of a binary alloy is described in this section. As mentioned earlier, an alloy is a multi-component system. A binary alloy is a specific case of a multi-component alloy with only one solute component. A binary alloy consists of a solute that has a composition of c, and a solvent that has a composition of $(1-c)$. During the solidification of a binary alloy, we model the diffusion of the solute concentration across the solid and the liquid phase. Mass diffusion is governed by Equation 2.7a. Near the vicinity of the solid-liquid interface, the composition of the solute in the solid and the liquid phase is dictated by the binary alloy phase diagram given in the Figure 2.1a. The difference in the concentration of the solute across the solid and liquid phase is balanced by the mass diffusion flux. This is captured in Equation 2.7b. The temperature of the interface is not fixed and can be affected by multiple factors. The undercooling on the interface can be due to its curvature (Gibbs-Thomson effect), the interface attachment kinetics, cooling rate ($\dot{T}$), and the applied temperature gradient. This is mathematically represented

in Equation 2.7c. Using the phase-diagram, this condition can be written in-terms of composition, c_l at the interface. The contribution from the attachment kinetics is neglected. $c_l = c_l^0 - \frac{\Gamma_g \kappa + G y + \dot{T} t}{|m|}$ where c is the solute composition in either the solid or the liquid phase. D is the mass diffusivity of alloy in the liquid phase, c_l and c_l^0 are the solute concentration at the interface for the temperature T_i and T_0 respectively. $\dot{T} = G\boldsymbol{\nu}_p$ is the cooling rate. The solute concentration is scaled into a variable $u_c = \frac{c - c_l^0}{c_l^0(1-k)}$ which represents supersaturation. k is the partition coefficient which represents the ratio of solid composition to the liquid composition.

$$\frac{\partial c(\boldsymbol{x}, t)}{\partial t} = D\nabla^2 c(\boldsymbol{x}, t), \quad \boldsymbol{x} \in \Omega^s, \Omega^l \tag{2.7a}$$

$$c_l(1-k)\boldsymbol{\nu}_n = -D\partial_n c(\boldsymbol{x}, t)|^+, \quad \boldsymbol{x} \in \Gamma \tag{2.7b}$$

$$T_m - T_i = \Gamma\kappa + \frac{\boldsymbol{\nu}_n}{\mu_k} + Gy + \dot{T}t, \quad \boldsymbol{x} \in \Gamma \tag{2.7c}$$

here, Γ is the solid-liquid interface that separates the solid phase, Ω^s, and the liquid phase, Ω^l.

Rewriting the Equations 2.7a, 2.7b and 2.7c in-terms of the supersaturation, u_c, we get,

$$\frac{\partial u_c(\boldsymbol{x}, t)}{\partial t} = D\nabla^2 u_c(\boldsymbol{x}, t), \quad \boldsymbol{x} \in \Omega^s, \Omega^l \tag{2.8a}$$

$$(1 + (1-k)u_c^*)\boldsymbol{\nu}_n = -D\partial_n u_c(\boldsymbol{x}, t)|^+, \quad \boldsymbol{x} \in \Gamma \tag{2.8b}$$

$$u_c^* = -d_0\kappa + \dot{\theta}t - \gamma z, \quad \boldsymbol{x} \in \Gamma \tag{2.8c}$$

Here $d_0 = \frac{\Gamma_g}{\Delta T_0}$ is the chemical capillary length , $\dot{\theta} = \frac{-\dot{T}}{\Delta T_0}$ is the non-dimensional cooling rate and $\gamma = \frac{G}{\Delta T_0}$ is non-dimensional thermal gradient and $\Delta T_0 = |m|(1-k)c_l^0$ (Neumann-Heyme, 2017).
As can be expected, an analytical solution for the moving boundary problem in Equations 2.8 is not known. In the next subsection, a phase-field representation of this problem that is extensively used to model dendritic

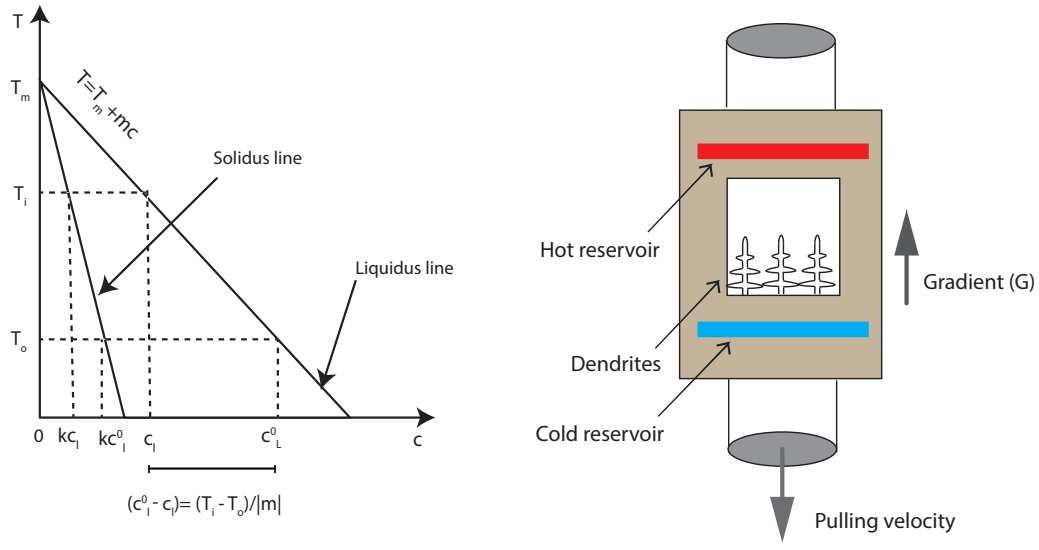

Figure 2.1: Directional solidification in a binary alloy. Shown are (2.1a) a simplified phase diagram of a binary alloy, and (2.1b) a schematic of a directional solidification process. In the case of directional solidification, typically, the melt is forced to solidify at a constant pulling velocity under a fixed temperature gradient. The dendritic structures in this case evolve at the solid-liquid interface, via a Mullins-Sekerka instability, when the pulling velocity is above a critical value.

solidification of binary alloys is discussed.

2.1.4 Phase-field model describing the solidification of a binary alloy

In this section, the phase-field model for the solidification of a binary alloy is described. Following the variational procedure adopted in the case of a pure melt, we write the free energy functional form, $\Pi[\phi, c, T]$, for a binary alloy. The free energy in this case has the additional dependence on the solute composition, c, along with the order paramter, ϕ, and the temperature, T. This functional form, given by Equation 2.9, takes into ac-

count bulk free energy of the system $f(\phi, T_m)$, internal energy and entropy $f_{AB}(\phi, c, T)$, and the interface term $\frac{1}{2}\sigma|\boldsymbol{\nabla}\phi|^2$, where $\sigma \propto \lambda^2$.

$$\Pi[\phi, c, T] = \int_\Omega \left[f(\phi, T_m) + f_{AB}(\phi, c, T) + \frac{1}{2}\sigma|\boldsymbol{\nabla}\phi|^2 \right] \, dV \tag{2.9}$$

here $\Omega = \Omega_s \cup \Gamma \cup \Omega_l$ represents the total volume encompassing the bulk solid, the bulk liquid and the interface region. The governing equations for the model are obtained by writing the diffusion equations relevant to a conserved quantity - the solute composition, and a non-conserved quantity - the order-parameter.

$$\frac{\partial c(\boldsymbol{x}, t)}{\partial t} = \boldsymbol{\nabla}.\Big(M(\phi, c)\boldsymbol{\nabla}\frac{\delta\Pi}{\delta c}\Big), \quad \boldsymbol{x} \in \Omega \tag{2.10a}$$

$$\frac{\partial \phi(\boldsymbol{x}, t)}{\partial t} = -K_\phi \frac{\delta\Pi}{\delta\phi}, \quad \boldsymbol{x} \in \Omega \tag{2.10b}$$

where $M(\phi, c)$ is the solute mobility, and K_ϕ is the order parameter mobility. It is convenient to scale the composition, c and write it as $u_c = \frac{1}{1-k}\big(\frac{2c}{c_l^0(1-\phi+k(1+\phi))} - 1\big)$. The parameter u_c can be understood as a concentration undercooling parameter analogous to u in Section 2.1.2. This change of variable enables us to draw similarities with the earlier form of the phase-field model described in Equations 2.5. At the onset of solidification, the initial solute concentration in the liquid region is $c = c_l^0$ and the solute concentration in the solid region is $c = kc_l^0$, as per the phase-diagram. However, when expressed in term of u_c, it is instructional to note that the initial composition undercooling, $u_c = 0$, both in the solid region ($c = kc_l^0, \phi = 1$) and the liquid region ($c = c_l^0, \phi = -1$). Thus, it is preferable to work with u_c as the primal field, as it is a continuous variable across the solid and liquid region unlike the solute composition, c, which is discontinuous, as can be easily seen from the initial conditions. The final form of the phase-field model in Equations 4.1e-4.1f, is presented with-

out the accompanying mathematical derivation. For interested readers, a detailed derivation can be found in Echebarria et al. (2004).

$$\Big(\frac{1+k}{2}-\frac{1-k}{2}\phi\Big)\frac{\partial u_c}{\partial t}=\boldsymbol{\nabla}\cdot\Big(\tilde{D}\big(\frac{1-\phi}{2}\big)\boldsymbol{\nabla}u_c-\mathbf{J}_{at}\Big) \qquad (2.10c)$$
$$+\Big(1+(1-k)u_c\Big)\frac{1}{2}\frac{\partial\phi}{\partial t},\quad \boldsymbol{x}\in\Omega$$

$$\Big(1-(1-k)\frac{y-\tilde{\boldsymbol{v}}t}{\tilde{l}_T}\Big)a_s^2(\mathbf{n})\frac{\partial\phi}{\partial t}=\phi-\phi^3-\xi(1-\phi^2)^2\big(u_c+\frac{y-\tilde{\boldsymbol{v}}t}{\tilde{l}_T}\big)$$
$$+\boldsymbol{\nabla}\cdot\big(a_s^2(\mathbf{n})\boldsymbol{\nabla}\phi\big)+\frac{\partial}{\partial\boldsymbol{x}}\Big(|\boldsymbol{\nabla}\phi|^2a_s(\mathbf{n})\frac{\partial a_s(\mathbf{n})}{\partial\left(\frac{\partial\phi}{\partial\boldsymbol{x}}\right)}\Big),\quad \boldsymbol{x}\in\Omega$$
$$+\frac{\partial}{\partial\boldsymbol{y}}\Big(|\boldsymbol{\nabla}\phi|^2a_s(\mathbf{n})\frac{\partial a_s(\mathbf{n})}{\partial\left(\frac{\partial\phi}{\partial y}\right)}\Big) \qquad (2.10d)$$

The solute diffusivity in the solid region is small as compared to the solute diffusivity in the liquid region. Thus mass diffusion is neglected in the solid region. $\tilde{D}$ is the non-dimensional diffusivity in the liquid phase. In the directional solidification process, dendrite growth is influenced by the presence of a temperature gradient G and pulling velocity $\tilde{\boldsymbol{v}}_p$. This can be realized by the the term $\frac{y-\tilde{\boldsymbol{v}}t}{\tilde{l}_T}$ in the Equation 4.1f, where $\tilde{l}_T=\frac{|m|(1-k)c_l^0}{G}$ is called the thermal length. A modified form of Equation 4.1e was suggested by Ohno and Matsuura (2009) where the mass diffusion in the solid phase is not neglected, and D_s is comparable to D_l. This results in the modification to the diffusivity part and anti-trapping flux current as seen in the Equation 2.10e. If we substitute k=1 and $D_s=D_l$ in this

equation, Equation 4.1e is recovered.

$$\Big(\frac{1+k}{2}-\frac{1-k}{2}\phi\Big)\frac{\partial u_c}{\partial t}=\boldsymbol{\nabla}\cdot\left(\tilde{D}\big(\frac{1-\phi}{2}+k\frac{1+\phi}{2}\frac{D_s}{D_l}\big)\boldsymbol{\nabla}\mathbf{u_c}\right) \\ \boldsymbol{\nabla}\cdot\Big(-(1-k\frac{D_s}{D_l})\mathbf{J}_{at}\Big)+\Big(1+(1-k)u_c\Big)\frac{1}{2}\frac{\partial\phi}{\partial t} \tag{2.10e}$$

Weak formulation

The above governing equations in their weak (integral) form are posed here. This formulation is used to solve these equations within a standard finite element framework.

Find the primal fields $\{u_c, \phi\}$, where,

$$u_c \in \mathscr{S}_{u_c}, \quad \mathscr{S}_{u_c}=\{u_c \in H^1(\Omega) \mid u_c = u_c' \;\forall\, \mathbf{X}\in\Gamma^{u_c}\},$$
$$\phi \in \mathscr{S}_{\phi}, \quad \mathscr{S}_{\phi}=\{\phi \in H^1(\Omega) \mid \phi = \phi' \;\forall\, \mathbf{X}\in\Gamma^{\phi}\}$$

such that,

$$\forall\, w_{u_c} \in \mathscr{V}_{u_c}, \quad \mathscr{V}_{u_c}=\{w_{u_c} \in H^1(\Omega) \mid w_{u_c}=0 \;\forall\, \mathbf{X}\in\Gamma^{u_c}\},$$
$$\forall\, w_{\phi} \in \mathscr{V}_{\phi}, \quad \mathscr{V}_{\phi}=\{w_{\phi} \in H^1(\Omega) \mid w_{\phi}=0 \;\forall\, \mathbf{X}\in\Gamma^{\phi}\}$$

we have,

$$\int_\Omega w_{u_c}\left(\Big(\frac{1+k}{2}-\frac{1-k}{2}\phi\Big)\frac{\partial u_c}{\partial t}-\Big(1+(1-k)u_c\Big)\frac{1}{2}\frac{\partial\phi}{\partial t}\right)dV \\ +\int_\Omega \tilde{D}\big(\frac{1-\phi}{2}\big)\boldsymbol{\nabla}w_{u_c}.\big(\boldsymbol{\nabla}u_c-\mathbf{J}_{at}\big)\,dV=0 \tag{2.11a}$$

$$\int_{\Omega} w_{\phi}\left(\left(1-(1-k)\frac{y-\tilde{\nu}t}{\tilde{l}_T}\right)a_s^2(\mathbf{n})\frac{\partial\phi}{\partial t}-\left(\phi-\phi^3-\xi(1-\phi^2)^2\left(u_c+\frac{y-\tilde{\nu}t}{\tilde{l}_T}\right)\right)\right)dV$$

$$+\int_{\Omega} a_s^2\boldsymbol{\nabla}w_{\phi}.\boldsymbol{\nabla}\phi\,dV+\int_{\Omega}|\boldsymbol{\nabla}\phi|^2a_s\frac{\partial w_{\phi}}{\partial x}\frac{\partial a_s}{\partial\left(\frac{\partial\phi}{\partial x}\right)}dV+\int_{\Omega}|\boldsymbol{\nabla}\phi|^2a_s\frac{\partial w_{\phi}}{\partial y}\frac{\partial a_s}{\partial\left(\frac{\partial\phi}{\partial y}\right)}dV=0 \tag{2.11b}$$

here, $\Omega=\Omega_s\cup\Omega_l$, where Ω_s is the solid phase and Ω_l is the liquid phase, respectively. The variations, ω_{u_c} and ω_{ϕ}, belong to $H^1(\Omega)$ - the Sobolev space of functions that are square-integrable and have a square-integrable derivatives.

2.2 Numerical implementation and results

This section outlines the numerical implementation of the phase-field models described in Section 2.1.2 and 2.1.4. In Section 2.2.1, computational implementation is covered. In Section 2.2.2, a summary is presented of the input model parameters used in the simulation of dendritic growth in a pure metal and a binary alloy, and along with list of the non-dimensional parameters used in these models. In Sections 2.2.3, using various dendritic morphologies modeled in this work, important geometric features of dendrites are identified that are tracked in the dendritic shape studies presented later. In Sections 2.2.4 classical four fold symmetric dendrite shape occurring in undercooled pure melt is simulated and then used as a basis for convergence studies of dendritic morphology and dendritic tip velocity. Later, in Sections 2.2.5-2.2.8, the evolution of complex 2D and 3D dendrite morphologies is modeled. These simulations cover various cases of solidification ranging from a single equiaxed dendrite in a pure liquid melt to a multi-columnar dendrites growing in a binary alloy. Finally, evolution of equiaxed dendrite in 3D is demonstrated.

2.2.1 Computational implementation

The phase-field formulations presented in this work are solved using computational implementations of two numerical techniques: (1) A C^0-continuous basis code based on the standard Finite Element Method (FEM); the code base is an in-house, C++ programing language based, parallel code framework with adaptive meshing and adaptive time-stepping - build on top of the deal.II open source Finite Element library (Arndt et al., 2021), (2) A C^1-continuous basis code based on the Isogeometric Analysis (IGA) method; the code base is an in-house, C++ programing language based, parallel code framework - build on top of the PetIGA open source IGA library (N. Collier, 2013). As can be expected, the IGA code base can model C^0-continuous basis also, but does not currently support some capabilities like adaptive meshing that are needed for 3D dendritic simulations. Both codes support a variety of implicit and explicit time stepping schemes. Following the standard practise in our group to release all research codes as open source (Wang et al., 2016; Jiang et al., 2016; Rudraraju et al., 2019), the code base of the current work is made available to the wider research community as an open source library (Bhagat, 2022b).

2.2.2 Material properties and non-dimensional quantities in solidification

The specific material properties and non-dimensional parameters used in the modeling of pure metal and binary alloys are described here. First, the case of dendrite growth in an undercooled melt of pure metal is considered, whose governing equations are given by Equations 4.1c and 4.1d. Undercooling of the liquid melt is responsible for driving dendrite growth in this case and there is no external imposition of a temperature gradient or a dendritic growth velocity. This is commonly referred to as free dendritic growth. The set of non-dimensional input parameters used in this model

and their numerical values (adopted from Karma and Rappel (1998)) are summarized in Table 4.1. Here, $\tilde{D}$ is the thermal diffusivity of heat conduction, ϵ_4 is the strength of interface surface energy anisotropy where the subscript indicates the assumed symmetry of the dendritic structure, and in this simulation, we consider a four-fold symmetry. The choice of the length-scale parameter λ_0, identified as the interface thickness, and the time-scale parameter τ_0 set the spatial and temporal resolution of the dendritic growth process. ξ is a coupling parameter representing the ratio of interface thickness and capillary length.

Non-dimensional parameter	Numerical value
Thermal diffusivity, $\tilde{D}$	1
Anisotropy strength, ϵ_4	0.05
Characteristic length-scale, λ_0	1
Characteristic time-scale, τ_0	1
Coupling parameter, ξ	1.60

Table 2.1: Input parameters for the phase-field model of solidification of a pure metal. The length-scale parameter λ_0 and the time-scale parameter τ_0 set the spatial and temporal resolution of the dendritic growth process.

Next the case of dendritic growth in binary alloys is discussed. As mentioned earlier, chemically, alloys are distinct from pure melts due to the presence of solute atoms of one or more alloying materials. During the solidification of alloys, solute diffusion plays a critical role. The coupled governing equations of solute diffusion and phase-field are given by the Equations 4.1e-2.10e. The solid-liquid interface is constrained with the imposition of the temperature gradient, G, and the pulling velocity, $\mathbf{v}_p$. We solve for two primal fields - composition undercooling, u_c, and the phase-field order parameter, ϕ. The input parameters used in the numerical model are given in Tables 4.2-4.3. The parameters listed in the Table 4.2 are the required material properties for modeling dendritic growth in a binary alloy (adopted from Zhu et al. (2019)): mass diffusivities D_l and D_s in the

Parameter	Numerical value (units)
Liquid phase diffusivity, D_l	2.4×10^{-9} $m^2 s^{-1}$
Solid phase diffusivity, D_s	1.15×10^{-12} $m^2 s^{-1}$
Partition coefficient, k	0.14
Anisotropy strength, ϵ_4	0.05
Gibbs-Thomson coefficient, Γ_g	2.36×10^{-7} m-K
Liquidus slope, m_l	-3.5 $K(wt\%)^{-1}$
Initial concentration, c_0	4wt%
Thermal gradient, G	3700 Km^{-1}
Pulling velocity, v_p	1.35×10^{-5} ms^{-1}
Interface thickness, λ_0	1.058×10^{-6} m
Model constant, a_1	0.8839
Model constant, a_2	0.6267

Table 2.2: Material properties and phase-field model parameters for a binary alloy Al-4wt.% Cu

Input parameters	Expression
Chemical capillary length, d_0	$\frac{k\Gamma}{mC_0(k-1)}$
Ratio of interface thickness to capillary length, Ξ	$\frac{\lambda_0}{d_0}$
Non-dimensional thermal diffusivity, $\tilde{D}$	$\frac{D_l \tau_0}{\lambda_0^2}$
Non-dimensional pulling velocity, $\tilde{v}$	$\frac{v\tau_0}{\lambda_0}$
Characteristic thermal length-scale, $\tilde{L_T}$	$\frac{\lvert m_l \rvert (1-k) c_0}{kG\lambda_0}$
Characteristic time-scale, τ_0	$\frac{a_1 a_2 \xi \lambda_0^2}{D_l}$
Coupling parameter, ξ	$a_1 \Xi$

Table 2.3: Input parameters for the phase-field model of solidification of a binary metallic alloy. The numerical values of the input parameters are computed using the expressions shown here that are in terms of the properties listed in Table 4.2.

solid and liquid phase, Gibbs-Thomson coefficient Γ_g, thermal gradient, G and pulling velocity v_p. Since here a generic dilute binary alloy is modeled, the temperature and composition phase diagram of a physical alloy is approximated by a linear relationship. This approximation is possible with assumption of the alloy to be a dilute binary alloy. This linearization of a temperature-composition relationship results in two more parameters: the partition coefficient k and the slope of the liquidus line m_l. An optimal choice of the phase-field interface thickness is made keeping in mind the computational tractability of the final numerical model. Table 4.3 lists the expressions used to calculate the input parameters relevant to the model.

2.2.3 Primary geometric features and shape variations in dendrite morphologies

Dendrites occur in a great variety of morphologies and orientations. One of most common, yet fascinating, occurrences of dendritic growth is in the formation of snowflakes that are dendritic structures with a distinct six-fold geometric symmetry. In more practical applications, as in the solidification of metallic alloys, dendritic shapes can be broadly classified as "columnar" or "equiaxed". Columnar dendrites grow into a positive temperature gradient, and the rate of growth is controlled by the constitutional undercooling of the liquid melt ahead of the dendritic tip. On the other hand, growth of an equiaxed dendrites in pure melt is controlled by the temperature undercooling of the surrounding liquid melt.

The schematic shown in Figure 2.2 depicts these possible variations in dendritic shapes, and also identifies important geometric features that are traditionally used by the Materials Science and Metallurgy community to quantify dendritic morphologies. At the top end of the schematic, shown is a equiaxed dendrite with a six-fold symmetry (one-half of the symmetric dendrite shown) that is typical of snowflakes and in certain alloy microstructures. At the bottom, shown are columnar dendrites with

their primary arms oriented parallel and inclined at a 30° angle to the vertical axis. These primary arms develop secondary arms as they evolve, and the separation of the primary arms (referred to as the primary dendrite arm spacing or PDAS) and secondary arms (referred to as the secondary dendrite arm spacing or SDAS) are important geometric characteristics of a given dendrite shape. Further, towards the right side of the schematic is a columnar dendrite colony growing homogeneously oriented along the horizontal axis, and shown towards the left side of the schematic are two time instances (separated by an interval Δt) of an equiaxed dendrite's interface evolution and the movement of the dendritic tip over this time interval is Δx. The dendritic tip velocity, a very important measure of dendritic kinetics, is then given by $\mathbf{v}_{\text{tip}} = \frac{dx}{dt}$. It is to be noted that all these morphologies were produced in simulations of various solidification conditions using the numerical framework presented in this work, and are but one demonstration of the capabilities of this framework in modeling complex dendritic morphologies.

2.2.4 Single equiaxed dendrite evolution

Growth of a single equiaxed dendrite in an undercooled melt of pure metal is a classical solidification problem, and much of traditional analysis of dendritic growth is based on reduced order models for this problem. The phase-field governing equations are given by Equations 4.2b-4.2c, and the primal fields solved for are the temperature undercooling u and the order parameter ϕ. These equations are solved using both a C^0 basis and a C^1 basis as part of the study of convergence with respect to variations in the spatial discretization. Input parameters used in this model have been listed in Section 2.2.2. Zero flux Boundary Conditions are considered on all the boundaries for the fields u and ϕ, and the Initial Condition is a uniformly undercooled liquid melt with $\Delta = -0.75$ everywhere. The phase-field order parameter is set to $\phi = -1.0$ everywhere, except a very

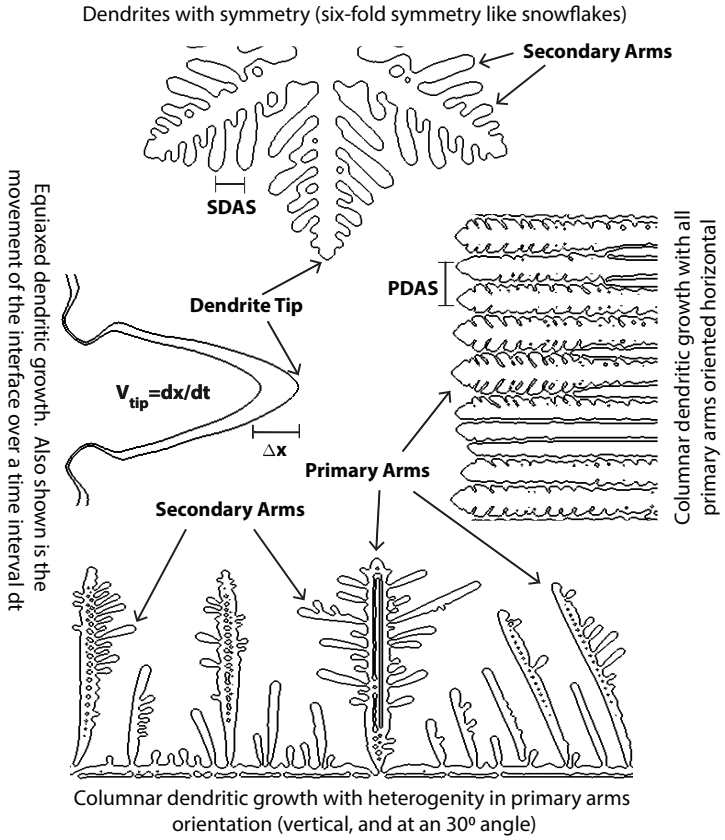

Figure 2.2: Schematic showing important geometric features used to quantify dendritic morphologies, and some typical variations of shapes and orientations in columnar and equiaxed dendrites. Shown are the primary arms and primary dendrite arm spacing (PDAS), secondary arms and secondary dendrite arm spacing (SDAS), and the movement of the dendritic tip by a distance Δx over a time interval Δt. Dendritic tip velocity is given by $\boldsymbol{\nu}_{\text{tip}}$. All these shapes were generated using the solidification numerical models presented in this work.

small circular region at the center representing a solid seed formed due to nucleation with $\phi = 1.0$ in the seed. Recollect that, in all the models, $\phi = 1.0$ represents the bulk solid and $\phi = -1.0$ represents the bulk liquid region and any value in between represents the diffuse interface between these two regions. The non-dimensional size of the domain is 500x500

and it is uniformly discretized into elements with a length measure of $\Delta x = 2.0$. The non-dimensional time step for the implicit time stepping scheme considered in this case is $\Delta t = 0.04$.

The growth of dendrites out of the nucleation point at the center is dictated by the degree of undercooling of the liquid melt. As solidification begins, the surrounding undercooled liquid melt is at lower temperature than the solid seed. As a result, the solid seed diffuses heat into the liquid region. Theoretically, the solid-liquid interface of an undercooled pure melt is always unstable, so small local numerical perturbations on circular solid seed interface begin to grow. Due to the assumption of strong anisotropy (four-fold symmetry) of the interface, perturbations to the interface grow rapidly along the favorable orientations as compared to the non-favorable orientations. Figure 2.3a represents u at a particular time, t = 840. Diffusion takes place over the entire stretch of the solid and liquid regions. From t = 0 to 840, u changes from the initial value of -0.75 as per the solution of the heat diffusion equation. It should be noted that the bulk of the liquid region and the solid dendrite are at a uniform temperature, and the temperature variations are mostly localized to the vicinity of the interface. The bulk liquid melt region shown in blue is at a low temperature and the bulk solid dendrite in red is at a high temperature, as seen in Figure 2.3a. The level set of $\phi = 0$ is identified as the distinct solid-liquid interface and the evolution of this interface is plotted in Figure 2.3b as a series of $\phi = 0$ level sets at different time instances. As can be seen, at t=0, the circular seed at the center of the domain, over time, evolves into a four-fold symmetric interface. At time, t = 840, a fully developed equiaxed dendrite shape can been seen. This Initial Boundary Value Problem is also simulated on C^1-continuous mesh and found identical spatiotemporal growth of the equiaxed dendrite.

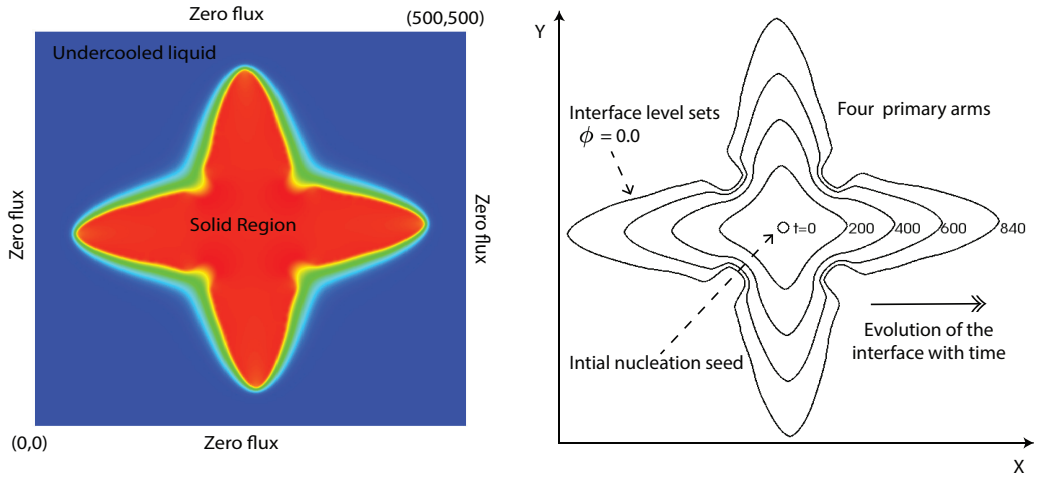

(a) Temperature contour at t=840 (b) Time evolution of the interface

Figure 2.3: Growth of a single equiaxed dendrite in an undercooled melt of pure metal. Shown are the (2.3a) Temperature contour (u) at t = 840, and (2.3b) Temporal evolution of the equiaxed dendrite interface, delineated by the level set $\phi = 0$, at different time instances.

Numerical convergence studies

In this section, the accuracy of the interface propagation numerical results for the single equiaxed dendrite case presented above is assessed. This is done by comparing the velocity of propagation of the dendritic tip with known analytical solutions of tip velocity for this problem, and also study the convergence of the tip velocity with mesh size and increasing continuity of the numerical basis.

Velocity of the dendritic tip: As can be seen in Figure 2.3, the phase-field model of solidification of a pure metal successfully produces the freely growing dendrite shape and four-fold symmetry as expected. However, predicting quantifiable features of the dendritic evolution would provide a better validation of the proposed numerical framework. In this context,

the dendritic tip propagation velocity (see Figure 2.2) for single equiaxed dendrites has been widely used in analytical studies of dendritic propagation. In the literature, implicit expressions for radius and velocity of the dendritic tip have been obtained using semi-analytical approaches, and they provide estimates of $\boldsymbol{\nu}_{\mathrm{tip}}$. One of the more popular semi-analytical approaches to obtain the tip velocity employs a Green's function (GF) approach. The Green's function is an integral kernel that is widely used to solve of certain classes of differential equations. This approach is not discussed here, but only use the dendritic tip velocity values predicted by this approach. These values are denoted by $\boldsymbol{\nu}_{\mathrm{tip}}(\mathsf{GF})$. Interested readers are referred to Karma and Rappel (1998) for details of the GF approach.

The model parameters used in this study are $\Delta = -0.65$, $\epsilon_4 = 0.05$, $\tilde{D} = 1$, $d_0/\lambda_0 = 0.544$, $\lambda_0 = 1$, $\tau_0 = 1$, $\xi = 1.596$. The numerical domain size and time step size, in dimensionless units, are 500x500 and $\Delta t = 0.04$, respectively. An implicit (backward Euler scheme) time-stepping method for this study is chosen, and the time step size, Δt, was chosen considering stable quadratic convergence of the relative residual error for the implicit time stepping scheme. Further, this time step size is comparable to the values reported in the finite difference method literature for this problem (Karma and Rappel, 1998). For these values, the Green's function approach predicts an equilibrium tip velocity, $\boldsymbol{\nu}_{\mathrm{tip}}(\mathsf{GF}) = 0.0469$. Freely growing equiaxed dendrite in an infinite domain, under solidification conditions held constant over time, attains a fixed equilibrium tip velocity. In this study, the effect of two discretization parameters is considered, namely: (1) Comparison of the numerical dendritic tip velocity ($\boldsymbol{\nu}_{\mathrm{tip}}$) to the equilibrium tip velocity obtained from Green's function approach $\boldsymbol{\nu}_{\mathrm{tip}}(\mathsf{GF})$ (Figure 2.4), and (2) Convergence of the tip velocity ($\boldsymbol{\nu}_{\mathrm{tip}}$) with mesh refinement, and its dependence on the order of continuity of the basis (Figure 2.5).

The method of estimating the dendrite tip velocity from the numerical

simulations using the computational frameworks described above is described briefly. Simulations were performed using both a C^0-continuous basis and a C^1-continuous basis, to study the effect of basis continuity when resolving fine dendritic morphologies. The dendritic tip velocity measurement is done manually as a post-processing of the phase-field order parameter contours of the numerical simulations. At each time instance, the zero level set ($\phi = 0$) is plotted using a visualization tool for FEM output, Visit (Vis, 2012). The tip of the zero level set of the order parameter is manually tracked, and the velocity of tip propagation at each time instance is computed using a simple finite difference estimate of the derivative $\boldsymbol{\nu}_{tip} = \frac{dx}{dt}$. The criteria for choosing the zero level set to represent the interface is a standard practice in the dendritic modeling literature (Boettinger et al., 2002; Gibou et al., 2003). As can be seen from Figure 2.4, after a non-dimensional time of 1500, for all the cases we considered, the estimated tip velocity at any time instant is within 10% of the theoretical tip velocity, with 10% being the upper bound for the coarsest C^0-continuous mesh. Thus, for the error estimates, the tip velocity at t = 1500 is considered. At time t=2000 the dendrite approaches the edge of the computational domain. Two sources of error can potentially cause minor variations to the computed velocity values. The first source of error arises from not picking the exact tip location in subsequent time snapshots as the dendrite interface shape is evolving with time. The second source of error arises due to the use of only C^0 interpolation of the nodal solutions inside the elements by the visualization tool. This error is significant for C^1-basis, as the results are C^1-continuous but the visualization of the results inside the elements is only C^0-continuous. As can be seen in Figure 2.4, $\boldsymbol{\nu}_{tip}$ starts to approach the Green's function value, $\boldsymbol{\nu}_{tip}(GF)$, across all the simulations, but shows better convergence to the Green's function value for the C^1-continuous basis. Further, the percentage error of $\boldsymbol{\nu}_{tip}$, given by Error$= \frac{|\boldsymbol{\nu}_{tip} - \boldsymbol{\nu}_{tip}(GF)|}{\boldsymbol{\nu}_{tip}(GF)}$, consistently reduces with a decrease in the mesh

size across both C^0-continuous and C^1-continuous basis, as shown in Figures 2.5(a) and 2.5(b). This is an important numerical convergence result, as to the best of our knowledge, this is the first time convergence rates have been demonstrated for non-trivial dendritic shape evolution with respect to mesh refinement. The convergence rates are demonstrated in the plot in Figures 2.5(a), where the rate of convergence (slope of the percentage Error vs mesh size plot) is close to two for a C^0-continuous basis, and close to three for a C^1-continuous basis. While obtaining theoretical optimal converge rates with respect to h-refinement of the discretization for this coupled system of parabolic partial differential equations is very challenging, one can observe that the convergence rates shown are comparable to the optimal convergence rates of classical heat conduction and mass diffusion partial differential equations (Bieterman and Babuška, 1982). This completes the estimation of error in $\boldsymbol{\nu}_{\mathrm{tip}}$, which is a measure of localized error in the order parameter field, as the dendritic interface is given by the zero level set of the order parameter field. Now the errors over the entire domain for both the temperature field and the order parameter field are estimated.

Error convergence of the temperature and order parameter fields: For this study, three different mesh refinements of a C^0-continuous basis are considered. For each of these refinements, the computational domain size is 160x160, chosen time step is $\Delta t = 0.12$, and the other input parameters are as given in Table 4.1. An implicit (backward Euler scheme) time-stepping method for this study is chosen, and the time step size, Δt, was chosen considering stable quadratic convergence of the relative residual error for the implicit time stepping scheme. Further, a time-step size smaller than the value considered does not yield any significant improvement in the error computations is also verified. As the Initial Condition, a small nucleation seed was considered, and this seed grows into the

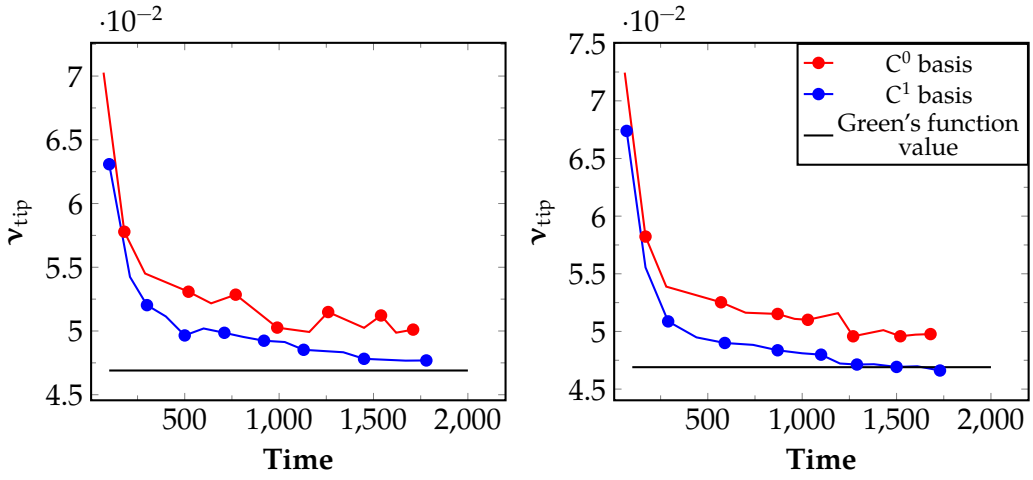

(a) Δx=2.0 (b) Δx=1.0

Figure 2.4: Comparison of the numerical and analytical (Green's function approach) dendritic tip velocities over time during growth of a single equiaxed dendrite for two different mesh sizes (Δx), and for both C^0-continuous and C^1-continuous basis.

surrounding undercooled melt. For the problem of interest, there are no known analytical solutions for the fields u or ϕ. As mentioned in the earlier subsection, the only analytical result available is for the equilibrium dendritic tip velocity. Thus, a computational approach to obtain the reference solution of both the primal fields is followed. A separate problem is solved on a very fine mesh ($\Delta x = 0.2$) using the popular open source phase field library PRISMS-PF (DeWitt et al., 2020), and the primal field solutions for this very fine mesh are considered the reference solutions. It is to be noted PRISMS-PF library is being successfully used by the wider Materials Science community to solve numerous phase-field problems. The mesh size of $\Delta x = 0.2$ for the reference solution was arrived at by performing a convergence study of the total free energy with respect to the mesh refinement, and noting the mesh size below which the rate of change of free energy with respect to mesh refinement nearly plateaued.

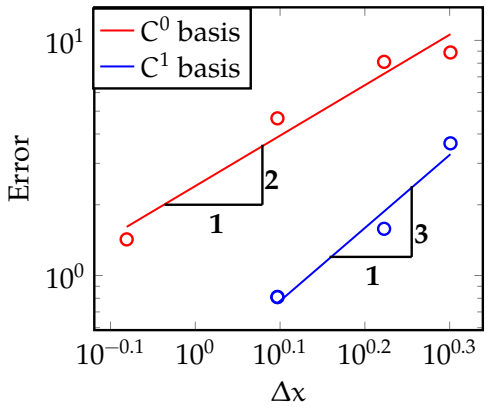

(a) Convergence of error in dendritic tip velocity with mesh refinement.

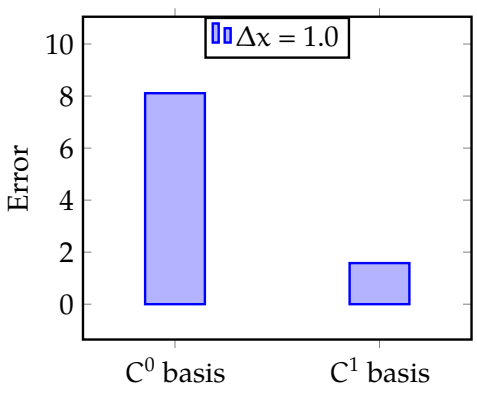

(b) Comparison of error in dendritic tip velocity for a mesh size of $\Delta x = 1.0$

Figure 2.5: Convergence of the percentage error in dendritic tip velocity, given by Error=$\frac{|v_{tip} - v_{tip}(GF)|}{v_{tip}(GF)}$, with mesh refinement and its dependence on the continuity of the basis. The C^0 basis is chosen to be first order (Linear), and the C^1 basis is chosen to be second order (Quadratic). Subplot (a) shows rate of error convergence ($\epsilon = \mathcal{O}(\Delta x)^{order+1}$) with respect to mesh refinement in a log-log plot. Subplot (b) shows the difference in percentage errors between a C^0-continuous basis and a C^1-continuous basis for one mesh size.

Using this numerical reference solution, error in the temperature and order parameter fields of the solutions obtained for the numerical formulations presented in this work, is calculated by comparing the fields and their gradients using two types of norms relevant to the problem, and for three different mesh refinements at one instance of time (time = 450) when the dendritic shape is well established. The two error norms used in this analysis are the L_2-norm and the H_1-norm, and these are defined as follows:

$$|u - \hat{u}|_{L_2} = \sqrt{\int_\Omega |u_h - \hat{u}|^2 \, dV} \tag{2.12a}$$

$$|u - \hat{u}|_{H_1} = \sqrt{\int_\Omega \left(|u_h - \hat{u}|^2 + |\nabla u_h - \nabla \hat{u}|^2 \right) \, dV} \tag{2.12b}$$

Here, u_h is the finite element solution under consideration and $\hat{u}$ is the reference numerical solution. The integral is defined over the entire numerical domain, so the estimated error, unlike the previous error in tip velocity, is not localized to any particular region in the domain. The convergence of this error in these two norms with mesh refinement is shown in Figure 2.6 on a log-log scale. As can be seen from these plots, a good convergence in both the norms for both the primal fields, with the rates of convergence being in the vicinity of 1.5 to 2.0 is observed. In this work, the error convergence for each of the primal fields is chosen to be studied separately. Given that this is a coupled problem in two primal fields, it is possible to construct a single L_2-norm and H_1-norm that accounts for both the fields. For example, $\sqrt{\int_\Omega (|u_h - \hat{u}|^2 + |\phi_h - \hat{\phi}|^2) \, dV}$ for a unified L_2-norm of the error in both the fields. We are not aware of any theoretical optimal error estimates in any of the relevant error norms for this problem, so this numerical strategy to obtain error estimates is seen as filling this vital gap by providing numerical convergence studies, thus permitting the numerical error convergence analyses of these governing equations.

2.2.5 Growth of multiple equiaxed dendrites

In Section 2.2.4, one particular type of dendritic growth, namely the evolution of a single equiaxed dendrite during the solidification of pure metal is discussed. Now the evolution of multiple equiaxed dendrites during the solidification of a more complex binary alloy solution is modeled. The input parameters for the model are listed in Table 4.2. Growth of multi-equiaxed dendrites during solidification of a binary alloy is governed by the Equations 4.2d-4.2e. The primal fields in this problem are the non-dimensional composition, u_c, and the phase-field order parameter, ϕ. As

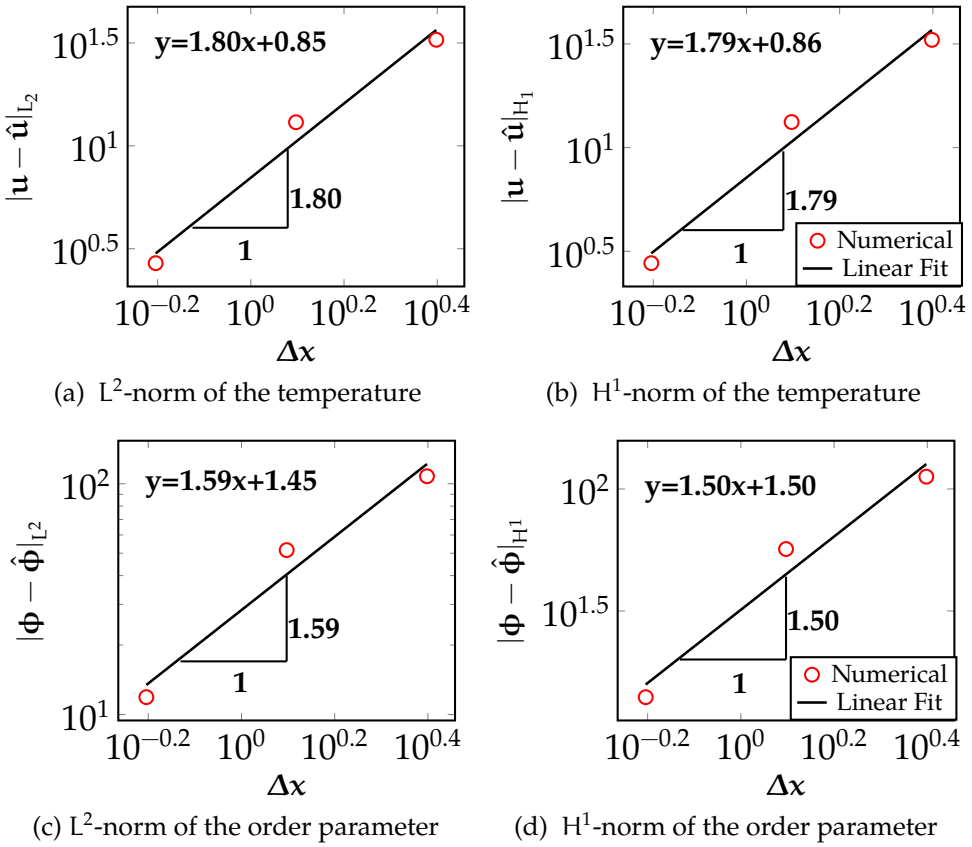

(a) L^2-norm of the temperature

(b) H^1-norm of the temperature

(c) L^2-norm of the order parameter

(d) H^1-norm of the order parameter

Figure 2.6: Error estimates and order of convergence for the primal fields (u, ϕ) shown on log-log plots. The error norms used in this study are the L_2-norm and the H_1-norm of (u, ϕ). A first order C^0-continuous basis is used for this study. The equation of the linear fit shown is noted in each plot.

an Initial Condition for this problem, multiple small nucleation seeds are randomly distributed in the numerical domain. The seed locations are completely random, and generated using a random number generator. To ensure free equiaxed dendritic growth, thermal gradient G and pulling velocity $\mathbf{v}_p$ is taken to be zero. The numerical domain of size 600x600 is subdivided into uniform elements with a length measure of $\Delta x = 1.2$. The time step size is $\Delta t = 0.005$. The average alloy composition in the entire

domain is taken to be $c_0 = 4\%$, which corresponds to $u_c = 0$. Nucleation seeds of the solid phase are randomly placed such that $\phi = 1$ inside of the seed and $\phi = -1$ outside of the seed. Zero flux Boundary Conditions are considered for both the fields. During the metal casting process, many solid nuclei are randomly formed near cavities or defects on the surface of a mold. These nuclei then start to grow in an equiaxial manner with neighboring nuclei competing with each other. This competition can shunt the growth of dendrites approaching each other. Solution contours of the fields u_c and ϕ are shown in the Figure 2.7. Here, Subfigure 2.7a shows the solute composition in the numerical domain at t = 40. Initially, the entire domain is at an alloy concentration of 4%. Due to negligible mass diffusivity in the solid phase, solute diffusion primarily takes place in the liquid region. A solute composition of $c_0 = 4\%$ is highest near the interface, and as one moves away from the interface, the solute concentration decreases. This is apparent in all the dendritic interfaces shown in the Subfigure 2.7a. Solute composition inside the solid is given by $c_0 = 0.56$ and it stays constant due to low negligible diffusivity in the solid region. Subfigure 2.7b demonstrates the competition between the dendrites growing out of the various seeds, the interaction of the dendritic tips, and the growth of secondary dendrite arms. Material properties of an alloy are often correlated with fine-scale microstructure length scales (at the grain scale and sub-grain scale), and the secondary dendrite arm spacing (SDAS) is one of the important microstructural properties of alloys.

2.2.6 Growth of single columnar dendrites

In this section, the growth of columnar dendrites, growing from a single seed during the solidification of a binary alloy is demonstrated. The numerical model and input parameters used in this case are identical to the previous Section 2.2.5. The notable difference from the model in Section 2.2.5 to the current model is the imposition of constraints like non-

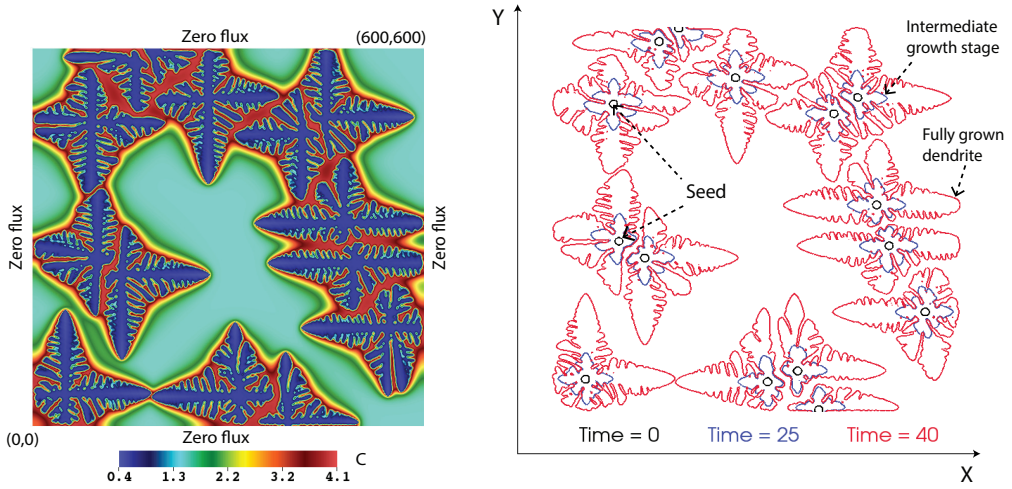

(a) Composition (b) Zero level sets of the order parameter

Figure 2.7: Growth of multiple equiaxed dendrites. Shown are the (2.7a) contours of solute composition, c, at time t = 40, and (2.7b) Time evolution of multiple equiaxed dendrite interfaces at time t = 0, 25 and 40. The dendrite interfaces are the zero level sets of the order parameter, $\phi = 0.0$.

zero thermal gradient G and pulling velocity ν_p. Initially, a single solid seed is placed at the bottom of the numerical domain. The entire domain is at a solute composition of $c_0 = 4\%$ which corresponds to the composition undercooling of $u_c = 0$. Zero flux Boundary Conditions are enforced on both the primal fields, u_c and ϕ. Figure 2.8 depicts the evolution of the composition field, and the dendritic interface as a function of time. The temperature gradient (G) applied is in the vertical direction. As opposed to the solidification in an undercooled pure metal, the liquid phase in this type of solidification is at a higher temperature than the dendrite in a solid phase. Any numerically localized perturbation to the solid-liquid interface will grow as per the degree of constitutional undercooling. For the given temperature gradient G and pulling velocity ν_p, the solid-liquid interface is unstable. This is evident from the interface $\phi = 0$ evolution captured in the Subfigure 2.8b. At t = 0, the solid seed starts to grow. By t = 35,

the solid seed has developed four primary branches due to the four-fold symmetry in the anisotropy considered. The growth of only three primary arms is captured in the simulation and the fourth arm pointing downward is not a part of the computation. These three primary arms have developed secondary arms of their own as seen in contour. By t = 40, the initial seed has grown into a larger size dendrite and several of its secondary arms are growing in the columnar fashion aligning with the direction in which constraints are applied, i.e, vertically. The phenomenon of secondary arms growing in the vertical direction becomes more obvious by t = 45 and t = 50 as seen in the Subfigure 2.8b. The diffusion of the solute is governed by the same mechanism discussed in Section 2.2.5. Like Subfigure 2.7a, in this case as well, the solute composition is maximum near the dendrite interface and it decreases as one moves away from the interface. This is clearly shown in the Subfigure 2.8a.

2.2.7 Growth of multiple columnar dendrites

Columnar dendrites growing out of a flat boundary are the next type of dendrites modeled. This type of dendrites occur in directional solidification processes which are of significance in manufacturing of alloy components by use of molds, where often the dendrite growth is primarily columnar. The characteristic of the columnar dendrites are the growth of a colony of dendrites along the direction of the imposed temperature gradient and the pulling velocity. These dendrites then move at a steady-state tip velocity which is determined by the pulling velocity. The other geometric features of columnar dendrites which are typically observed in the experimental studies include primary arms, secondary arms, spacing between arms, growth competition between the neighboring dendrites, and the interaction of the diffusion field between neighboring dendrites. The growth of multi-columnar dendrites is governed by the same governing equations that were used to model the solidification of a binary

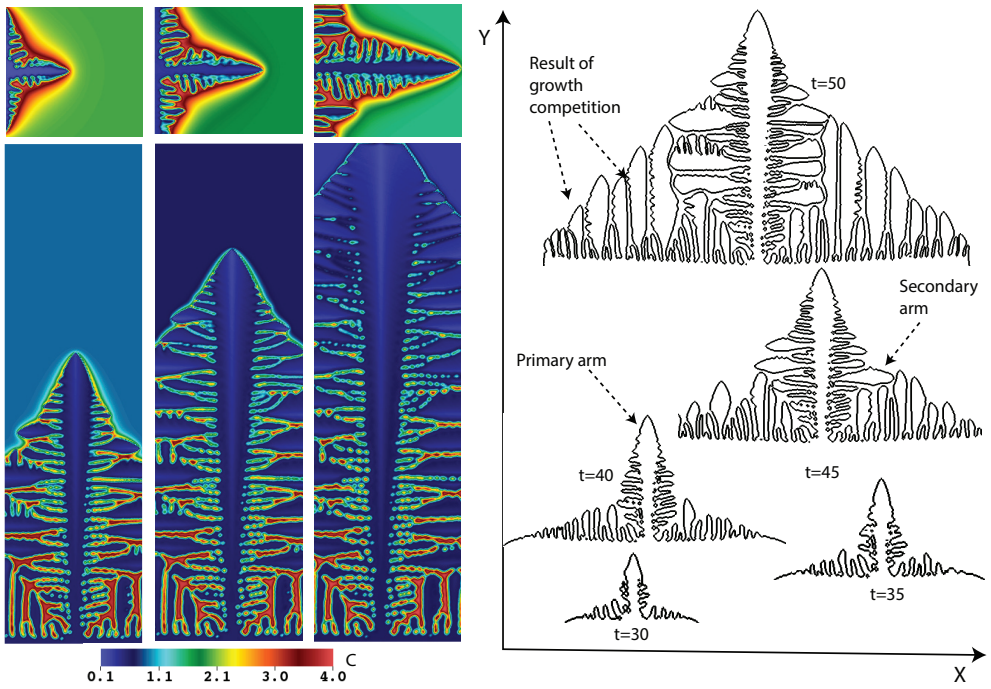

(a) Composition (b) Zero level sets of the order parameter

Figure 2.8: Growth of a single columnar dendrite. Shown are the (2.8a) contours of solute composition, c, at different time instances, and (2.8b) Time evolution of single columnar dendrite interfaces at times t = 30 to 50.

alloy in the previous Section 2.2.4-2.2.5, and so are the input parameters. However for the Initial Condition, an initial thin layer of solid solute on one of the boundaries is taken, and $\phi = 1$ is set inside the initial solute layer thickness and $\phi = -1$ is set in rest of the domain. Non-dimensional composition undercooling is set to $u_c = -1$ everywhere in the domain. For the Boundary Conditions, zero flux conditions are enforced on the boundaries for both the primal fields u_c and ϕ. Figure 2.9 depicts the results of multiple columnar dendritic growth. As can be seen, the phase-field contour interface ($\phi = 0$) at time, t= 240, fills the entire domain with a colony of columnar dendrites. The initial planar interface with a solute composition seeds the dendrites that then compete to evolve into this

columnar dendritic structure. The emergence of seven primary arms of the dendrites, as seen in Subfigure 2.9b, is the result of the competition for growth among several more initial primary arms of dendrites. Some of these underdeveloped arms can be seen in the lower portion of the figure. The primary arm spacing between these seven primary arms appears to converge to a constant value with the progress of the dendrites. Another feature of the columnar dendrites that were captured is the growth of the secondary dendrite arms and their orientation. The concentration of the solute in the solid region is nearly uniform at a value of 0.56. The region surrounding these solid dendrites consists of the liquid melt where the highest concentration is about 4.0. Due to mass diffusion, there exists a gradient in the solute concentration in the liquid melt as can be seen in the Subfigure 2.9a.

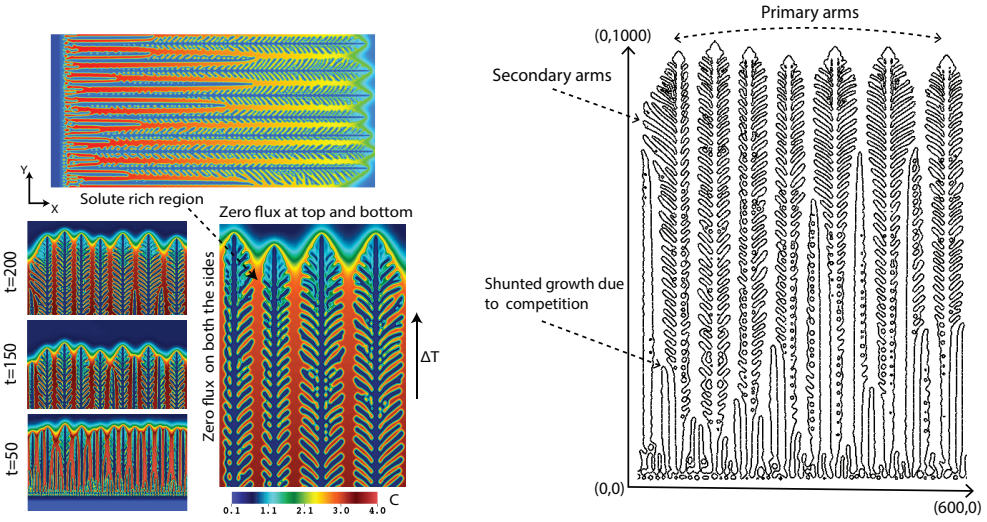

(a) Composition (b) Zero level sets of the order parameter

Figure 2.9: Growth of multiple columnar dendrites. Shown are the (2.9a) Contours of the solute composition, c, at time t = 240, and (2.9b) Growth profile of multiple columnar dendrite interfaces at time t = 240.

2.2.8 Three dimensional growth of single equiaxed dendrite

The phase-field model described by the Equations 4.1c-4.1d in three dimensions is now simulated. The initial solidification conditions consist of a small spherical seed placed in a $500 \times 500 \times 500$ computational domain with an adaptive mesh and the smallest element length measure of $\Delta x = 2.0$ and uniform time step $\Delta t = 0.12$. The seed is placed in an undercooled melt of pure metal. The input phase-field parameters used in the simulation are listed in Table 4.1. The evolution of a spherical seed into a four-fold symmetric dendrite structure is shown in the Figure 2.10. The fully grown dendrite in blue at the end of the evolution has six primary arms as dictated by the surface anisotropy. The distribution of an undercooling temperature u on a fully grown dendrite, shown in red, can also be seen in the figure. Three dimensional implementation of phase-field models of dendrites is computationally very demanding, due to the need to resolve the fine scale primary-arm and secondary-arm structures. To make this problem computationally tractable, we use local mesh adaptivity (h-adaptivity), implicit time-stepping schemes with adaptive time-step control, and domain decomposition using MPI.

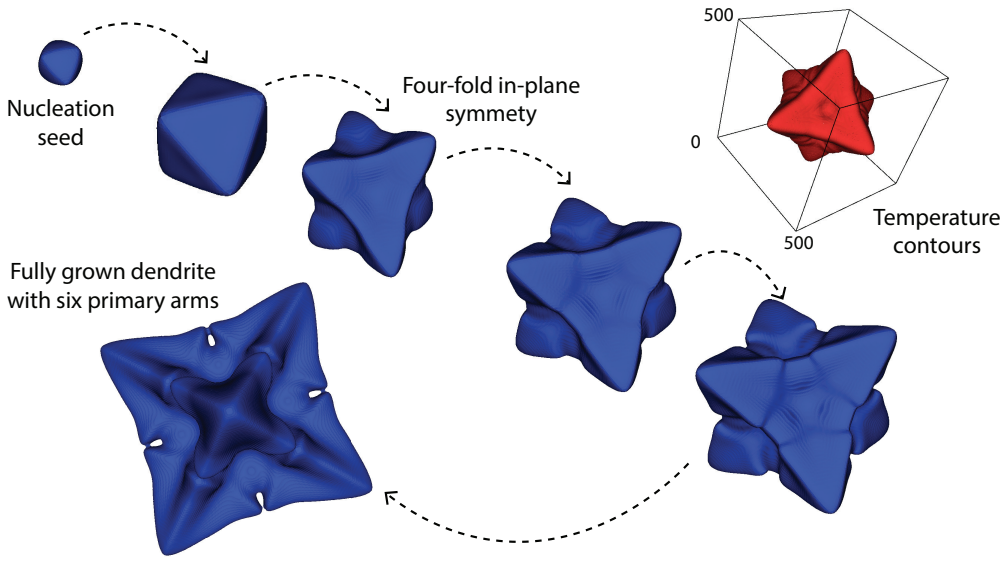

Figure 2.10: Evolution of a 3D single equiaxed dendrite. The dendritic structures shown in blue are the time evolution of the contours of the phase-field parameter, ϕ, and the dendritic structure shown in red is the contour of the undercooling temperature, u, at one time instance.

3 MULTI-PHYSICS MODELING OF MELTPOOL DYNAMICS IN METAL ADDITIVE MANUFACTURING

The outline of this chapter is as follows: Section 3.1 introduces the governing equations of the LPBF process in their dimensional and non-dimensional forms, along with the corresponding numerical formulation suitable to be solved using the Finite Element (FE) method. Section 3.2 covers the validation of FE-based implementation of the LPBF thermo-fluidic model with experimental results and numerical results from the literature. In Section 3.3, an empirical analysis based on linear least-squares regression is described to identify an important dimensionless quantity that is interpreted as a measure of heat absorbed by the powdered material and the resulting meltpool. An important relationship is then identified relating the measure of heat absorbed by the meltpool and classical dimensionless quantities relevant to the thermo-fluidic governing equations of the LPBF.This is followed by a presentation of simulation results in Section 3.4, including a discussion on the effects of the dimensionless quantities on the meltpool morphology and the resulting microstructure.

3.1 Governing equations of the LPBF process

3.1.1 Thermo-fluidic model of the LPBF process

[1] A discussion of the processes underlying the LPBF relevant to the thermo-fluidic model is outlined in this section. The schematic in Figure 3.1 shows an outline of the LPBF process. In LPBF, a recoater spreads a metal powder layer on top of the powder bed or partially built part that is enclosed in

[1] The work presented in Chapter 3 has been published as: Kunal Bhagat and Shiva Rudraraju, "A numerical investigation of dimensionless numbers characterizing meltpool morphology of the laser powder bed fusion process.", Materials 2023, 16(1), 94.

an inert environment. A high-intensity laser scans over this powder layer, causing localized melting and fusion of the melted powder on top of the partially built part. At the macro-scale or part-scale, this laser irradiation of the metal powder results in the formation of a *meltpool* (also referred to as *molten pool* or *melting pool* in the literature) of the liquified metal, that subsequently solidifies. This solidification of the meltpool is driven from the mesoscale, where the liquid melt undergoes a phase transformation to a solid phase, but the solidification is spatially heterogeneous and leads to the formation of dendritic structures and eventually the grain-scale microstructure. The formation of dendrites, their morphology, and the related numerical models have been extensively treated by the authors in a recent publication Bhagat and Rudraraju (2022). In this work, *part-scale*

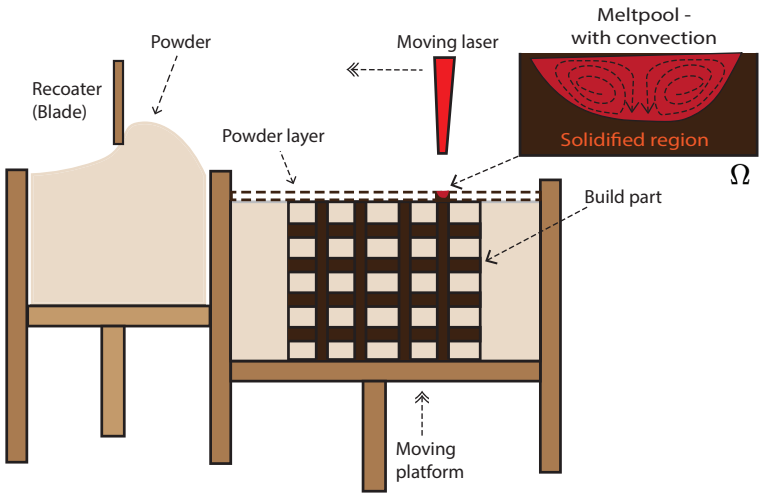

Figure 3.1: Schematic depicting the part-building process in Laser Powder Bed Fusion (LPBF). Laser irradiation on the powdered material causes localized melting and fusion of the metal powder on top of the partially built part. The localized melting results in a small pool of liquified metal referred to as the *meltpool*. Shown in the inset figure are the state of the powder under the laser - with the newly solidified region and a meltpool with convective flow of the liquified metal, and this region comprises the computational domain (Ω) of the numerical model presented in this work.

and the thermo-fluidic processes that are relevant in the meltpool and its immediate vicinity are considered. The processes modeled, with varying fidelity, are the movement of the laser-powered heat source, powder melting, convective flow in the meltpool, heat diffusion, and convective and radiation losses. These processes and their thermo-fluidic effects can be captured by coupled partial differential equations solving for the thermal distribution and the velocity distribution in the meltpool (Mukherjee et al., 2018).
The governing equations of heat transfer are as follows:

$$\rho c \frac{\partial T(\mathbf{x}, t)}{\partial t} + \rho(\boldsymbol{\nu}.\boldsymbol{\nabla})T(\mathbf{x}, t) = \boldsymbol{\nabla} \cdot k\big(\boldsymbol{\nabla} T(\mathbf{x}, t)\big) + S_\phi + S_p, \quad \mathbf{x} \in \Omega \quad (3.1a)$$

Equation 3.1a is solved for thermal conduction over the domain Ω (see Figure 3.1). T and $\boldsymbol{\nu}$ are the temperature and velocity, respectively, and are the primal fields of the governing equations. All through this work, vector quantities like velocity and the gradient operator, $\boldsymbol{\nabla}$, are shown in bold to distinguish them from other scalar quantities.

S_p is the heat input from the laser and S_ϕ is the latent heat released by the metal. ρ, c, k represent density, specific heat capacity, and the thermal conductivity of the material, respectively, and these can be constant or temperature dependent. Melting of the metal powder consumes latent heat, which is represented by source term, $S_\phi = -\rho(\boldsymbol{\nu}.\boldsymbol{\nabla})\phi - \rho L(\frac{\partial \phi}{\partial t})$. Here the liquid fraction, ϕ, determines the state of the material. $\phi = 0$ represents the solidified region, $\phi = 1$ represents the liquid, and $0 < \phi < 1$ represents the mushy zone region (Brent et al., 1988). The liquid fraction is a function of the temperature of the material and is given by the hyperbolic function: $\phi = \frac{e^{\xi}}{e^{\xi}+e^{-\xi}}$, where $\xi = \frac{\lambda(T-0.5T_m)}{T_l-T_s}$ and $T_m = \frac{1}{2}(T_l + T_s)$. λ is a constant that represents the solid-liquid interface thickness, T_s, and T_l are the solidus and the liquidus temperature of the material, respectively. The shape of the laser beam is modeled as an axisymmetric Gaussian profile, and the moving laser power is modeled using a source term, $S_p =$

$\frac{\alpha\omega P}{\pi r_p^2 l_p} \cdot e^{\left(-\frac{f(x-v_p t)^2}{r_p^2} - \frac{fy^2}{r_p^2} - \frac{fz^2}{l_p^2}\right)}$, where P is the laser power, α is the absorptivity, f is the distribution factor, r_p is the laser spot size, l_p is the powder layer thickness, and v_p is the laser scan speed.

Effectively, thermal conduction, powder melting due to the moving laser, and the formation of a liquid meltpool are modeled. Inside the meltpool, heat diffusion, along with the advection and convection effects of the fluid flow are considered. Convection inside the meltpool is a result of the competition between the surface tension and the buoyancy effects, but the surface tension driven flow dominates inside the meltpool (Kumar and Roy, 2009). The governing equations for the fluid flow, accounting for the conservation of mass and momentum, are given by,

$$\nabla.\mathbf{v}(\mathbf{x},t) = 0, \quad \mathbf{x} \in \Omega \tag{3.1b}$$

$$\rho\frac{\partial \mathbf{v}(\mathbf{x},t)}{\partial t} + \rho(\mathbf{v}(\mathbf{x},t).\nabla)\mathbf{v}(\mathbf{x},t) = -\nabla \mathbf{p} - \frac{180\mu}{d_\phi^2}\frac{(1-\phi)^2}{\phi^3+\delta}\mathbf{v}(\mathbf{x},t) \tag{3.1c}$$
$$+\nabla.\big(\mu\nabla\mathbf{v}(\mathbf{x},t)\big) + \beta\mathbf{g}(T - T_s)$$

This equation also accounts for advective and diffusive transport, buoyancy-induced flow, and the pressure drop due to the mushy zone (modeled as a porous zone) (Brent et al., 1988). Here, β is the expansion coefficient, T_s is the solidus temperature, μ is the dynamic viscosity, d_ϕ is the characteristic length scale of the porous mushy region, and δ is a very small parameter to avoid division by zero when $\phi = 0$ (solid region). Integral form of governing equations introduced in the Section 3.1.2 are given by Equations 3.2a-4.2a. As will be seen in the integral form, the surface integrals therein also account for the surface tension-induced flow and losses to the inert surroundings. This is captured by the inclusion of the convective and radiation heat losses, Marangoni convection from the top surface of the domain, Ω. At the bottom surface, temperature is fixed to ambient temperature. To limit the modeling complexity, in this otherwise

highly coupled multiphysics environment, mechanical deformation of the solidified region and keyhole formation is neglected.

3.1.2 Non-dimensional formulation of the governing equations

In this section, a dimensionless framework is constructed that exploits the powerful idea of the Buckingham-π theorem. The LPBF process consists of several process parameters and the thermo-fluidic model that helps us build an understanding of the complex interaction between several of these process parameters. The dimensionless framework facilitates combining several of these dimensional parameters into fewer dimensionless independent quantities. These dimensionless parameters then present key details of the complex additive process such as LPBF in fewer numbers of variables. The classical Buckingham-π theorem (Yarin, 2012) provides a mathematical basis for reducing the parameter dimensionality of the equations and helps group the parameters in the governing equations into a fewer number of non-dimensional and distinct quantities. This reduction follows from the application of the Rank-Nullity theorem (Curtis et al., 1982; Bluman and Kumei, 2013). Further, as will be discussed in later sections, the Finite Element Method (FEM) is employed to solve the governing equations considered in this work.FEM is a widely used numerical method that solves partial differential equations posed in their weak formulation (integral formulation). The dimensionless version of the governing equations that results from the application of the Buckingham-π theorem are worked with in their weak form as that is more suitable for obtaining numerical solutions using FEM.

Weak formulation

In this section, the process of non-dimensionalization of the governing equations given by Equation 3.1(a-c) is discussed. For the process of non-dimensionalization, the laser scan velocity, $\mathbf{v}_p$ is chosen as the characteristic velocity in the system, and the non-dimensional velocity in the meltpool is then given by $\tilde{\mathbf{v}} = \frac{\mathbf{v}}{\mathbf{v}_p}$. The thickness of the powder layer, l_p, is chosen as the characteristic length, and this leads to the characteristic time, given by $t_p = \frac{l_p}{\mathbf{v}_p}$. Now, the non-dimensional time and length are given by $\tilde{t} = \frac{t}{t_p}$ and $\tilde{x} = \frac{x}{l_p}$, respectively. Further, the non-dimensional temperature is chosen to be $\tilde{T} = \frac{T - T_\infty}{T_l - T_\infty}$, where T_l and T_∞ are the liquidus temperature of the metal and the ambient temperature of the inert surroundings, respectively. The characteristics value of the pressure is chosen to be $\rho \mathbf{v}_p^2$. A list of the dimensionless variables used in this model are summarized in Table 3.1. Using these scaled quantities, the dimensional strong (differential) form of the governing equations given by Equation 3.1(a-c) are converted into their corresponding dimensionless weak (integral) form. Following the standard variational procedure of deriving the weak formulation of the governing equations from their strong form (Hughes, 2012), the following weak formulations are obtained that are suitable for solving using FEM. Find the primal fields, $\{\tilde{T}, \tilde{\mathbf{v}}\}$, where,

$$\begin{aligned}
&\tilde{T} \in \mathscr{S}_T, \quad \mathscr{S}_T = \{\tilde{T} \in H^1(\Omega) \mid \tilde{T} = \tilde{T}' \; \forall \, \mathbf{x} \in \partial\Omega_D^T\}, \\
&\tilde{\mathbf{v}} \in \mathscr{S}_{\mathbf{v}}, \quad \mathscr{S}_{\mathbf{v}} = \{\tilde{\mathbf{v}} \in H^1(\Omega) \mid \tilde{\mathbf{v}} = \tilde{\mathbf{v}}' \; \forall \, \mathbf{x} \in \partial\Omega_D^{\mathbf{v}}\}
\end{aligned}$$

such that,

$$\begin{aligned}
&\forall \; \omega_T \in \mathscr{V}_u, \quad \mathscr{V}_T = \{\omega_T \in H^1(\Omega) \mid \omega_T = 0 \; \forall \, \mathbf{x} \in \partial\Omega_D^T\}, \\
&\forall \; \boldsymbol{\omega}_{\mathbf{v}} \in \mathscr{V}_\phi, \quad \mathscr{V}_\phi = \{\boldsymbol{\omega}_{\mathbf{v}} \in H^1(\Omega) \mid \boldsymbol{\omega}_{\mathbf{v}} = 0 \; \forall \, \mathbf{x} \in \partial\Omega_D^{\mathbf{v}}\}
\end{aligned}$$

the integral form is given as follows,

$$\int_{\Omega} \omega_T \Big(\frac{\partial \tilde{T}}{\partial \tilde{t}} + \tilde{\mathbf{v}}.\tilde{\boldsymbol{\nabla}}\tilde{T} \Big) d\Omega$$

$$+ \int_{\Omega} \boldsymbol{\nabla}\omega_T . \Big[\frac{1}{\mathbf{Pe}} \Big] \tilde{\boldsymbol{\nabla}}\tilde{T} d\Omega + \int_{\Omega} \omega_T \Big[\frac{\mathbf{Tc}}{\mathbf{Ste}} \Big] \Big((\tilde{\mathbf{v}}.\tilde{\boldsymbol{\nabla}})\tilde{\phi} + \frac{\partial \tilde{\phi}}{\partial \tilde{t}} \Big) d\Omega$$

$$- \int_{\Omega} \omega_T \frac{\alpha d}{\pi \tilde{r}^2 \tilde{l}} \Big[\mathbf{Q} \Big] \exp(\tilde{x}, \tilde{y}, \tilde{z}) d\Omega + \int_{\partial \Omega_N^T} \omega_T \Big(\Big[\frac{\mathbf{Bi}}{\mathbf{Pe}} \Big] \tilde{T} + \Big[\frac{\mathbf{t_s}}{\mathbf{Bo}} \Big] \tilde{T} \Big) \mathbf{n} dS = 0 \tag{3.2a}$$

$$\int_{\Omega} \boldsymbol{\omega_\nu} \Big(\frac{\partial \tilde{\mathbf{v}}}{\partial \tilde{t}} + \tilde{\mathbf{v}} \cdot \tilde{\boldsymbol{\nabla}}\tilde{\mathbf{v}} \Big) d\Omega - \int_{\Omega} \boldsymbol{\omega_\nu} \Big[\frac{\mathbf{RaPr}}{\mathbf{Pe^2}} \Big] (\tilde{T} - \tilde{T}_s) d\Omega$$

$$- \int_{\Omega} \tilde{\boldsymbol{\nabla}}.\boldsymbol{\omega_\nu}\tilde{P} d\Omega + \int_{\Omega} \boldsymbol{\omega_\nu} \Big[\frac{\mathbf{Pr}}{\mathbf{DaPe}} \Big] \tilde{\mathbf{v}} d\Omega + \int_{\Omega} \Big[\frac{\mathbf{Pr}}{\mathbf{Pe}} \Big] (\tilde{\boldsymbol{\nabla}}\boldsymbol{\omega_\nu}.\tilde{\nabla}\tilde{\mathbf{v}}) d\Omega$$

$$+ \int_{\partial \Omega_N^{\nu}} \boldsymbol{\omega_\nu} \Big(\tilde{P} - \Big[\frac{\mathbf{MaPr}}{\mathbf{Pe^2}} \Big] \tilde{\nabla}\tilde{T} \Big) \mathbf{n} dS = 0 \tag{3.2b}$$

here, $\mathbf{n}$ is the unit outward normal vector at the surface boundary. $\partial\Omega_N^T$ and $\partial\Omega_N^{\nu}$ are the boundaries for the temperature and velocity Neumann boundary conditions, respectively, and $\partial\Omega_D^T$ and $\partial\Omega_D^{\nu}$ are the boundaries for the temperature and velocity Dirichlet boundary conditions, respectively. ω_T and $\boldsymbol{\omega_\nu}$ are standard variations from the space $H^1(\Omega)$ - the Sobolev space of functions that are square-integrable and have a square-integrable derivatives. In these equations, the relevant dimensionless numbers are grouped inside square brackets. These dimensionless numbers, along with their physical interpretation, are listed in Table 3.2. The surface boundary condition in Equation 3.2a represents the nondimensional form of the convective and radiation heat losses to the inert surrounding, and the boundary condition (on the top surface) in Equation 4.2a represents

the Marangoni flow induced by the surface tension gradient.

Parameter	Expression	Physical interpretation
$\tilde{l}$	$\frac{l_p}{l_p}$	Dimensionless powder layer thickness
$\tilde{r}$	$\frac{r_s}{l}$	Dimensionless laser spot radius
$\tilde{t}$	$\frac{t\nu}{l_p}$	Dimensionless time
$\tilde{T}$	$\frac{T-T_\infty}{T_l-T_\infty}$	Dimensionless temperature
$\tilde{\mathbf{v}}$	$\frac{\mathbf{v}}{\mathbf{v}_p}$	Dimensionless velocity
$\tilde{p}$	$\frac{p}{\rho v_p^2}$	Dimensionless pressure
$\tilde{\nabla}$	$\frac{1}{l_p}\nabla$	Dimensionless gradient operator

Table 3.1: List of the scaling variables used in the non-dimensionalization of Equations 3.2a-4.2a

3.1.3 Computational implementation

As stated earlier, the above integral form of the governing equations are solved using FEM, and as model inputs, realistic process parameters and material properties of common LPBF alloys are chosen, and these are discussed in the Section 3.3.1 and in the Supplementary Information. FEM implementation is done in an in-house, scalable, finite element code framework written in C++ language with support for adaptive meshing and various implicit and explicit time-stepping schemes, and is built on top of the deal.II open source Finite Element library Arndt et al. (2021). Standard FEM constructs are adopted, and for all the simulations presented in this work, linear and quadratic Lagrange bases are used for pressure and other field variables such as temperature and velocity, respectively. The coupled Navier-Stokes equations are solved using Chorin's projection method (Chorin, 1997). Following the standard practice in our group to release all research codes as open source (Bhagat and Rudraraju, 2022;

Parameter	Expression	Physical interpretation
Prandtl ($\mathbf{Pr}$)	$\frac{\nu}{\alpha}$	Ratio of momentum to thermal diffusivity
Grashof ($\mathbf{Gr}$)	$\frac{g l^3 \beta (T_l - T_\infty)}{\nu^2}$	Ratio of buoyancy force to viscous force
Darcy ($\mathbf{Da}$)	$\frac{\kappa}{d_\phi^2}$	Ratio of permeability to the cross-sectional area
Marangoni ($\mathbf{Ma}$)	$\frac{d\gamma}{dT} \frac{l_p \Delta T}{\mu \alpha}$	Ratio of advection (surface tension) to diffusive transport
Péclet($\mathbf{Pe}$)	$\frac{l_p \nu_p}{\alpha}$	Ratio of advection transport to diffusive transport
Stefan ($\mathbf{Ste}$)	$\frac{c(T_l - T_s)}{L}$	Ratio of sensible heat to latent heat
Power ($\mathbf{Q}$)	$\frac{P}{\rho c (T_l - T_\infty) \nu_p l_p^2}$	Dimensionless power with velocity dependence
Radiation measure ($\frac{\mathbf{t_s}}{\mathbf{Bo}}$)	$\frac{\sigma (T_l - T_\infty)^3}{\rho c \nu_p}$	Measure of radiation contribution to the heat transfer
Biot ($\mathbf{Bi}$)	$\frac{h l_p}{k}$	Ratio of resistance to diffusion and convection heat transport

Table 3.2: Symbols, expressions and their physical interpretation for the dimensionless quantities considered in Equations 3.2a-4.2a

Gulati and Rudraraju, 2022; Wang et al., 2016; Jiang et al., 2016; Rudraraju et al., 2019), the complete code base for this work is made available to the wider research community as an open-source library (Bhagat, 2022a). A representative schematic of the computational domain and the relevant boundary conditions are shown in Figure 3.2. The important boundary conditions such as convective and radiations losses and shear stress on the top surface expressed as surface tension gradient with temperature is visible in the surface integral terms in Equation 3.2a-4.2a. The initial temperature and temperature at the bottom surface of the material are assumed to be fixed at 353K. The ambient temperature was taken as 301.15K. These temperatures were scaled to a dimensionless form in the computational implementation. The minimum and maximum dimensionless mesh sizes in an adaptive meshing scheme are taken to be $\Delta x = 0.8$ and $\Delta x = 6.0$ along the x, y, and z directions. A uniform dimensionless time step size of $\Delta t = 1.0$ is used for running test cases. The small factor in Equations 4.1b, $\delta = 1.0 \times 10^{-5}$ is used in all the simulations. The interface parameter (λ) used in our simulation is in the range $\lambda = [0.1, 1.0]$.

3.2 Experimental and numerical validation

In this section, a validation of the numerical formulation and the FEM-based computational framework is presented. This computational framework solves the thermo-fluidic governing equations of the meltpool described in Section 3.1. Further, a comparison is given between the simulation results with experimentally observed cooling rates (made available to us by our experimental collaborators), and with predictions of other numerical models from the literature. Variables like the cooling rates during the solidification, material temperature, velocity of fluid inside the pool, and meltpool geometry can be used as a yardstick to gauge the capability of our numerical model towards simulating the LPBF process. For this

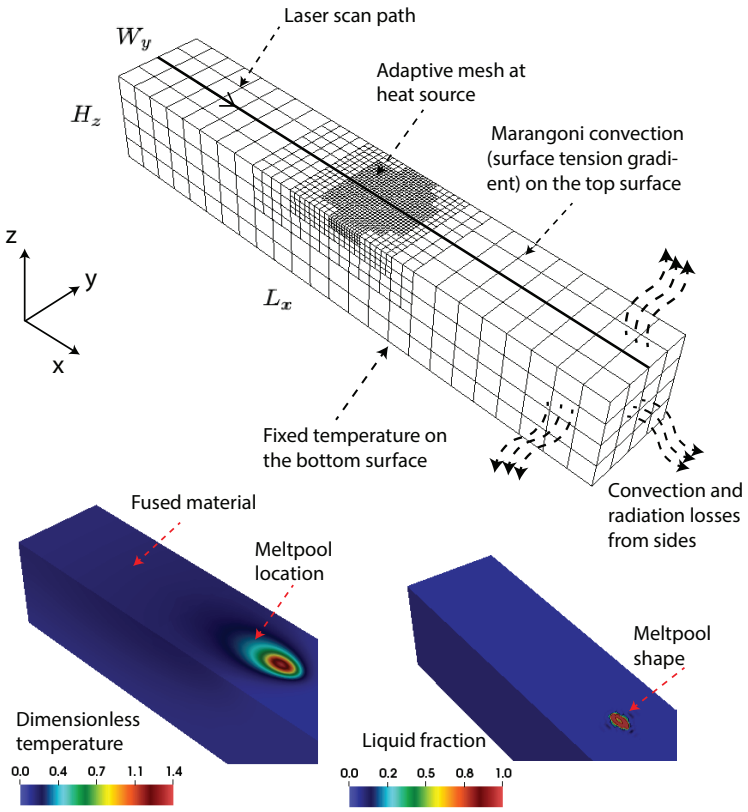

Figure 3.2: Schematic of the 3D finite element (FE) computational domain indicating the laser scan path and the relevant boundary conditions. Also shown is the underlying adaptive mesh that evolves with the location of the heat source. Representative dimensionless temperature profile and location of the meltpool obtained from the FE simulation of SS316 alloy AM are shown. The numerical parameters and material properties used in this simulation are given in Section 3.1.3 and in the Supplementary Information.

validation study, the temperature and velocity distributions, the cooling rates, and the maximum velocity in the meltpool are obtained from our FEM implementation. The cooling rate estimates from our simulations are compared with the cooling rates estimated from experimental data of the LPBF process that were obtained from Bertsch et al. (2020). Further, our

simulation results are compared with the corresponding material temperature distribution and meltpool velocity values obtained from numerical modeling data in (Shen et al., 2020). Simple thin-walled pseudo-2D plates and 3D cuboidal geometries made of stainless steel (SS316 alloy) using the LPBF process are considered in this validation study. The printed geometries consists of 13 x 0.2 x 13 mm^3 thin wall plates and 50 x 10 x 4 mm^3 cuboids. The schematic of the printed 2D plates and 3D cuboidal geometries can be found in Bertsch et al. (2020). These geometries are subsequently referred to as the 2D walls and 3D cuboids. The powder layer thickness used was 0.02 mm in both cases. Experimental details, AM technical specifications, and the post-processing methods used to measure cooling rates can be found in the publications of our experimental collaborators, Bertsch et al. (2020)-Rankouhi et al. (2020). The experimental cooling rates were estimated by our collaborators, through post-processing of the microstructure morphology, particularly the secondary dendrite arm spacing (λ_2) at a distance of 6.5 mm and 2 mm from the base for the 2D walls and 3D cuboids, respectively. The dendritic arm spacing in the printed parts was analyzed by our collaborators using a scanning electron microscope (SEM) following standard post-processing techniques. The cooling rates for the alloy SS316 were obtained using the relation $\lambda_2 = 25\dot{\epsilon}^{-0.28}$ (Thoma et al., 1995), where λ_2 is measured from SEM images.

For obtaining the numerical results, temperature-dependent material properties of the SS316 stainless steel alloy are considered separately for the powdered, fused, and liquid state of the material. The temperature and velocity distributions inside the meltpool were obtained from the FE model. The cooling rates are given by the expression $|\boldsymbol{\nabla} T|\boldsymbol{\nu}_p$, where $|\boldsymbol{\nabla} T|_2$ is a measure of the average temperature gradient in the meltpool, and $\boldsymbol{\nu}_p$ is the laser scanning speed. For the 2D plates, the cooling rate was measured at a location 6.5 mm from the base, both in the experiments and the FE model. Similarly, for the 3D cuboids, cooling rate estimates were

obtained at a location 2 mm from the base, both in the experiments and the FE model. As can be seen from Figure 3.3, the cooling rates obtained from the FE model are close to the experimentally reported values. The cooling rates are used for comparison with experiments in this work, as they are of immense practical interest due to their influence over the evolution of the microstructure (dendritic growth and grain growth) that then dictates the mechanical properties of the printed part.

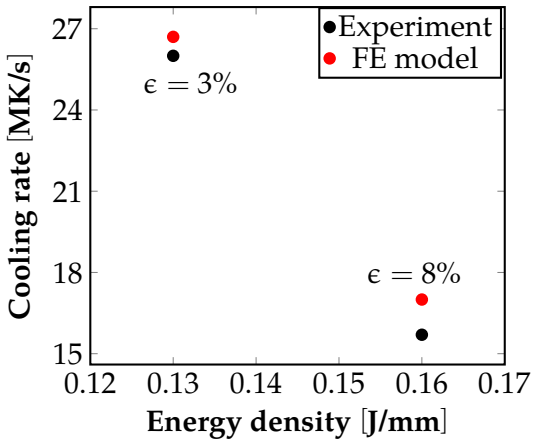

Figure 3.3: Dependence of cooling rates obtained from experiments and the FE model on the energy density, $\frac{P}{\boldsymbol{\nu}_p}$. The average cooling rate from the FE model was estimated using the relation: $\dot{T} = G\boldsymbol{\nu}_p = |\boldsymbol{\nabla} T|\boldsymbol{\nu}_p$. Laser power (W) and scan speed (mm/s) combinations used for this study were $(P, \boldsymbol{\nu}_p) = (90, 575), (90, 675)$.

Further, the temperature distribution and maximum velocity values in the meltpool obtained from the FE model were compared against the reference test cases given in (Shen et al., 2020). These cases represent the simulation of an LPBF process with a laser power of 100W and 200W used to print AZ91D magnesium alloy parts. As shown in the Figures 3.4a-3.4c, the point temperature as a function of time and the maximum meltpool velocity values obtained from our numerical model closely matches the trend reported in the literature. These comparisons provide a good val-

idation of our FE-based numerical formulation and its computational implementation.

3.3 Empirical analysis of the energy absorbed by the meltpool

In this section, the rationale behind the construction of a model of the energy absorbed by the meltpool is discussed. Numerical modeling of the AM process, in general, solves governing equations of heat conduction, fluid flow, mechanical deformation of the solidified region, etc., that is in terms of "local" field quantities like temperature, velocity, displacement, etc. However, the goal in this work is to arrive at estimates of the "global" response of the system at the meltpool-scale, i.e., measures like the meltpool morphology (size and shape), average temperature distribution, average velocity distribution, etc. *The intention is to propose and validate a "global" model of the energy absorbed by the meltpool in terms of various process variables, material properties, and output variables, and thus determine the important quantities, from amongst these dependencies, that have a most direct impact on the meltpool evolution*.

Towards proposing a linear model of the heat energy absorbed by the meltpool, various non-dimensional quantities are chosen that appear in Equations 3.2a and 4.2a. These are the input quantities made up of material properties, processing conditions, and surrounding environment variables. The general procedure used to estimate a linear model is as follows: $\hat{\mathbf{u}}$, the dimensionless measure of the heat absorbed by the meltpool, and modeled as linearly dependent on the input non-dimensional quantities. Such a model can be mathematically expressed as $\hat{\mathbf{u}} = \sum_{i=0}^{n} a_i \pi_i$. where n, π_i, and a_i denote the number of inputs, the dimensionless numbers considered and their corresponding coefficients, respectively. The merits and demerits of choosing various input non-dimensional quantities to

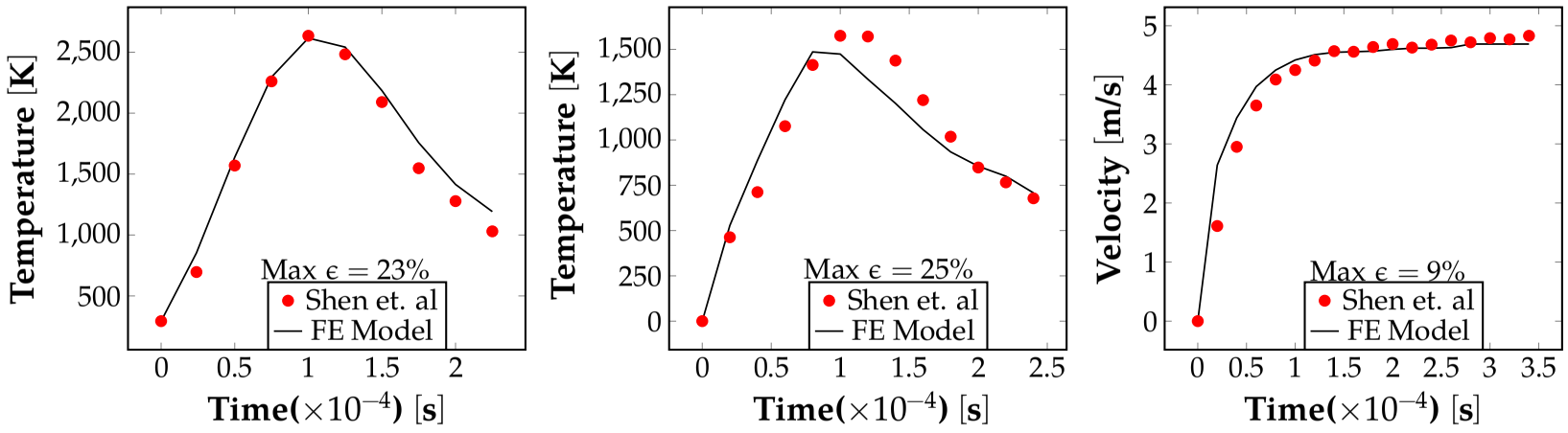

(a) (b) (c)

Figure 3.4: Validation of the FE model results by comparing with corresponding values reported in the literature. (3.4a) Variation of point temperature with time for the case P=200W. (3.4b) Variation of point temperature with time for the case P=100W. (3.4c) Variation of maximum pool velocity with time for the case P=100W.

characterize the model are evaluated using physics-based and statistical arguments discussed in the subsequent sections. Broadly, a method of least squares numerical approach is implemented to estimate the coefficients, a_i, corresponding to each dimensionless number, π_i, considered as a potential variable influencing the heat absorbed by the meltpool. It is the relative magnitude of these coefficients that inform us about the significance or insignificance of each dimensionless quantity towards the model of the heat absorbed. Further, it is understood from prior knowledge that a system with higher $\hat{\mathbf{u}}$ can potentially correlate to a rise in some measure of the meltpool temperature. The maximum temperature of the material is arguably higher if the heat received $\hat{\mathbf{u}}$ is higher. Thus, as a first-order argument, there exists a phenomenological relation $\hat{\mathbf{u}} \propto \tilde{T}_{max}$. This reasoning permits us to use $\tilde{T}_{max}$ as a measure of the $\hat{\mathbf{u}}$, and the value of $\tilde{T}_{max}$ is obtained by solving thermo-fluidic model described by Equations 3.2a-4.2a on different alloy materials and processing conditions listed in the Tables 3.6- 3.7 provided in the Supplementary Information. Having obtained $\tilde{T}_{max}$, the coefficients, a_i are estimated, using a method of least squares approach and an explicit form $\hat{\mathbf{u}}$ in terms of various dimensionless numbers, π_i is obtained. Once the linear model of the heat absorbed by the meltpool, $\hat{\mathbf{u}}$, is determined, it is linked with the several output variables of interest, namely the temperature gradient in the meltpool, the solidification cooling rate $(G\mathbf{v}_p)$, a measure of the advection heat transport due to the surface tension gradient, and finally the meltpool morphology (aspect ratio$(\frac{l_m}{w_m})$ and volume $(l_m w_m d_m)$). Important correlations between the relevant output variables and nondimensional input numbers are discussed at length in Section 3.4.

3.3.1 Process variables, material properties, and output variables

In this section, the process variables like laser characteristics, the material properties of the alloy, and the output variables obtained from the thermo-fluidic model are discussed. The powder layer thickness $l_p = 0.02$ mm and laser spot radius $r_p = 0.1$ mm are taken for all the cases. The simulation domain geometry, $L_x \times W_y \times H_z = 3 \times 0.5 \times 0.5$ mm^3, is fixed for all the cases. The movement of the laser is modeled as a single scan on the centerline of the top surface. The temporal and 3D spatial variations of the temperature and velocity of the material in the meltpool are obtained from the FE model. Due to the laser heat source, the temperature of the material increases past the liquidus melting temperature and results in the formation of a liquid meltpool. In the simulations, five commonly used LPBF alloy materials are considered, namely Stainless steel (SS316), a Titanium alloy (Ti-6Al-4V), a Nickel Alloy (Inconel 718), an Aluminium alloy (AlSi10Mg), and a Magnesium alloy (AZ91D)(Khairallah and Anderson, 2014; Mukherjee et al., 2018; Shen et al., 2020). To limit the complexity of the analysis by making dimensionless quantities independent of temperature, constant material properties (non-varying with temperature) are chosen. The numerical values of the input material properties for each of the alloys considered are provided in the Supplementary Information.

The process variables considered are the laser power value (P) and laser scan speed v_p, a laser distribution factor, $f = 2.0$, is fixed for all the cases. For a given alloy, twelve (4×3) combinations of the process variables were chosen to simulate a range of process conditions that are relevant to the LPBF process. The numerical values of the input process properties for each of the alloys considered are provided in the Supplementary Information, under Table 3.6 and Table 3.7 . In the thermo-fluidic model, the heat transfer coefficient (h) and the Stefan-Boltzmann constant (σ) are associated with the surrounding inert environment. $\sigma = 5.67 \times 10^{-8}$ $W/(m^2K^4)$

is a known constant. The effect of varying the heat transfer coefficient is found to have a negligible impact based on our preliminary simulations, so the heat transfer coefficient is taken as $h = 10\ W/m^2K$. This is due to the relatively minimal convective and radiation losses to the environment, as compared to the conduction of the heat through the base plate. In total, we perform about sixty $(5 \times 4 \times 3)$ LPBF simulations considering different process variables and material properties. At a fixed non-dimensional time $\tilde{t} = 100$, the maximum value of the magnitude of the temperature gradient $G = |\boldsymbol{\nabla} T|$ is recorded. The temperature gradient value in the meltpool region is significant but is relatively small outside this region. The temperature gradient is an important variable that controls the microstructure evolution in the additively printed material. The cooling rate, given by $G\boldsymbol{\nu}_p$, where $\boldsymbol{\nu}_p$ is the speed of the solid-liquid interface is also an important output variable for understanding the microstructure evolution. Further, the maximum temperature, T_{max}, and maximum velocity, $\boldsymbol{\nu}_{max}$, in the meltpool, is tracked along with a measure of the maximum extent of the meltpool length (l_m), width (w_m) and depth (d_m) that characterize the meltpool morphology.

3.3.2 Parametrization in terms of the dimensionless quantities

The use of an empirical approach to estimate $\hat{\mathbf{u}}$ is described in this section. The most appropriate set of dimensionless input parameters that explain variation in the measure of the heat absorbed is chosen. As stated earlier, $\hat{\mathbf{u}}$ is considered proportional to $\tilde{T}_{max}$. Sixty correlations of the form $(\Pi, \tilde{T}_{max})$ are generated from our simulations, where Π represents the set of the dimensionless input quantities considered. The unknown coefficients, (a_i) are determined through the standard method of linear least-squares regression. The data for the regression analysis is obtained from the finite element simulations of the LPBF process. Here multiple

regression attempts were made to arrive at a linear characterization of $\hat{\mathbf{U}}$ in terms of the most relevant dimensionless input quantities. While many combinations of the dimensionless input quantities were considered, three such attempts as representative of our regression analysis are presented here. The first two attempts result in correlations that are weak and hence discarded, before converging onto an acceptable correlation between $\hat{\mathbf{U}}$ and the relevant dimensionless input quantities in the third attempt.

First attempt of the regression analysis: The following set of independent variables: $\Pi = \{\frac{\mathbf{1}}{\mathbf{Pe}}, \mathbf{Q}, \frac{\mathbf{Tc}}{\mathbf{Ste}}, \frac{\mathbf{Bi}}{\mathbf{Pe}}, \frac{\mathbf{t_s}}{\mathbf{Bo}}\}$ are considered. The hypothesized linear relationship is shown below. Here ϵ is the error - the difference between the expected and true value of $\hat{\mathbf{U}}$.

$$\hat{\mathbf{U}} = a_0 + a_1\mathbf{Q} + a_2\mathbf{Pe}^{-1} + a_3\frac{\mathbf{Tc}}{\mathbf{Ste}} + a_4\frac{\mathbf{Bi}}{\mathbf{Pe}} + a_4\frac{\mathbf{ts}}{\mathbf{Bo}} + \epsilon \tag{3.3a}$$

The values of the coefficients resulting from the least-squares regression are given in Table 3.3. The condition number for this analysis is 8.11×10^7, which is very high. This indicates that there exists strong collinearity in the assumed input set Π. The collinearity can be understood in terms of the primary variable as follows: On close inspection of the dimensionless expressions for $\mathbf{Q} = \frac{P}{\rho c(T_l - T_\infty)\nu_p l_p^2}$, $\frac{\mathbf{1}}{\mathbf{Pe}} = \frac{\alpha}{\nu_p l_p}$, $\frac{\mathbf{Bi}}{\mathbf{Pe}} = \frac{hl\alpha}{\nu_p l_p}$, and $\frac{\mathbf{t_s}}{\mathbf{Bo}} = \frac{\sigma(T_l - T_\infty)^3}{\rho c \nu_p}$, it is observed that laser scan velocity is accounted for in all the four variables, and this can potentially reduce the linear independence of these physical quantities. Further, the role of inert environment variables is limited in our analysis. Considering the regression coefficients, $\mathbf{Bi}/\mathbf{Pe}$ and $\mathbf{t_s}/\mathbf{Bo}$ are dropped from our next regression attempt.

Second attempt of the regression analysis: In the second iteration, the chosen independent set is $\Pi = \{\mathbf{E}, \mathbf{Pe}, \frac{\mathbf{Tc}}{\mathbf{Ste}}\}$. The hypothesized linear

Parameter	Intercept	$\mathbf{Q}$	$\mathbf{Pe^{-1}}$	$\frac{\mathbf{Tc}}{\mathbf{Ste}}$	$\frac{\mathbf{Bi}}{\mathbf{Pe}}$	$\frac{\mathbf{t_s}}{\mathbf{Bo}}$
a_i	1.45^*	0.0053^*	-0.1719^*	-0.7076^*	300.3	-18200^*

Table 3.3: First attempt of the regression analysis to estimate the coefficients, a_i, using the linear least-squares approach. Asterisk(*) indicates the statistical significance of the coefficient using a t-test with a 95% confidence interval. Other statistics : $R^2 = 0.65$, Adjusted $R^2 = 0.61$, F-statistic=20.12, P(F)=0.0. Condition number=8.11×10^7.

Parameter	Intercept	$\mathbf{E}$	$\mathbf{Pe}$	$\frac{\mathbf{Tc}}{\mathbf{Ste}}$
a_i	0.6938^*	0.0087^*	-0.1677^*	0.1521

Table 3.4: Second attempt of the regression analysis to estimate the coefficients, a_i, using the linear least-squares approach. Asterisk(*) indicates the statistical significance of the coefficient using a t-test with a 95% confidence interval. Other statistics: $R^2 = 0.763$, Adjusted $R^2 = 0.750$, F-statistic=55.95, P(F)=0.0. Condition number=1.12×10^3.

Parameter	Intercept	$\mathbf{E}$	$\mathbf{Pe}$
a_i	0.8146^*	0.0082^*	-0.1654^*

Table 3.5: Third attempt of the regression analysis to estimate the coefficients, a_i, using the linear least-squares approach. Asterisk(*) indicates the statistical significance of the coefficient using a t-test with a 95% confidence interval. Other statistics : $R^2 = 0.746$, Adjusted $R^2 = 0.737$, F-statistic=83.61, P(F)=0.0. Condition number=422.

relationship is given by the following relation.

$$\hat{\mathbf{U}} = a_0 + a_1\mathbf{E} + a_2\mathbf{Pe} + a_3\frac{\mathbf{Tc}}{\mathbf{Ste}} + \epsilon \tag{3.3b}$$

Further, considering the details of the regression analysis, the expression for the variable dimensionless power, $\mathbf{Q}$, that had a velocity dependence is modified to a new variable, $\mathbf{E} = \frac{P}{k(T_l - T_\infty)} = \mathbf{PeQ}$. This new variable is a modified dimensionless power and is independent of the laser scan

velocity. Now, the laser scan speed parameter is only represented in the Péclet number, $\mathbf{Pe}$. The fourth term $\frac{Tc}{Ste}$ is purely dependent on the material properties. Note the least-squares solution yields the coefficients given in Table 3.4.

The least-square solution obtained from this model is an improvement over the previous model. This can be realized from the improvement in the accuracy of the fit given by the variable R^2. The adjusted R^2 improves from 0.65 to 0.75 with the less number of variables in the set Π. The condition number is still high but better than the previous model. Thus, the non-significant variable is dropped from the set, Π, in our third attempt.

Third attempt of the regression analysis: $\Pi = \{E, \mathbf{Pe}\}$ and the hypothesized linear relationship is given by the following relation.

$$\hat{U} = a_0 + a_1 E + a_2 \mathbf{Pe} + \epsilon \tag{3.3c}$$

The least-square solution is summarized in Table 3.5. The condition number is greatly improved. The probability that all $a_i = 0$ at the same time is negligible as seen from the probability of F-statistic. All the coefficients are statistically significant i.e the hypothesis that individual $a_i = 0$ can be safely discarded.

Now the linear model given by Equation 3.3c is interpreted in light of the physics of the additive process. The heat received by the material is defined by a quantity $\hat{U}$. The higher the heat received greater the temperature reached by the system. This $\hat{U}$ is related to the various material property and process parameters. Using the non-dimensional analysis, several parameters were combined into a bunch of non-dimensional numbers. These numbers are associated with and are responsible for several physical phenomena. Using the linear model and the available data, the variation of $\hat{U}$ was explained using a linear combination of constant, E and $\mathbf{Pe}$. A more complete dependence can potentially be highly non-linear,

but this also can be analytically intractable.

3.4 Results

In the previous section, a linear least-squares regression approach was used to arrive at a relation for the dimensionless heat energy absorbed, $\hat{U}$. The regression analysis resulted in a relation for $\hat{U}$ in terms of the dimensionless power, E, and the Péclet number, (Pe). In the following sections (Sections 3.4.1-3.4.3), relation for $\hat{U}$ is used to investigate the advective transport occurring inside the meltpool for different alloys and then to characterize their meltpool morphology (aspect ratio and volume) using the Marangoni number and the Stefan number. In Section 3.4.4, $\hat{U}$ is used to characterize microstructure evolution using the temperature gradients and the cooling rates in the solidified region.

3.4.1 Influence of Péclet number on advection transport in the meltpool

In this section, the extent of advection transport observed in the meltpool in different alloys during the LBPF process is discussed. The goal is to analyze the macroscopic geometric features of the meltpool, such as its aspect ratio and volume. In trying to explain the variation of these macroscopic features, a measure of advection in the meltpool using the relevant dimensionless quantities are critically investigated. Figure 3.5 describes the variation of the Péclet number, $Pe^* = Pe v_{max}$, with the non-dimensional quantity $Ma\hat{U}$. It is to be noted that the Péclet number with an asterisk, $Pe^* = Pe v_{max} = \frac{l_p v_p}{\alpha} \frac{v_{max}}{v_p}$, is defined using the maximum velocity in the meltpool, and is a measure of the advective transport relative to the diffusion transport in the meltpool. A larger value of Pe^* denotes a larger circulation of heat inside the meltpool due to the

fluid motion. The dimensionless quantity $\mathbf{Ma^*} = \mathbf{Ma\hat{U}}$ is a measure of heat transport caused by the fluid flow induced due to the surface tension gradient. As seen from the Figure 3.5, for the alloy shown, $\mathbf{Pe^*}$ increase with the $\mathbf{Ma^*}$. This correlation implies the overall movement of fluid in the meltpool is greater if the advection transport due to surface tension force is greater. Each point in these plots represents a single simulation result for the relevant quantities plotted and is obtained from the FEM framework. Another key information conveyed in Figure 3.5 is that for some alloys like AlSi10Mg, advection due to surface tension forces is minimal, as can be seen from the numerical values of the total advection ($\mathbf{Pe^{\circ}_{max}}$) shown on the Y-axis. On the other hand, alloys like Ti6Al4V show a higher value of advection transport due to surface tension forces. These observations are important correlations between advection measure $\mathbf{Pe^*} = \mathbf{Pe}\nu_{max}$, Marangoni number, Péclet number, and the dimensionless power ($\mathbf{Ma\hat{U}} = a_0\mathbf{Ma} + a_1\mathbf{MaE} + a_2\mathbf{MaPe}$), and will be used below to make connections to the meltpool morphology.

3.4.2 Influence of Marangoni number on the meltpool aspect ratio

In this section, the geometric characteristics of the meltpool, particularly the aspect ratio is discussed. The meltpool aspect ratio is defined as the ratio of its maximum length to its maximum width ($\frac{l_m}{w_m}$). To understand aspect ratio in terms of the input process parameters, dimensionless quantity $\mathbf{Ma\hat{U}}$ is useful. For characterizing the meltpool shapes, correlations were found between $\mathbf{Ma\hat{U}} = a_0\mathbf{Ma} + a_1\mathbf{MaE} + a_2\mathbf{MaPe}$ and the aspect ratio of the meltpool for different alloys, and different process parameters. The rise in $\hat{\mathbf{U}}$ is an indication of enough heat received by the material to cause melting during the additive process. The aspect ratio of the meltpool is related to the fluid flow induced inside the meltpool. As shown in the previous section, in Figure 3.5, AlSi10Mg alloy has a low advection

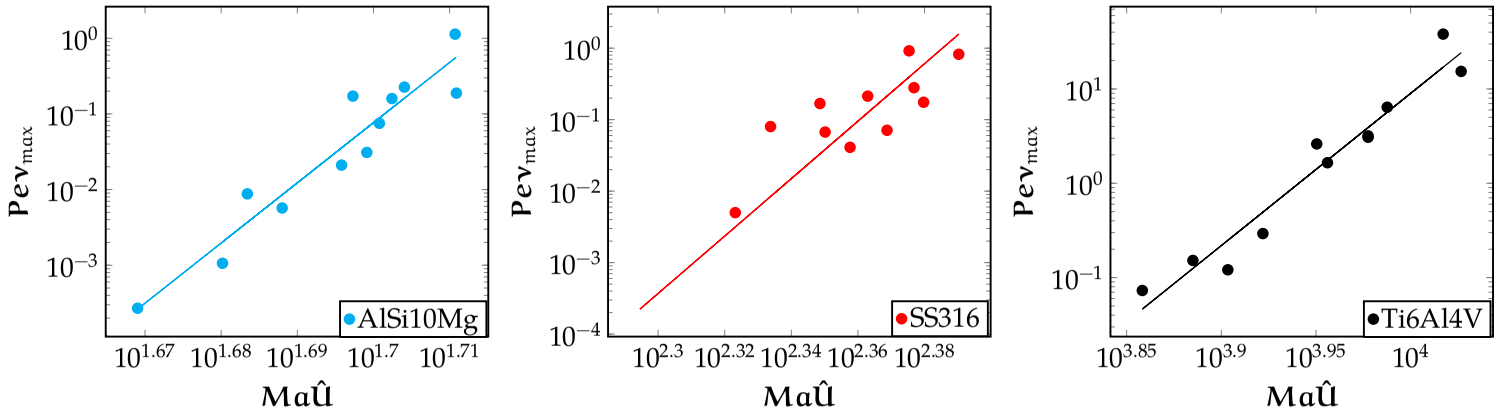

Figure 3.5: Measure of total advection measured as $\mathbf{Pe}^{\circ}_{\mathbf{max}}$ vs surface tension based advection $\mathbf{Ma\hat{U}} = a_0\mathbf{Ma} + a_1\mathbf{MaE} + a_2\mathbf{MaPe}$ on a log-log scale for (3.5a)AlSi10Mg, (3.5b)SS316, (3.5c)Ti6Al4V alloys. Corresponding plots comparing IN718 and AZ91D alloys, and a comparison of all the five alloys considered in this work can be found in Figure 3.10 and Figure 3.11 of the Supplementary Information. The advection measure corresponds to the degree of fluid flow inside the meltpool. Each point in these plots represent a single simulation result for the relevant quantities plotted, and is obtained from the FEM framework.

measure, $\mathbf{Pe\nu_{max}}$, and Ti6Al4V alloy has a high advection measure. This information is relevant here to understand the meltpool shapes of these materials. Figure 3.6a shows the variation of the aspect ratio ($\frac{l_m}{w_m}$) plotted as a function of non-dimensional quantity $\mathbf{Ma\hat{U}}$ for Ti6Al4V alloy material. The aspect ratio increases with $\mathbf{Ma\hat{U}}$. The aspect ratio with $\mathbf{Ma\hat{U}}$ if visualized in a combined plot for all the three alloys considered in this work, it is instructional to see the separations of materials into three clusters - each for one alloy, as seen in the Figure 3.6b. From this clustering, it can be seen that Ti6Al4V almost always produced an elongated or elliptical-shaped meltpool whose aspect ratio is far from 1. The alloy AlSi10Mg produces a meltpool that is relatively less elongated and has an aspect ratio closer to 1. The advection in the fluid flow causes the meltpool to expand along the direction of the higher temperature gradient. From this discussion, insightful observations, relating the aspect ratio of the meltpool with $\mathbf{Ma\hat{U}}$, can be made that help us characterize the meltpool shapes potentially produced by different alloys.

3.4.3 Influence of Stefan number on meltpool volume

In this section, a relation between the input non-dimensional numbers and the volume of the meltpool is presented. The volume of the meltpool is the volume of the localized region where the heat received by the material resulted in the melting of the material. the pool volume is identified using the liquid fraction, ϕ, which is a variable that we track in the model at all time instances and all spatial points in the domain. To completely melt the material, the material needs to absorb enough power to raise the temperature above the liquidus temperature and to overcome the latent heat barrier. The dimensionless power absorbed by the material is associated as a form of latent power, $P_L = \frac{\Omega_m}{l_p^3}\frac{\mathbf{Tc}}{\mathbf{Ste}}$. Since $\frac{\mathbf{Tc}}{\mathbf{Ste}}$ is constant for a given material, P_L is proportional to the volume of the material melted ($\tilde{\Omega}_m$). One can expect, as a first-order argument, that more material will melt if $\hat{\mathbf{U}}$ is higher. Thus,

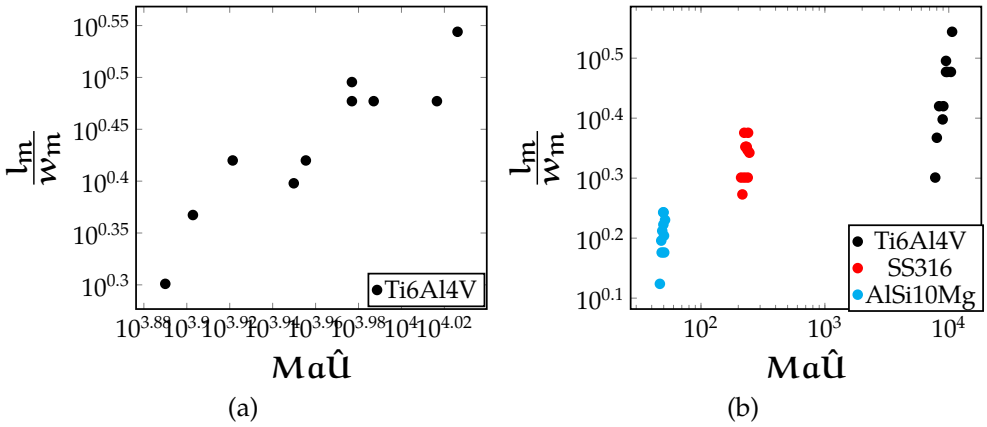

Figure 3.6: Correlation of the aspect ratio with $Ma\hat{U} = a_0 Ma + a_1 MaE + a_2 MaPe$, plotted on a log-log scale, for (3.6a) Ti6Al4V alloy, and for (3.6b) three alloys (Ti6Al4V, SS316 and AlSi10Mg) shown in a single plot to demonstrate clustering. A combined plot demonstrating this clustering for all the five alloys (Ti6Al4V, SS316, AlSi10Mg, IN718 and AZ91D) considered in this work can be found in Figure 3.12 of the Supplementary Information. Each point in these plots represent a single simulation result for the relevant quantities plotted, and is obtained from the FEM framework.

one can expect $P_L = \tilde{\Omega}_m \frac{Tc}{Ste}$ to increase with $\hat{U}$. This understanding helps us anticipate that the meltpool volume for different alloys, $\tilde{\Omega}_m$, increases with $\frac{Ste\hat{U}}{Tc}$, and this can indeed be seen in Figure 3.7a-3.7c. The numerical range of the meltpool volumes across the data points is similar, but for a given alloy, the meltpool volume increases with $\frac{Ste}{Tc}\hat{U}$. With this analysis, an important correlation is obtained between the meltpool volume and the quantity $\frac{Ste}{Tc}\hat{U} = a_0 \frac{Ste}{Tc} + a_1 \frac{SteE}{Tc} + a_2 \frac{StePe}{Tc}$.

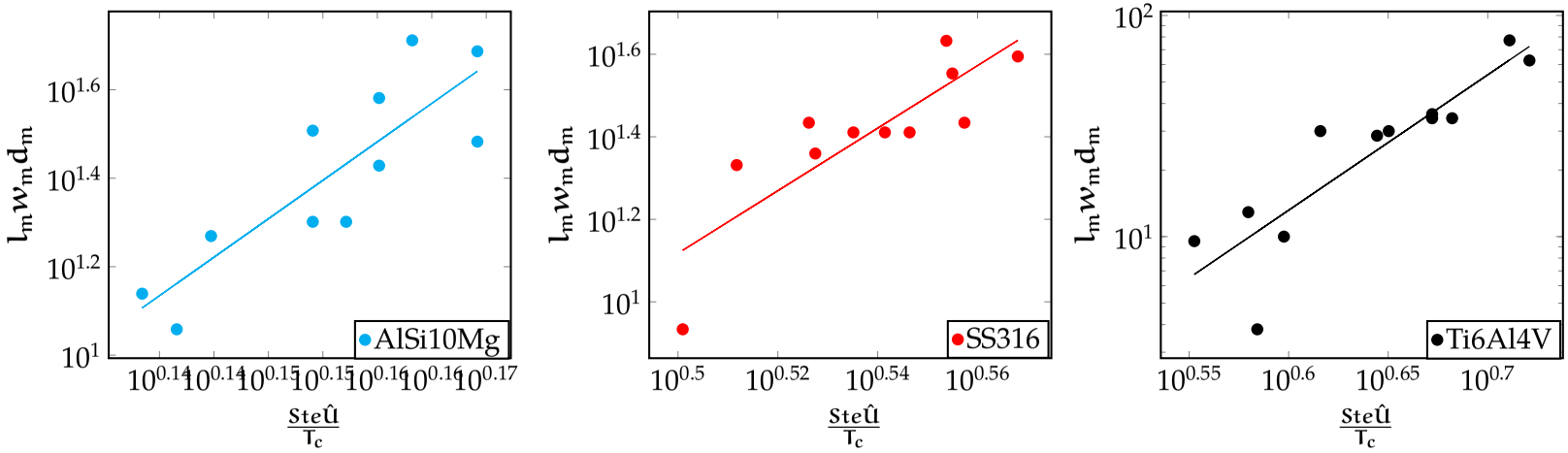

Figure 3.7: Correlation of the meltpool volume $(l_m w_m d_m)$ with $\frac{Ste\hat{u}}{T_c} = a_0\frac{Ste}{Tc} + a_1\frac{SteE}{Tc} + a_2\frac{StePe}{Tc}$, plotted on a log-log scale, for (3.7a) AlSi10Mg, (3.7b) SS316, and (3.7c) Ti6Al4V alloys. Corresponding plots comparing IN718 and AZ91D alloys, and a comparison of all the five alloys considered in this work can be found in Figure 3.13 and Figure 3.14 of the Supplementary Information. Each point in these plots represent a single simulation result for the relevant quantities plotted, and is obtained from the FEM framework.

3.4.4 Influence of the heat absorbed on the solidification cooling rates

In this section, a discussion on characterizing the microstructure of the solidified region is presented. To support this discussion, $\hat{\mathbf{U}}$ is used to explain the variation in the output variables like the temperature gradient, G, and the cooling rate, $G\boldsymbol{\nu}_p$, where $\boldsymbol{\nu}_p$ is the laser scan speed. These variables are traditionally understood to have a direct influence on the microstructure in the solidification literature. $\hat{\mathbf{U}} = a_0 + a_1\mathbf{E} + a_2\mathbf{Pe}$, has a strong linear correlation with the temperature gradient, G, as shown in the Figures 3.8a-3.8c. Considering the correlations observed in these figures, it can be inferred that the non-dimensional temperature gradient is proportional to the value of $\hat{\mathbf{U}}$. Further, this relation is expressed entirely in terms of input material properties and process parameters.

In the LPBF process, the laser scan speed controls the speed of movement of the solidification interface. The laser scan speed used in the simulations is assumed to be equal to the maximum solid-liquid interface velocity ($\boldsymbol{\nu} = \boldsymbol{\nu}_p$ (Mohammadpour et al., 2020; Rappaz et al., 1990). The variation of the cooling rates, $G\boldsymbol{\nu}_p$ are observed with $\hat{\mathbf{U}}$ by increasing dimensionless laser power, $\mathbf{E}$, but keeping the Péclet number fixed. The dimensionless temperature gradient, $\tilde{G}_{max}$, will increase with $\hat{\mathbf{U}}$. as seen in the Figure 3.8. It is also instructional to see that the cooling rate, $G\boldsymbol{\nu}_p$, increases with $\hat{\mathbf{U}}$, as shown in Figure 3.9a. There exists a well-known correlation between a microstructure size, λ_2, and the cooling rate, $G\boldsymbol{\nu}_p$, in the solidification process, and is given by the relation $\lambda_2 = 25(G\boldsymbol{\nu}_p)^{-0.28}$ (Thoma et al., 1995). Using this relation, it can be seen that the size of the microstructure will get finer as we increase $\hat{\mathbf{U}}$, which can be achieved by increasing $\mathbf{E}$. Thus, the size of the microstructure correlates with the input non-dimensional quantity given by $\hat{\mathbf{U}} = a_0 + a_1\mathbf{E} + a_2\mathbf{Pe}$.

The effect of $\hat{\mathbf{U}}$ on the cooling rate is studied due to a change in the Péclet number, $\mathbf{Pe}$, but keeping the dimensionless laser power, $\mathbf{E}$, fixed. $\hat{\mathbf{U}}$

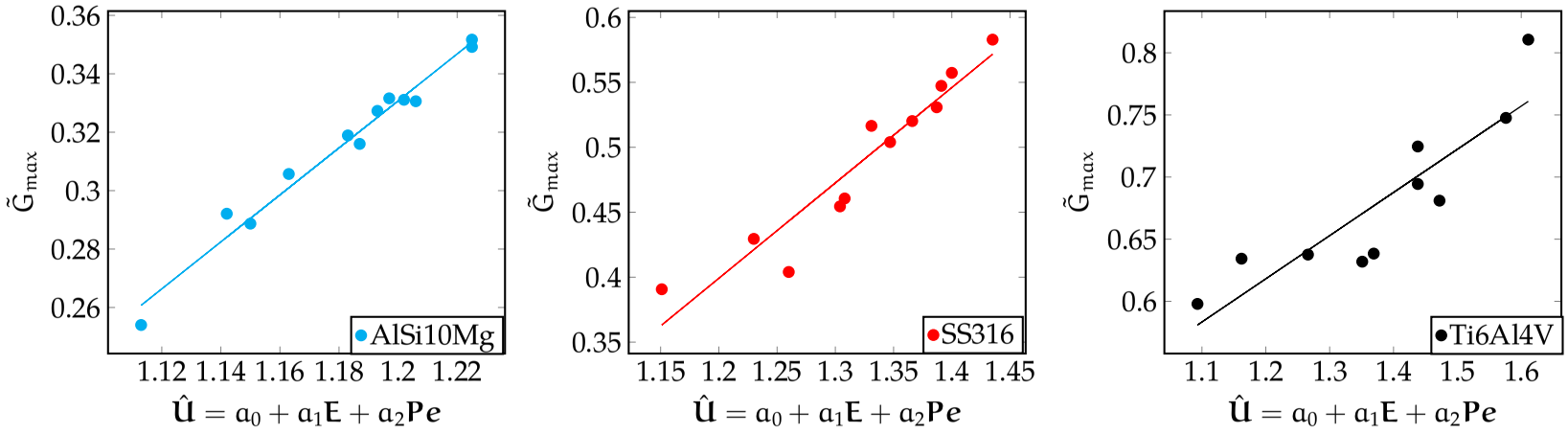

(a) b (b) b (c) b

Figure 3.8: Dimensionless temperature gradient (G) with the $\hat{U}$ for different alloys. Plots corresponding to IN718 and AZ91D alloy material can be found in Figure 3.15 of the Supplementary Information. Each point in these plots represent a single simulation result for the relevant quantities plotted, and is obtained from the FEM framework.

decreases with increase in $\mathbf{Pe}$ and $\mathbf{E}$ fixed. From Figure 3.8, it is known that the dimensionless temperature gradient, G, and its dimensional counterpart, both decrease if we decrease $\hat{\mathbf{U}}$. Thus the cooling rate, $G\boldsymbol{\nu}_p$, decreases with increase in $\hat{\mathbf{U}}$, as seen in Figure 3.9b. This decrease is solely due to an increase in the value of $\mathbf{Pe}$. Using this information, a correlation is identified between the change in the size of the microstructure and the Péclet number, i.e, increasingly coarser microstructural features can be observed with a decrease in the cooling rate.

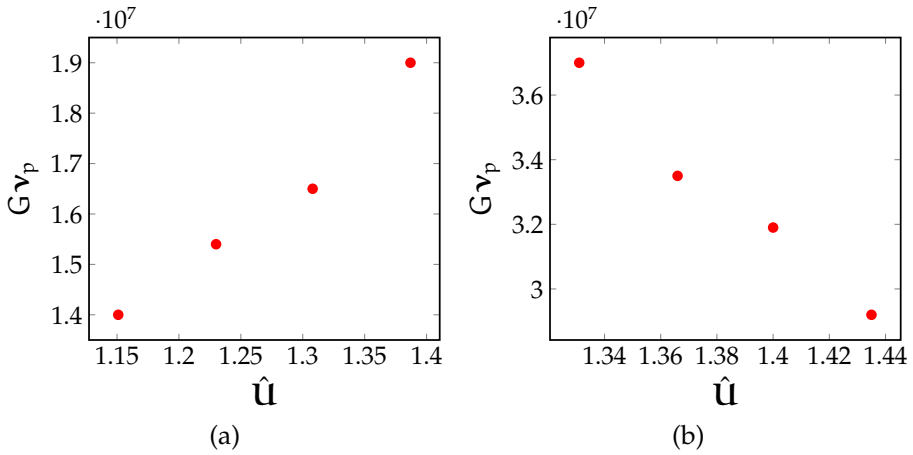

Figure 3.9: (3.9a) Variation of the dimensional cooling rate, $G\boldsymbol{\nu}_p$, with $\hat{\mathbf{U}} = a_0 + a_a\mathbf{E} + a_2\mathbf{Pe}$, plotted on a log-log scale. Here, $\hat{\mathbf{U}}$ is changed by changing $\mathbf{E}$, but keeping $\mathbf{Pe}$ fixed for SS316 alloy, (3.9b) Variation of dimensional cooling rate, $G\boldsymbol{\nu}_p$, with $\hat{\mathbf{U}} = a_0 + a_a\mathbf{E} + a_2\mathbf{Pe}$, plotted on a log-log scale. Here, $\hat{\mathbf{U}}$ is changed by changing $\mathbf{Pe}$, but keeping $\mathbf{E}$ fixed for SS316 alloy.

Supplementary Information for "Chapter 3"

Material properties and process variables

Material properties of various alloys and the corresponding AM process variables used in this work are listed here. These properties were collected from multiple sources in the literature. The properties of solid and liquid materials are averaged and dependence on the temperature is neglected.

Property	SS316	Ti6Al4V	IN718	AlSi10Mg	AZ91D
$\rho(\frac{kg}{m^3})$	7800	4000	8100	2670	1675
$c(\frac{J}{kgK})$	490	570	435	890	1122
$k(\frac{W}{mk})$	36.5	7.3	11.4	173.0	77 .5
$\mu(\frac{Kg}{ms})$	7.0×10^{-3}	4.0×10^{-3}	5.0×10^{-3}	1.3×10^{-3}	3.0×10^{-3}
$\frac{d\gamma}{dT}(\frac{N}{mK})$	-4.00×10^{-4}	-2.63×10^{-3}	-3.70×10^{-3}	-3.5×10^{-4}	-2.13×10^{-4}
$\beta(\frac{1}{K})$	5.85×10^{-5}	2.50×10^{-5}	4.8×10^{-5}	2.4×10^{-5}	9.54×10^{-5}
$\kappa(m^2)$	5.56×10^{-13}	5.56×10^{-13}	5.56×10^{-13}	5.56×10^{-13}	5.56×10^{-13}
$L(\frac{J}{kg})$	2.72×10^5	2.84×10^5	2.09×10^5	4.23×10^5	3.73×10^5
$T_s(K)$	1693	1878	1533	831	743
$T_l(K)$	1733	1928	1609	867	868

Table 3.6: Average material properties for different alloys used to calculate input non-dimensional numbers of the thermo-fluidic model Mukherjee et al. (2018), Shen et al. (2020)

Material	(Laser Power, Scan speed) (P, ν_p)
SS316	(70, 0.3), (80, 0.4), (90, 0.5), (100, 0.6) (110, 0.7), (110, 0.8), (110, 0.9), (110, 1.0) (65, 0.5), (75, 0.5), (85, 0.5), (95, 0.5)
Ti6Al4V	(15, 0.2), (25, 0.5), (35, 0.7), (45, 0.9) (40, 0.6), (40, 0.7), (40, 0.8), (40, 1.0) (35, 0.9), (40, 0.9), (45, 0.9), (50, 0.9)
IN718	(20, 0.15), (30, 0.25), (40, 0.45), (50, 0.75), (45, 0.80), (45, 0.90), (45, 1.0), (45, 1.1) (53, 0.95), (55, 0.95), (58, 0.95), (60, 0.95)
AlSi10Mg	(75, 0.35), (85, 0.45), (95, 0.55), (105, 0.65) (100, 0.6), (100, 0.7), (100, 0.8), (100, 0.9) (90, 1.1), (95, 1.1), (100, 1.1), (110, 1.1)
AZ91D	(35, 0.25), (40, 0.30), (45, 0.35), (50, 0.45 (40, 0.30), (40, 0.40), (40, 0.50), (40, 0.60) (40, 0.60), (50, 0.60), (60, 0.60), (70, 0.60)

Table 3.7: Chosen process conditions for different alloys used to calculate input non-dimensional numbers of the thermo-fluidic model

Additional correlations of the dimensionless numbers

The influence of the Péclet number on advection transport in the meltpool for additional materials IN718 and AZ91D is shown in Figure 3.10, and the corresponding comparison of the five alloys considered in this work is given in Figure 3.11. The combined plot of aspect ratio with $\mathbf{Ma\hat{U}}$ is given in the Figure 3.12. The meltpool aspect ratio and Marangoni number of IN718 and Ti6AL4V are similar magnitudes. Similarly, the meltpool aspect ratio and Marangoni number of AZ91D and AlSi10Mg are comparable. The influence of Stefan number on the meltpool volumes for IN718 and AZ91D is shown in Figure 3.13, and the corresponding comparison of the five alloys considered in this work is given in Figure 3.14. Influence of dimensionless heat absorbed on non-dimensional temperature gradient (G) for IN718 and AZ91D is shown in Figure 3.15.

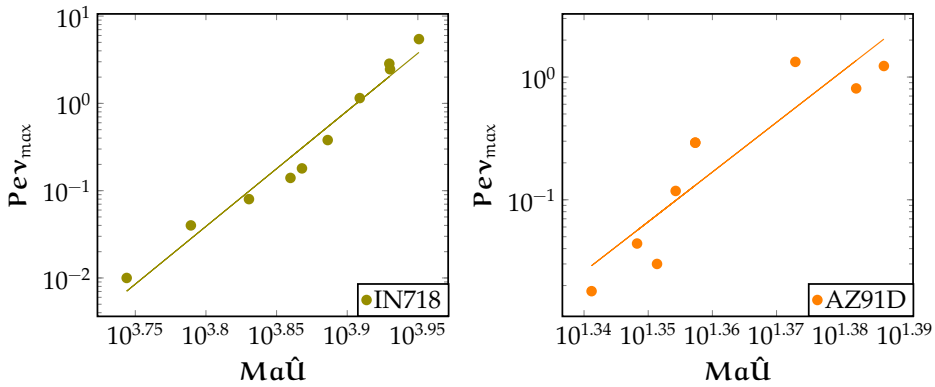

Figure 3.10: Measure of total advection measured as $\mathbf{Pe\nu}_{max}$ vs surface tension based advection $\mathbf{Ma\hat{U}} = a_0\mathbf{Ma} + a_1\mathbf{MaE} + a_2\mathbf{MaPe}$ on a log-log scale for (3.10a)IN718 (3.10b)AZ91D, alloys.

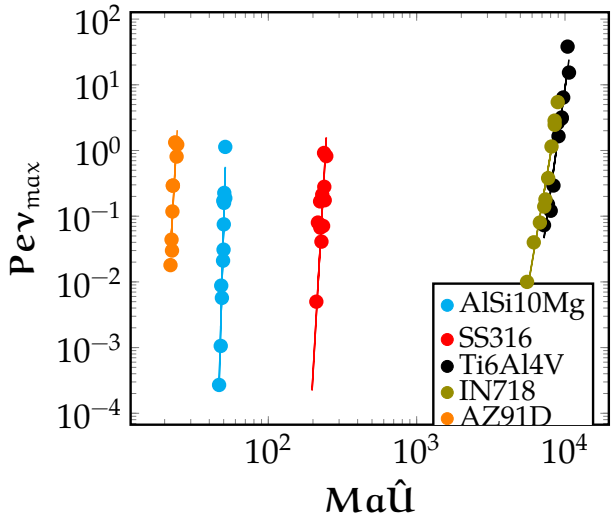

Figure 3.11: Measure of total advection measured as $Pe_{v_{max}}$ vs surface tension based advection $Ma_{\hat{U}} = a_0 Ma + a_1 MaE + a_2 MaPe$, plotted on a log-log scale, for all the five alloys (AlSi10Mg, SS316, Ti6Al4V, IN718 and AZ91D) considered in this work.

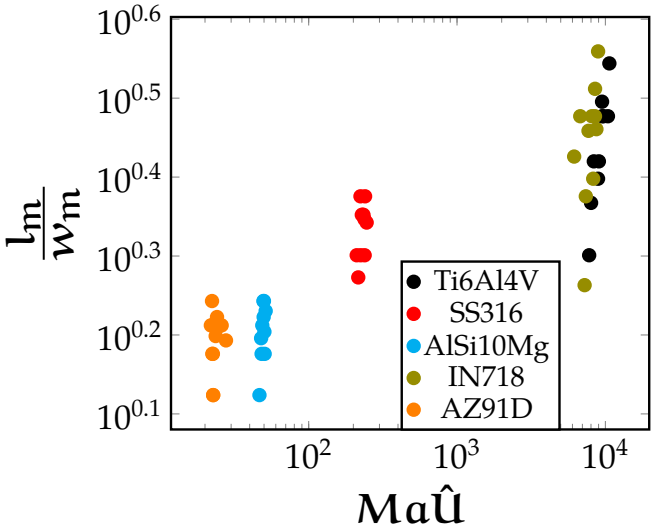

Figure 3.12: Correlation of the aspect ratio with $Ma_{\hat{U}} = a_0 Ma + a_1 MaE + a_2 MaPe$, plotted on a log-log scale, for all five alloys (Ti6Al4V, SS316, AlSi10Mg, IN718 and AZ91D) shown in a single plot to demonstrate clustering.

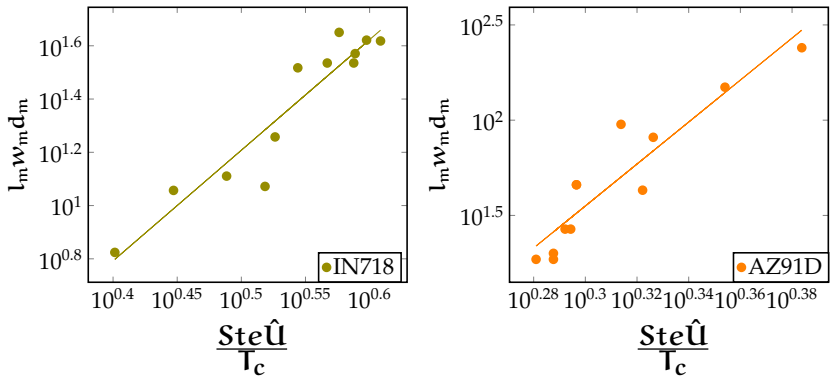

Figure 3.13: Correlation of the meltpool volume ($l_m w_m d_m$) with $\frac{Ste\hat{U}}{T_c} = a_0 \frac{Ste}{T_c} + a_1 \frac{SteE}{T_c} + a_2 \frac{StePe}{T_c}$, plotted on a log-log scale, for (3.13a) IN718, and (3.13b) AZ91D, alloys.

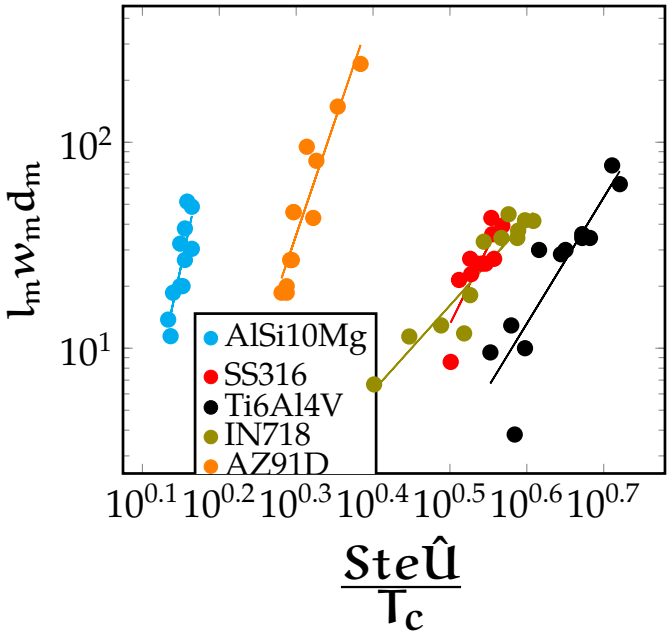

Figure 3.14: Correlation of the meltpool volume ($l_m w_m d_m$) with $\frac{Ste\hat{U}}{T_c} = a_0 \frac{Ste}{T_c} + a_1 \frac{SteE}{T_c} + a_2 \frac{StePe}{T_c}$, plotted on a log-log scale, for all the five alloys (AlSi10Mg, SS316, Ti6Al4V, IN718 and AZ91D) considered in this work.

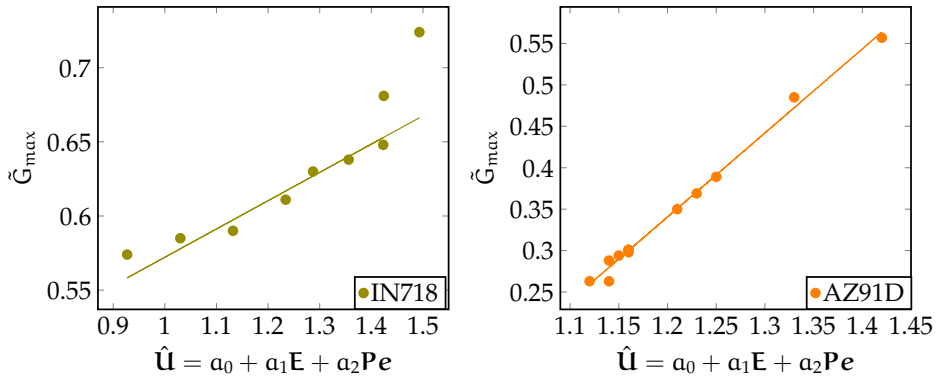

(a) b (b) b

Figure 3.15: Dimensionless temperature gradient (G) with the $\hat{U}$ for (3.15a) IN718 and (3.15b) AZ91D alloys.

4 MICROSTRUCTURE EVOLUTION UNDER THE INFLUENCE OF FLUID FLOW AND REMELTING

In this chapter, the effect of remelting and fluid flow on the microstructure evolution of metal additive manufacturing is investigated. Section 4.1 consists of governing equations for the coupled fluid flow and phase-field model. Section 4.2 covers the finite element implementation of the coupled fluid flow and phase-field model. The discussion on the effect of remelting on the solid-liquid interface and the effect of different fluid flow conditions on equiaxed and columnar dendrites is outlined in Section 4.3.

4.1 Governing equations

In this section, governing equations for dendritic solidification under the influence of fluid flow are described. The fluid flow is modeled with continuity and momentum conservation described in Section 4.1.1. These equations represent Navier-stokes equations for incompressible flow. The dendritic solidification is modeled with a diffuse interface phase-field based approach. Two forms of the phase-field model are presented, namely (a) phase-field model for solidification of pure melt described in Section 4.1.2, and (b) phase-field model for solidification of binary alloy described in Section 4.1.3.

4.1.1 Continuity and momentum conservation

Equation 4.1a- 4.1b are the mass and momentum conservation equation governing fluid flow in the melt of pure metal or binary alloy. It is assumed that the density of liquid and solidifying melt is uniform and temperature independent. The expressed equation is in the dimensionless form where $\boldsymbol{\nu} = \frac{\mathbf{u}\tau_0}{\lambda_0}$ is the velocity of fluid flow in the liquid and solidifying region.

Here τ_0 and λ_0 are the characteristics time scale and length scale obtained from the phase-field model.

$$\boldsymbol{\nabla}.\boldsymbol{\nu}(\boldsymbol{x},t) = 0, \quad \boldsymbol{x} \in \Omega \tag{4.1a}$$

Here Ω represents the domain consisting of the liquid melt and solidifying region. $\mathbf{p} = \frac{P\tau_0^2}{\rho\lambda_0}$ is dimensionless pressure and η is the kinematic viscosity.

$$\frac{\partial \boldsymbol{\nu}(\boldsymbol{x},t)}{\partial t} + \boldsymbol{\nu}(\boldsymbol{x},t).\boldsymbol{\nabla}\boldsymbol{\nu}(\boldsymbol{x},t) = -\boldsymbol{\nabla}\mathbf{p} + \boldsymbol{\nabla}.\big(\eta\boldsymbol{\nabla}\boldsymbol{\nu}(\boldsymbol{x},t)\big) \\ -\eta h(1+\phi)^2\boldsymbol{\nu}(\boldsymbol{x},t), \quad \boldsymbol{x} \in \Omega \tag{4.1b}$$

Equation 4.1b is coupled with phase-field model through order parameter ϕ. Here value of $\phi = 1$ represents the bulk solid region and $\phi = -1$ represents the bulk liquid region. The term $\eta h(1+\phi)^2\boldsymbol{\nu}(\boldsymbol{x},t)$ is the increased inertial pressure experienced by the fluid flow in the diffuse solidifying region. It can be interpreted as a momentum sink term which is zero in the liquid region and increases in magnitude along the diffuse region. In the solid region, and across the diffuse interface, the value of the inertial pressure increases, thereby forcing the velocity to drop several orders of magnitude than in the liquid region (Cimolin and Discacciati, 2013). The forcing function $(1+\phi)^2$ provides a smooth increase in inertial pressure and better convergence in the numerical implementation. Faster variation of inertial pressure across the diffuse interface can be modeled by choosing functions such as $(1+\phi)^4$ or $\frac{(1+\phi)^2}{(1-\phi)^3+\epsilon}$ where ϵ is a small constant (Brent et al., 1988).

4.1.2 Advective form of phase-field model of pure metal solidification

In this section, phase-field model for solidification of pure metal solidification coupled with the fluid flow model previously described in Section 4.1.1

is presented. Equation 4.1c is the thermal diffusion equation of phase-field model. This phase-field model is used to study the solidification of pure metal. Solidification of pure metal is described by the classical Stefan problem which is characterized by the parabolic heat diffusion equation and the consideration of a moving sharp solid-liquid interface. At the instantaneous interface location, the balance of heat flux has to be satisfied Slavov et al. (2003). This problem is re-framed as a diffuse interface problem using a Phase-field model (Plapp and Karma, 2000). The description of Stefan problem and its modification to the phase-field is covered earlier in Chapter 2.

$$\frac{\partial u_T}{\partial t} + \boldsymbol{\nu}.\nabla u_T = D\nabla^2 u_T + \frac{1}{2}\frac{\partial \phi}{\partial t}, \quad \boldsymbol{x} \in \Omega \tag{4.1c}$$

Here $u_T = \frac{(T-T_m)L}{c}$ is the dimensionless temperature. T and T_m are the temperatures and the melting temperature of pure metal. c is specific heat and L is volumetric latent heat enthalpy. ϕ is the order parameter denoting solid, liquid, or diffuse interface region. The term $\boldsymbol{\nu}.\nabla u_T$ denotes the advection of heat during the solidification of pure metal (Chen and Yang, 2019). The diffusion of heat is influenced by the direction of liquid melt velocity $\boldsymbol{\nu}$ and the direction of dimensionless temperature gradient $\boldsymbol{\nabla u_T}$.

$$\tau(\boldsymbol{n})\frac{\partial \phi}{\partial t} = -\frac{\partial f}{\partial \phi} + \boldsymbol{\nabla}\cdot\left(\lambda^2(\boldsymbol{n})\boldsymbol{\nabla}\phi\right) + \frac{\partial}{\partial \boldsymbol{x}}\left[|\boldsymbol{\nabla}\phi|^2\lambda(\boldsymbol{n})\frac{\partial\lambda(\boldsymbol{n})}{\partial\left(\frac{\partial\phi}{\partial \boldsymbol{x}}\right)}\right] + \frac{\partial}{\partial \boldsymbol{y}}\left[|\boldsymbol{\nabla}\phi|^2\lambda(\boldsymbol{n})\frac{\partial\lambda(\boldsymbol{n})}{\partial\left(\frac{\partial\phi}{\partial \boldsymbol{y}}\right)}\right], \boldsymbol{x} \in \Omega \tag{4.1d}$$

Equation 4.1d represents the diffusion of order parameter ϕ in the phase-field model. Here ϕ represents a continuous variation of phase such that $\phi = 1$ indicates a bulk solid region, $\phi = -1$ indicates a bulk liquid region and $1 < \phi < -1$ indicates diffuse interface region (Plapp and Karma, 2000).

The dendrites are assumed to be fixed or rooted in the melt so the advection of order parameter ϕ given by term $\boldsymbol{\nu} \cdot \boldsymbol{\nabla}\phi$ is neglected (Beckermann et al., 1999). $\lambda(\mathbf{n}) = \lambda_0 a_s$ is the anisotropic interface thickness. $\mathbf{n} = \frac{\boldsymbol{\nabla}\phi}{|\boldsymbol{\nabla}\phi|}$ is the unit normal to the interface and anisotropy parameter is given by $a_s = (1-3\epsilon_4)\Big[1 + \frac{4\epsilon_4}{(1-3\epsilon_4)} \frac{(\partial_x \phi)^4 + (\partial_y \phi)^4}{|\phi|^4}\Big] = 1 + \epsilon_4 cos(m\theta)$. The characteristics time scale $\tau = \tau_0 a_s^2$ is related to interface mobility. $\frac{\partial f}{\partial \phi} = -\phi + \phi^3 + \xi(1-\phi^2)^2\big(u_T\big)$ is derivative of double well potential.

4.1.3 Advective form of phase-field model of binary alloy

In this section, phase-field model for the solidification of binary alloy coupled with the fluid flow model earlier described in Section 4.1.1 is outlined. Equation 4.1e is the solute diffusion equation of phase-field model. This phase-field model is used to study the solidification of binary alloy (Echebarria et al., 2004). Analogous to Stefan problem of heat diffusion of pure melt, the solidification of a binary alloy is described by the Stefan problem of mass diffusion (Neumann-Heyme, 2017). The details of this Stefan problem and the phase-field model representation are covered in Chapter 2.

$$\Big(\frac{1+k}{2} - \frac{1-k}{2}\phi\Big)\frac{\partial u_c}{\partial t} + \boldsymbol{\nu}.\boldsymbol{\nabla} u_c = \boldsymbol{\nabla} \cdot \Big(\tilde{D}\big(\frac{1-\phi}{2}\big)\boldsymbol{\nabla} u_c - \mathbf{J}_{at}\Big) + \Big(1 + (1-k)u_c\Big)\frac{1}{2}\frac{\partial \phi}{\partial t}, \quad \boldsymbol{x} \in \Omega \tag{4.1e}$$

Here $u_c = \frac{1}{1-k}\big(\frac{2c}{c_l^0(1-\phi+k(1+\phi))} - 1\big)$ is defined as concentration undercooling. c, c_l^0, k, and ϕ are solute concentration, initial solute concentration in the liquid melt, partition coefficient, and order parameter. $\tilde{D}$ is dimensionless diffusivity in the liquid phase. $\mathbf{J}_{at}$ is anti-flux current (Echebarria et al., 2004)- Ohno and Matsuura (2009). The term $\boldsymbol{\nu} \cdot \boldsymbol{\nabla} u_c$ denotes the advection of dimensionless solute undercooling u_C during the solidification of a binary alloy. The diffusion of solute is influenced by the direction of liquid

melt velocity $\boldsymbol{v}$ and the direction of dimensionless solute undercooling gradient $\boldsymbol{\nabla} u_c$ (Rojas et al., 2015)-(Beckermann et al., 1999). Equation 4.1f represents the diffusion of order parameter ϕ in the phase-field model of a binary alloy. Similarly, the dendrites are assumed to be fixed or rooted in the melt so the advection of order parameter ϕ is neglected.

$$\Big(1-(1-k)\frac{y-\tilde{v}t}{\tilde{l}_T}\Big)a_s^2(\boldsymbol{n})\frac{\partial\phi}{\partial t}=-\frac{\partial f}{\partial\phi}+\boldsymbol{\nabla}\cdot\big(a_s^2(\boldsymbol{n})\boldsymbol{\nabla}\phi\big) \quad (4.1f)$$
$$+\frac{\partial}{\partial x}\Big(|\boldsymbol{\nabla}\phi|^2 a_s(\boldsymbol{n})\frac{\partial a_s(\boldsymbol{n})}{\partial\left(\frac{\partial\phi}{\partial x}\right)}\Big)+\frac{\partial}{\partial y}\Big(|\boldsymbol{\nabla}\phi|^2 a_s(\boldsymbol{n})\frac{\partial a_s(\boldsymbol{n})}{\partial\left(\frac{\partial\phi}{\partial y}\right)}\Big), \quad \boldsymbol{x}\in\Omega$$

Here $\frac{\partial f}{\partial\phi}=-\phi+\phi^3+\xi(1-\phi^2)^2\big(u_c+\frac{y-\tilde{v}t}{\tilde{l}_T}\big)$ is derivative of double well potential.

4.2 Numerical implementation

The weak or integral form of the governing equations as per standard Finite Element techniques are delineated in Section 4.2.1. The details on the coupled implementation of Navier-Stokes and phase-field method and computational specifics are covered in Section 4.2.2.

4.2.1 Integral form

Find the primal fields, $\{\boldsymbol{v}, u_{T/c}, \phi\}$. Here $u_{T/c}$ is u_T or u_c where,

$$\begin{aligned}
\boldsymbol{v}\in\mathscr{S}_{\boldsymbol{v}}, &\quad \mathscr{S}_{\boldsymbol{v}}=\{\boldsymbol{v}\in H^1(\Omega)\mid \boldsymbol{v}=\ \boldsymbol{v}'\ \forall\,\boldsymbol{x}\in\partial\Omega_D^{\boldsymbol{v}}\},\\
u_{T/c}\in\mathscr{S}_u, &\quad \mathscr{S}_u=\{u_{T/c}\in H^1(\Omega)\mid u_{T/c}=\ u'_{T/c}\ \forall\,\boldsymbol{x}\in\partial\Omega_D^{u}\},\\
\phi\in\mathscr{S}_\phi, &\quad \mathscr{S}_\phi=\{\phi\in H^1(\Omega)\mid \phi=\ \phi'\ \forall\,\boldsymbol{x}\in\partial\Omega_D^{\phi}\},
\end{aligned}$$

such that,

$$\begin{aligned}
\forall\, \boldsymbol{\omega}_{\boldsymbol{\nu}} \in \mathscr{V}_{\boldsymbol{\nu}}, \quad \mathscr{V}_{\boldsymbol{\nu}} &= \{\boldsymbol{\omega}_{\boldsymbol{\nu}} \in H^1(\Omega) \mid \boldsymbol{\omega}_{\boldsymbol{\nu}} = 0 \,\forall\, \mathbf{x} \in \partial\Omega_D^{\boldsymbol{\nu}}\},\\
\forall\, \omega_{u_{T/c}} \in \mathscr{V}_{u_{T/c}}, \quad \mathscr{V}_{u_{T/c}} &= \{\omega_{u_{T/c}} \in H^1(\Omega) \mid \omega_{u_{T/c}} = 0 \,\forall\, \mathbf{x} \in \partial\Omega_D^{u_{T/c}}\},\\
\forall\, \omega_{\phi} \in \mathscr{V}_{\phi}, \quad \mathscr{V}_{\phi} &= \{\omega_{\phi} \in H^1(\Omega) \mid \omega_{\phi} = 0 \,\forall\, \mathbf{x} \in \partial\Omega_D^{\phi}\}
\end{aligned}$$

$$\int_\Omega \boldsymbol{\omega}_{\boldsymbol{\nu}}\Big(\frac{\partial \boldsymbol{\nu}}{\partial t} + \boldsymbol{\nu}\cdot\boldsymbol{\nabla}\boldsymbol{\nu}\Big)\,d\Omega - \int_\Omega \boldsymbol{\nabla}.\boldsymbol{\omega}_{\boldsymbol{\nu}} p\,d\Omega + \int_\Omega \boldsymbol{\omega}_{\boldsymbol{\nu}}\eta h(1+\phi)^2\boldsymbol{\nu}\,d\Omega + \int_\Omega \eta(\boldsymbol{\nabla}\boldsymbol{\omega}_{\boldsymbol{\nu}}.\boldsymbol{\nabla}\boldsymbol{\nu})\,d\Omega + \int_{\partial\Omega_N^{\boldsymbol{\nu}}} \boldsymbol{\omega}_{\boldsymbol{\nu}}\Big(p - \boldsymbol{\nabla}\boldsymbol{\nu}\Big)\mathbf{n}\,dS = 0 \tag{4.2a}$$

$$\int_\Omega w_{u_T}\Big(\frac{\partial u_T}{\partial t} + \boldsymbol{\nu}.\nabla u_T - \frac{1}{2}\frac{\partial \phi}{\partial t}\Big)\,dV + \int_\Omega D\big(\boldsymbol{\nabla} w_{u_T}.\boldsymbol{\nabla} u_T\big)\,dV = 0 \tag{4.2b}$$

$$\int_\Omega w_\phi\Big(\tau\frac{\partial \phi}{\partial t} + \frac{\partial f}{\partial \phi}\Big)\,dV + \int_\Omega \lambda^2\boldsymbol{\nabla} w_\phi.\boldsymbol{\nabla}\phi\,dV + \int_\Omega |\boldsymbol{\nabla}\phi|^2\lambda\frac{\partial w_\phi}{\partial \mathbf{x}}\frac{\partial \lambda}{\partial\left(\frac{\partial \phi}{\partial \mathbf{x}}\right)}\,dV + \int_\Omega |\boldsymbol{\nabla}\phi|^2\lambda\frac{\partial w_\phi}{\partial \mathbf{y}}\frac{\partial \lambda}{\partial\left(\frac{\partial \phi}{\partial \mathbf{y}}\right)}\,dV = 0 \tag{4.2c}$$

$$\int_\Omega w_{u_c}\left(\Big(\frac{1+k}{2} - \frac{1-k}{2}\phi\Big)\frac{\partial u_c}{\partial t} + \boldsymbol{\nu}.\boldsymbol{\nabla} u_c - \Big(1 + (1-k)u_c\Big)\frac{1}{2}\frac{\partial \phi}{\partial t}\right)dV + \int_\Omega \tilde{D}\big(\frac{1-\phi}{2}\big)\boldsymbol{\nabla} w_{u_c}.\big(\boldsymbol{\nabla} u_c - \mathbf{J}_{at}\big)\,dV = 0 \tag{4.2d}$$

$$\int_{\Omega} w_{\phi} \left(\left(1 - (1-k) \frac{y - \tilde{\nu} t}{\tilde{l}_T} \right) a_s^2(\mathbf{n}) \frac{\partial \phi}{\partial t} + \left(\frac{\partial f}{\partial \phi} \right) \right) dV + \int_{\Omega} a_s^2 \boldsymbol{\nabla} w_{\phi} . \boldsymbol{\nabla} \phi \, dV \tag{4.2e}$$

$$+ \int_{\Omega} |\boldsymbol{\nabla} \phi|^2 a_s \frac{\partial w_{\phi}}{\partial x} \frac{\partial a_s}{\partial \left(\frac{\partial \phi}{\partial x} \right)} dV + \int_{\Omega} |\boldsymbol{\nabla} \phi|^2 a_s \frac{\partial w_{\phi}}{\partial y} \frac{\partial a_s}{\partial \left(\frac{\partial \phi}{\partial y} \right)} dV = 0$$

Here, $\mathbf{n}$ is the unit outward normal vector at the surface boundary. $\partial\Omega_N^{T/c}$ and $\partial\Omega_N^{v}$ are the boundaries for the temperature or concentration and velocity Neumann boundary conditions, respectively, and $\partial\Omega_D^{T/c}$ and $\partial\Omega_D^{v}$ are the boundaries for the temperature or concentration and velocity Dirichlet boundary conditions, respectively. $\boldsymbol{\omega}_{\mathbf{v}}$, $\omega_{u_{T,c}}$, and ω_{ϕ} belong to $H^1(\Omega)$ - the Sobolev space of functions that are square-integrable and have a square-integrable derivatives.

4.2.2 Computational details

The integral formulation described in Section 4.2.1 is implemented using the standard finite element method. An in-house MPI-based C++ code is developed with advanced capabilities such as adaptive meshing, implicit-explicit time-stepping, and iterative solvers. The code is built on top of deal.II finite element library (Arndt et al., 2021). Standard FEM constructs are adopted, and for all the simulations presented in this work, linear and quadratic Lagrange bases are used for pressure and other field variables such as temperature, solute concentration, order parameter, and velocity, respectively. The coupled Navier-Stokes equations are solved using Chorin's projection method (Chorin, 1997).

4.2.3 Fluid flow and solidification parameters

In this section, the parameters that were used in the phase-field model of pure metal and binary alloy solidification are listed. For the pure metal, non-dimensional parameters used in the phase-filed model are given in the Table 4.1. For the binary alloy solidification, the material properties for

Non-dimensional parameter	Numerical value
U_T	-0.75
Thermal diffusivity, $\tilde{D}$	1
Anisotropy strength, ϵ_4	0.05
Characteristic length-scale, λ_0	1
Characteristic time-scale, τ_0	1
Coupling parameter, ξ	1.60

Table 4.1: Input parameters for the phase-field model of solidification of a pure metal. The length-scale parameter λ_0 and the time-scale parameter τ_0 set the spatial and temporal resolution of the dendritic growth process.

the Al-4wt.% Mg is given in the Table 4.2. The dimensionless parameters used in the phase-field model are given in Table 4.3.

4.3 Results

The coupled numerical implementation of fluid flow and phase-field model is used to investigate the impact on the microstructure evolution. The impact is qualitatively understood by visualizing evolved dendrite morphology due to the influence of reheating and convection in the liquid melt during the solidification of pure metal and binary alloy materials. The impact of reheating or melting of a growing binary alloy dendrite is covered in Section 4.3.1.

Parameter	Numerical value (units)
Liquid phase diffusivity, D_l	3.0×10^{-9} $m^2 s^{-1}$
Solid phase diffusivity, D_s	1.0×10^{-12} $m^2 s^{-1}$
Partition coefficient, k	0.48
Anisotropy strength, ϵ_4	0.01
Gibbs-Thomson coefficient, Γ_g	1.30×10^{-7} m-K
Liquidus slope, m_l	-5. 07 $K(wt\%)^{-1}$
Initial concentration, c_0	4wt%
Thermal gradient, G	2.38×10^{-4} Km^{-1}
Pulling velocity, $\boldsymbol{\nu}_p$	4.25×10^{-3} ms^{-1}
Interface thickness, λ_0	6.25×10^{-8} m
Model constant, a_1	0.8839
Model constant, a_2	0.6267

Table 4.2: Material properties and phase-field model parameters for a binary alloy Al-4wt.% Mg (Geng et al., 2018)

Input parameters	Expression
Chemical capillary length, d_0	$\frac{k\Gamma}{mC_0(k-1)}$
Ratio of interface thickness to capillary length, Ξ	$\frac{\lambda_0}{d_0}$
Non-dimensional thermal diffusivity, $\tilde{D}$	$\frac{D_l \tau_0}{\lambda_0^2}$
Non-dimensional pulling velocity, $\tilde{\boldsymbol{\nu}}$	$\frac{\boldsymbol{\nu} \tau_0}{\lambda_0}$
Characteristic thermal length-scale, $\tilde{L_T}$	$\frac{\lvert m_l \rvert (1-k) c_0}{kG\lambda_0}$
Characteristic time-scale, τ_0	$\frac{a_1 a_2 \xi \lambda_0^2}{D_l}$
Coupling parameter, ξ	$a_1 \Xi$

Table 4.3: Input parameters for the phase-field model of solidification of a binary metallic alloy. The numerical values of the input parameters are computed using the expressions shown here that are in terms of the properties listed in Table 4.2.

4.3.1 Effect of reheating on binary alloy solidification

In this section, the effect of reheating on the solidification of a binary alloy is discussed. During the laser powder bed fusion process, a new powder layer is added to the previously solidified layer. The laser then moves over the newly added layer in a predefined path melting the powder layer which creates a meltpool. The depth of the meltpool is dependent on the laser power and laser scan velocity. The slowly moving and high-power laser results in a meltpool with a depth equal to multiple layers. This results in the remelting of the previously solidified structures affecting the microstructure. This remelting of solidified or solidifying dendrites is modeled in this section. The impact of fluid flow in the liquid melt is not considered. The solidification and remelting are modeled using the phase-field method of binary alloy solidification given by Equation 4.1e-4.1f. The convection term $\boldsymbol{\nu}.\boldsymbol{\nabla} u_c$ is neglected. An initial semi-circular seed is placed in the undercooled alloy melt. The frozen temperature approximation governs the evolution of the temperature by $T = T_m + G(y - \boldsymbol{\nu}_p t)$ where T_m is the melting temperature, y is the vertical position in the domain, G is the temperature gradient in the liquid meltpool (Echebarria et al., 2004). The magnitude of G is set by the laser power and material properties of the powdered alloy. $T = T_m$ is the current temperature at the interface when $G(y - \boldsymbol{\nu}_p t) = 0$. The direction of pulling velocity is $\boldsymbol{\nu}_p$ is such solid-liquid interface moves from $y = 0$ at $t = 0$ to some $y = y'$ at $t = t'$. During the solidification, T decreases below T_m with time at each location y. The remelting can be modeled by reversing the direction of solid-liquid interface motion and modifying temperature relation as $T = T_m + G(y + \boldsymbol{\nu}_p' t)$ during solidification where $\boldsymbol{\nu}_p'$ is the velocity of moving solid-liquid interface (Yue et al., 2022). The model parameters are given in Table 4.3 -4.3. A uniform time step size $dt = 0.04$ and adaptive meshing with minimum mesh size $\Delta x = 0.8$ was used. At time $t = 0$, a small semi-circular seed is provided with $\phi = 1$ inside the seed and $\phi = -1$ outside

everywhere. The concentration undercooling is taken to be $u_c = -0.5$ everywhere at $t = 0$. Neumann boundary conditions $\nabla u_c = 0$ and $\nabla \phi = 0$ are provided on all four boundaries. Until $t = 280$, solid-liquid contour moves at pulling velocity $\boldsymbol{\nu}_p = 0.52$ and after $t = 280$, $\boldsymbol{\nu}_p = 13.0$ to demonstrate the rapid melting of a binary alloy. At the onset of remelting, the phase-filed model is updated by changing the term $\left(u_c + \frac{y - \tilde{\nu} t}{\tilde{l}_T}\right)$ to $\left(u_c + \frac{y + \tilde{\nu'} t}{\tilde{l}_T}\right)$ in Equation 4.1f. The Figure 4.1 shows evolving dendritic shape represented by solute concentration c and order parameter ϕ at time (t). At $t = 276$, the dendrite grows with primary and secondary arms. The solute concentration inside the solid seed is $c = kc_l^0 = 0.4 * 4 = 1.68$ and near the solid-liquid interface solute concentration is highest $c = 4.0$ Away from the interface into the liquid melt, the solute concentration is governed by the diffusion in the liquid phase. The higher concentration is just after the interface and concentration diminishes or diffused away from the interface. With the onset of remelting, the solid phase starts to shrink as evident from order parameter ϕ at $t = 284$. The remelting is visible in the form of receding of the interface along with diminishing of primary and secondary arms thickness. In terms of solute concentration, the melted solid phase, replenished the liquid melt resulting in a higher concentration in the liquid around the interface. At $t = 344$, more region in the liquid alloy melt has higher solute concentration and correspondingly more diminished solid dendrite structure. The remelting also results in the pinching off of secondary arms from the primary arms evident in Figure 4.1 at $t = 344$. These pinched-off arms on further solidification acts as nucleus seeds thereby altering the microstructure pattern in full solidification and reheating cycle.

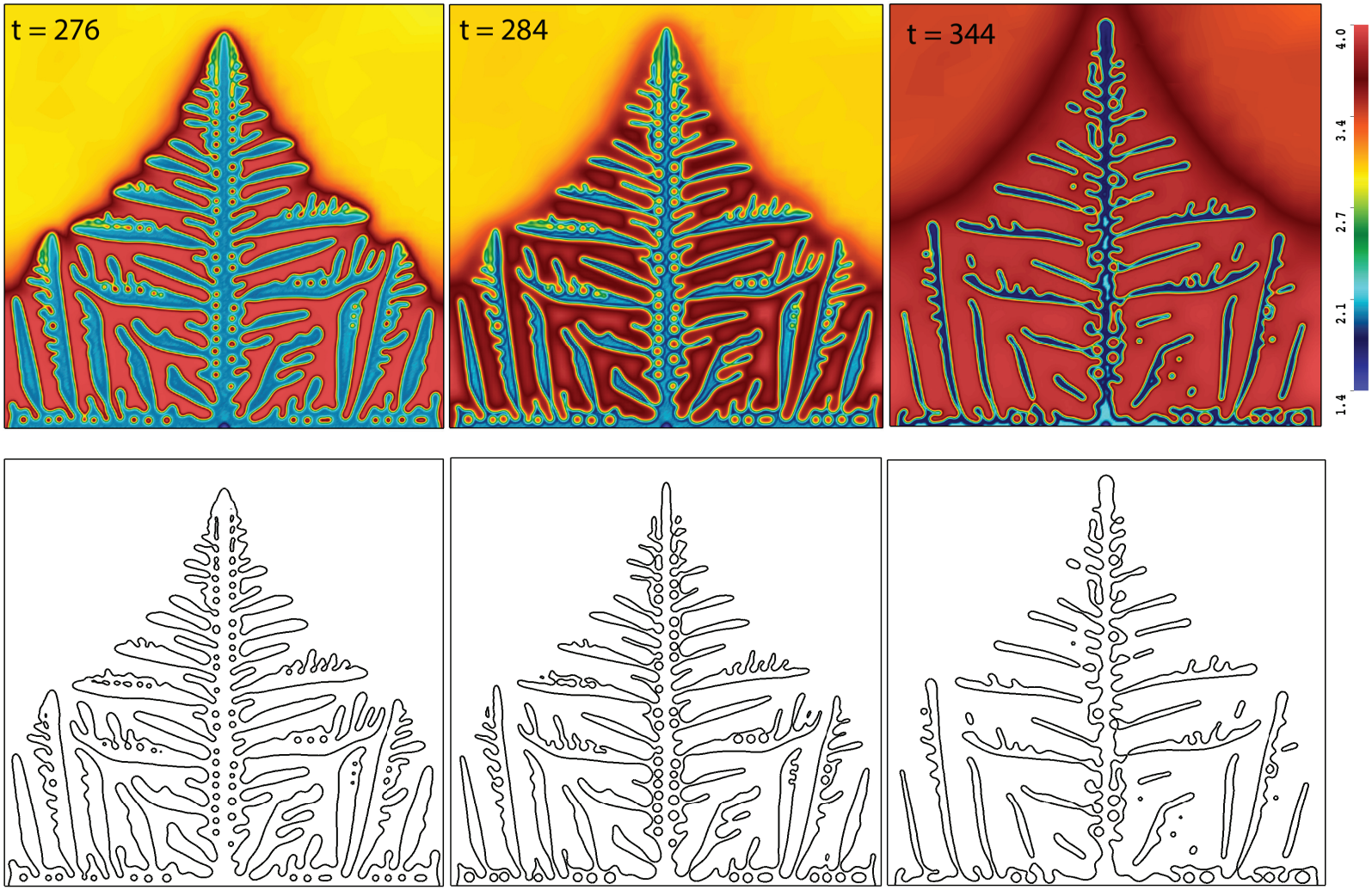

Figure 4.1: Evolution of an Al-4% Mg alloy dendrite. First three column figures represent solute concentration c at t= 276, 284, and t = 344. Second column three figure represents order parameter ϕ at the same time instant.

4.3.2 Convection driven growth of pure melt solidification

In the previous section, the effect of remelting on the anisotropic dendritic morphology was studied. The remelting is modeled with the increase in temperature. In this section, the anisotropic dendritic growth of pure metal is investigated under the influence of different fluid flow and dendrite orientation. The fluid flow is modeled by solving continuity and momentum conservation represented by Equation 4.1a-4.1b. The coupled pure metal solidification is modeled by solving phase-field model represented by Equation 4.1c-4.1d. Two different types of fluid flow are considered , namely (1) Flow through a channel, and (2) Marangoni convection inside a cavity.

Flow through a channel

A square computational domain with unitless dimension 500×500 is chosen. A uniform time step size $\Delta t = 0.5$ and adaptive meshing refinement with minimum mesh size $\Delta x = 2.0$ is used. The fluid flow model is solved with dimensionless parameters such as viscosity $\eta = 500$, and permeability parameter $h = 1.0$. The phase-field model parameters are chosen from Table 4.1. At time $t = 0$, velocity vector $\boldsymbol{\nu} = 0$, pressure $p = 500 - x$ is chosen as an initial condition for fluid flow. Solidification is initiated with a small circular seed at the center of the domain with $\phi = 1$ inside the seed and $\phi = -1$ everywhere. Initial temperature undercooling is taken to be $u_T = -0.75$ everywhere. The boundary condition for the coupled fluid flow and phase-field solidification model is chosen as $\boldsymbol{\nu} = 0.2, 0$ at the inlet, $\boldsymbol{\nu}_x = 0$ at the outlet, and $\boldsymbol{\nu} = 0$ on the top and bottom sides. Pressure $p = 0$ at the outlet. Neumann boundary condition $\boldsymbol{\nabla} u_T = 0$ and $\boldsymbol{\nabla}\phi = 0$ are applied on all sides. With the onset of solidification, solid seed starts to grow due to heat diffusion as governed by the phase-field model. The

liquid melt starts to flow around the dendrite with velocity vectors pointing from inlet toward outlet. The solid region is at the higher temperature and the surrounding liquid is at the lower temperature. As seen in Figure 4.2, the fluid flows from inlet to outlet. The flow is zero at the side walls due to no-slip boundary condition. The fluid velocity decreases as the fluid particle gets closer to the dendrite interface with velocity reducing by several orders of magnitude inside the dendrite due to momentum sink term $\eta h(1+\phi)^2$. The growth of dendrites is governed by heat diffusion and surface anisotropy. Due to presence of strong convection, the diffusion growth is dominated or aided by the liquid melt. In the region where liquid melt velocity $\boldsymbol{\nu}$ is directed away from inlet and solid dendrite arm is moving towards the inlet, the growth is fastest. This is observed by comparing the shape of dendrite at time $t = 150$, $t = 350$, and $t = 750$ in Figure 4.2. The colder liquid melt flowing from left end to right end ensures hotter dendrite grows faster in the opposite direction. However, when liquid melt velocity $\boldsymbol{\nu}$ and dendrite arm both move towards outlet, the growth of dendrite is slowest. In this case, the growth of hotter dendrite is restricted by the colder flowing liquid melt carrying away heat and diminishing heat diffusion. The growth of primary arms in the horizontal direction is unaffected by the fluid flow because $\boldsymbol{\nu}.\boldsymbol{\nabla} u_T = 0$. This lopsided growth alters the final anisotropic shape of equiaxed dendrite. The fluid flow condition considered in this case is not representative of fluid flow in the meltpool during the additive solidification. Nevertheless, the fluid flow through a channel and pure metal solidification case helps us understand altered microstructure evolution in the presence of convection.

Marangoni covection inside a cavity

In the second case, circulating fluid flow is considered inside the computational domain, and the effect of this circulating flow on the solidification of

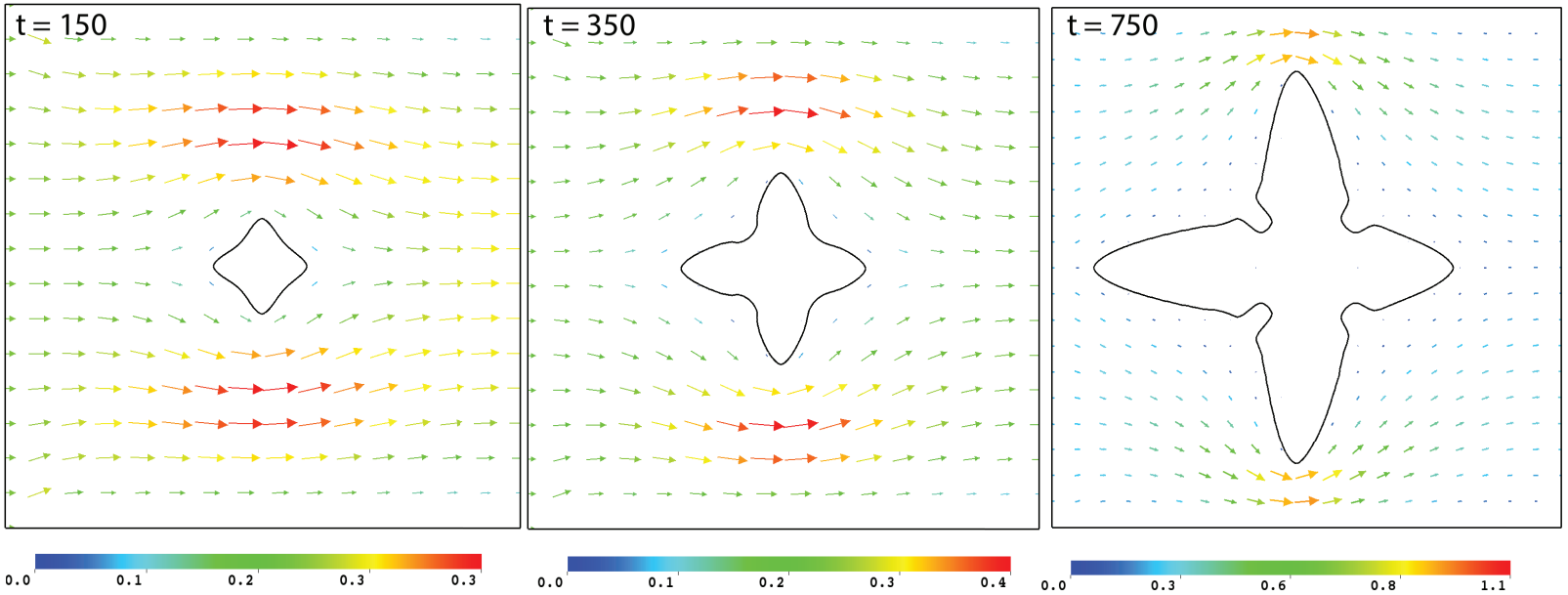

Figure 4.2: Evolution of pure metal dendrite and the liquid melt velocity vectors representing flow through a channel with obstruction t = 150, 350 and 750. Figure is rotated counterclockwise by 90°. Observe that the dendrite shape is biased and grows faster in the direction opposite to the flow.

pure melt is considered. As a boundary condition, the gradient of velocity ($\frac{\partial v}{\partial x} = \frac{A(2x-L)}{L}$) is specified at the top end to mimic the Marangoni flow observed inside the meltpool. Here $A = -100$ is the parameter controlling the magnitude of maximum velocity. The fluid flow circulation is clockwise in the left half of the domain and it is counter-clockwise in the right half of the domain. This is as per fluid flow observed in the meltpool in the LPBF process. No-slip boundary condition is specified $v = 0$ at the other three sides of the computational domain. Pressure $p = 0$ is specified on the top end. The rest of the parameters are same as before. As seen in Figure 4.3, the solid seed is placed at the center of the undercooled melt. At $t = 150$, growth of four primary is visible with the arm growing towards top end visibly larger than the other three primary arms. The fluid flow around the dendrite arms growing towards top end is downward. Thus, its growth is faster than other arms. At $t = 350 - 600$, the lopsided or uneven growth of dendrite is apparent in Figure 4.3. The equiaxed dendrite growth of pure melt is heavily influenced as compared to its anisotropic diffusion growth due to strong convection in the liquid melt. In the Figure 4.4, growth of dendrite oriented at an angle 20^0 with the vertical is modeled with the Marangoni convection in the liquid melt. From $t = 150-600$, the fastest growth is observed in the primary arm moving towards top end. The final microstructure evolved in the presence of convection in the liquid melt differs significantly from that of microstructure evolved under pure heat diffusion process and these altered morphology of dendrite affects the material properties of the material.

4.3.3 Convection driven growth of binary alloy solidification

In this section, anisotropic dendritic growth of binary alloy is investigated under the influence of different fluid flow conditions. As before the fluid flow is modeled by solving continuity and momentum conservation rep-

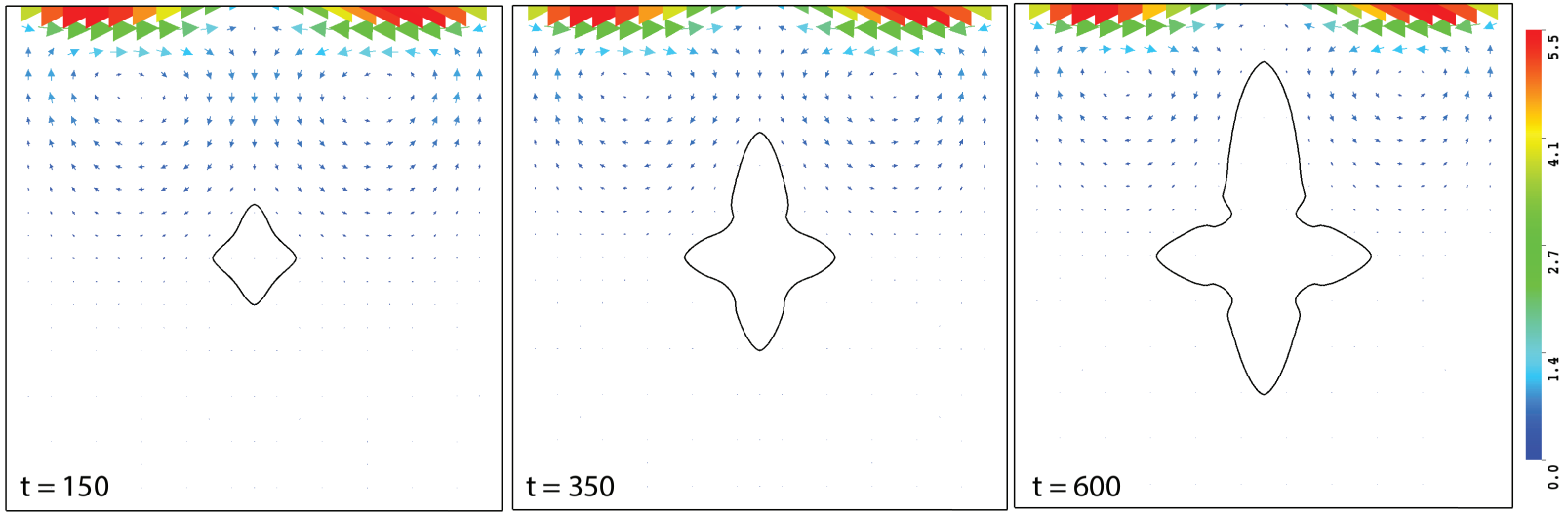

Figure 4.3: Evolution of pure metal dendrite and the liquid melt velocity vectors representing Marangoni flow inside a cavity at t = 150, 350, and 600. Figure is rotated counterclockwise by 90°.

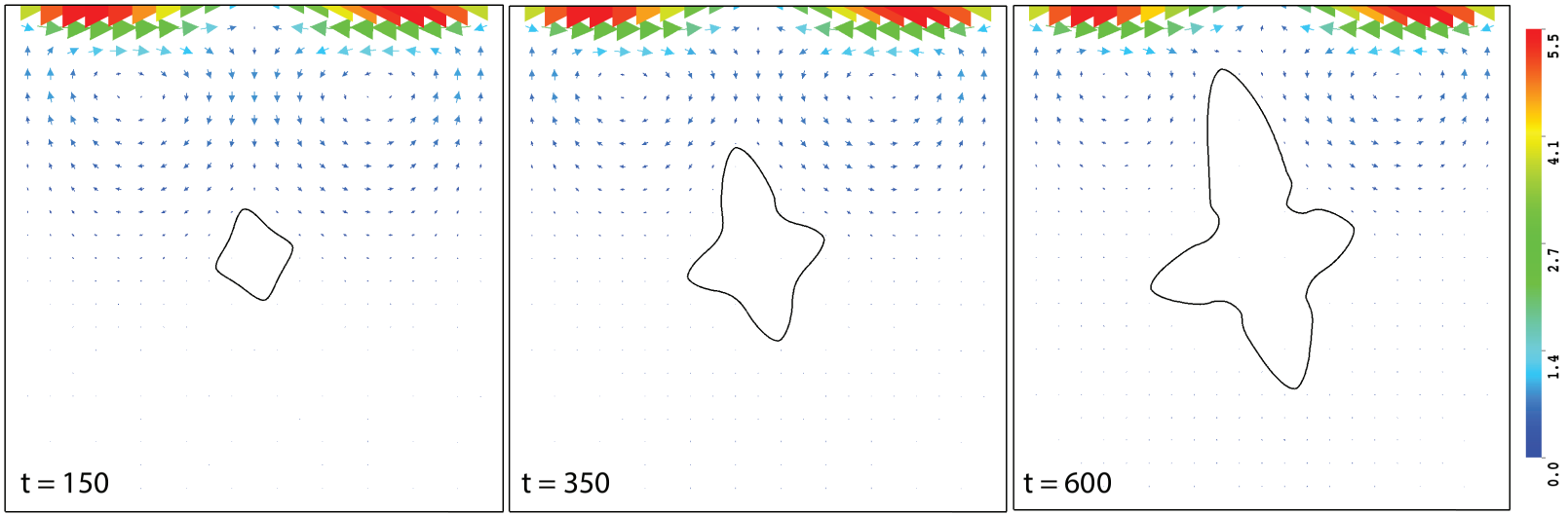

Figure 4.4: Evolution of pure metal dendrite oriented at $\theta = 20^0$ and the liquid melt velocity vectors representing Marangoni flow inside a cavity at t = 150, 350 and 600. Figure is rotated counter clockwise by 90°.

resented by Equation 4.1a-4.1b. The coupled binary alloy solidification is modeled by solving the phase-field model represented by Equation 4.1e-4.1f.

Flow through a channel

A square computational domain with unitless dimension 600×600 is chosen. A uniform time step size $\Delta t = 0.05$ and adaptive meshing refinement with minimum mesh size $\Delta x = 2.3$ is used. The fluid flow model is solved with dimensionless parameters such as viscosity $\eta = 500$, and permeability parameter $h = 1.0$. The phase-field model parameters are chosen from Table 4.3-4.2. At time $t = 0$, velocity vector $\boldsymbol{v} = 0$, pressure $p = 500 - x$ is chosen as an initial condition for fluid flow. Solidification is initiated with a small circular seed at the center of the domain with $\phi = 1$ inside the seed and $\phi = -1$ everywhere. Initial concentration undercooling is taken to be $u_c = -0.5$ everywhere. The boundary condition for the coupled fluid flow and phase-field solidification model is chosen as $\boldsymbol{v} = 0.5, 0$ at the inlet, $\boldsymbol{v}_x = 0$ at the outlet, and $\boldsymbol{v} = 0$ on the sides. Pressure $p = 0$ at the outlet end. Neumann boundary condition $\boldsymbol{\nabla} u_c = 0$ and $\boldsymbol{\nabla}\phi = 0$ are applied on all sides. With the onset of solidification, the solid seed starts to grow due to solute diffusion in the liquid melt as governed by the phase-field model of binary alloy solidification. The alloy liquid melt starts to flow around the dendrite with velocity vectors pointing inlet to the outlet end. The solute concentration near the interface from the liquid side is higher than the bulk alloy liquid melt region away from the interface. As seen in Figure 4.5, the fluid flows from inlet to outlet end. The flow is zero at the side walls due to the no-slip boundary condition. The fluid velocity decreases as the fluid particle gets closer to the dendrite interface with velocity reducing by several orders of magnitude inside the dendrite due to momentum sink term $\eta h(1+\phi)^2$. The growth of dendrites is governed by solute diffusion and surface anisotropy. Due to the presence of strong

convection, the diffusion growth is dominated or aided by the alloy liquid melt. In the region where liquid melt velocity $\boldsymbol{\nu}$ is directed from inlet to exit and the solid dendrite arm moving towards inlet, the growth is fastest. This is observed by comparing the shape of dendrite at time $t = 20$, $t = 60$, and $t = 100$ in Figure 4.5. The highly undercooled alloy liquid melt $u_c = -0.5$ is flowing from left end to right end ensuring low undercooled alloy in the liquid phase near the interface is advected and the solid alloy is diffused faster thus solid dendrite pointing towards inlet is growing faster. However, when liquid melt velocity $\boldsymbol{\nu}$ and the dendrite arm both move towards outlet, the growth of dendrite arm is slowest. In this case, the growth of dendrite is restricted by the undercooled alloy liquid melt keeping the region around the interface more solute-rich. The growth of primary arms in the vertical direction is unaffected by the fluid flow because $\boldsymbol{\nu}.\boldsymbol{\nabla} u_c = 0$. This lopsided growth alters the final anisotropic shape of equiaxed binary alloy dendrite.

Marangoni covection inside a cavity

In the second case, as described in Section 4.3.3, circulating fluid flow is considered inside the computational domain, and the effect of this circulating flow on the solidification of a binary alloy is considered. As a boundary condition, the gradient of velocity ($\frac{\partial \boldsymbol{\nu}}{\partial \boldsymbol{x}} = \frac{A(2x-L)}{L}$) is specified at the top end to mimic the Marangoni flow observed inside the meltpool. In this case, $A = -250$ is chosen. As seen in Figure 4.6, the solid seed is placed at the center of the undercooled alloy melt. At $t = 20$, growth of four primary arms is visible. The solute concentration in the liquid region just after the interface is higher and the solute concentration far away from the interface is lower. As alloy liquid melts flowing down near the dendrite arms, it creates conducive conditions for the solute-rich region to grow and thus growth of that primary arm is faster. This is visible by looking at the length of the primary arm growing toward top end at

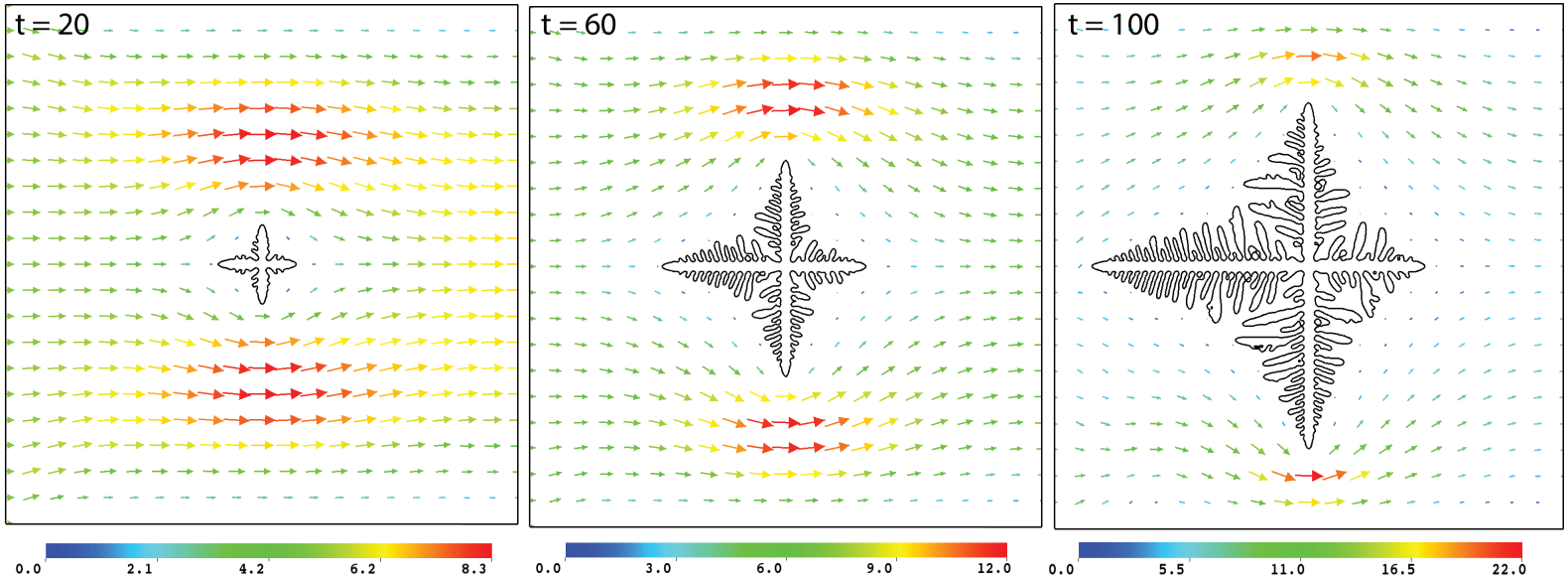

Figure 4.5: Evolution of binary alloy dendrite and the liquid melt velocity vectors representing flow through a channel at t = 20, 60 and 100. Figure is rotated counterclockwise by 90°. Observe that the dendrite shape is biased and grows faster in the direction opposite to the flow.

$t = 60$ and $t = 100$ in the Figure 4.6-4.7. Another interesting phenomenon observed is the growth of secondary arms of the primary arm growing vertically upwards is less pronounced as compared growth of secondary arms on the primary arm growing vertically downwards. This is the result of fluid flow conditions aligning with the growth of secondary arms in the circulation motion thereby diminishing its growth. However, the secondary arms on the vertically downward-moving dendrite grow faster due to unhindered solute diffusion. This uneven growth of primary and secondary arms alters the anisotropic growth and thereby affecting the final microstructure evolution in the vigorously circulating fluid flow in the meltpool.

4.3.4 Convection driven growth of columnar dendrite in binary alloy solidification

In this section, the effect of circulating fluid flow on the growth of columnar dendrites is considered. As before the circulating fluid flow is set up using the boundary condition by specifying the gradient of velocity as $(\frac{\partial \nu}{\partial x} = \frac{A(2x-L)}{L})$. Two different values of A are specified. In the first case, $A = -4.5 \times 10^2$ was used and in the other case $A = -10^{-2}$ was used. The magnitude of A is governed by the laser power (P) and laser scan speed(ν_p). Meltpool formed in additive process with a high value of $(P, \boldsymbol{\nu}_p)$ will have significant Marangoni convection as compared to meltpool formed with a low value of (P, ν_p). To model the growth of the columnar dendrite alloy, five solid hemispherical seeds were placed at the bottom of the computational domain at time $t = 0$. The phase-field variable is taken as $\phi = 1$ inside the seed and $\phi = -1$ everywhere in the domain. Everywhere the concentration undercooling is taken as $u_c = -0.5$. As seen in Figure 4.8, the three snapshot in the first column shows the morphology of columnar dendrite and velocity vector in the alloy melt at three time instant $t = 100$, $t = 220$, and $t = 260$. These

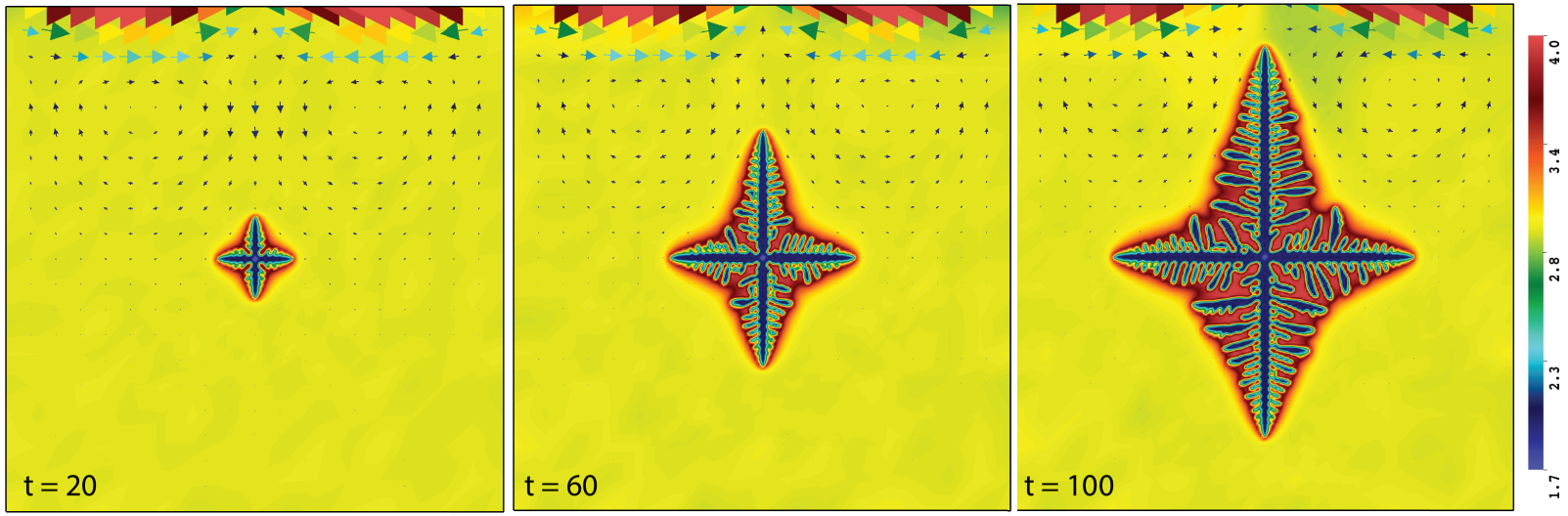

Figure 4.6: Solution concentration of binary alloy dendrite and the liquid melt velocity vectors representing Marangoni flow inside a cavity at t = 20, 60, and 100. Figure is rotated counterclockwise by 90°. Observe that the dendrite shape is biased and grows faster in the direction opposite to the flow.

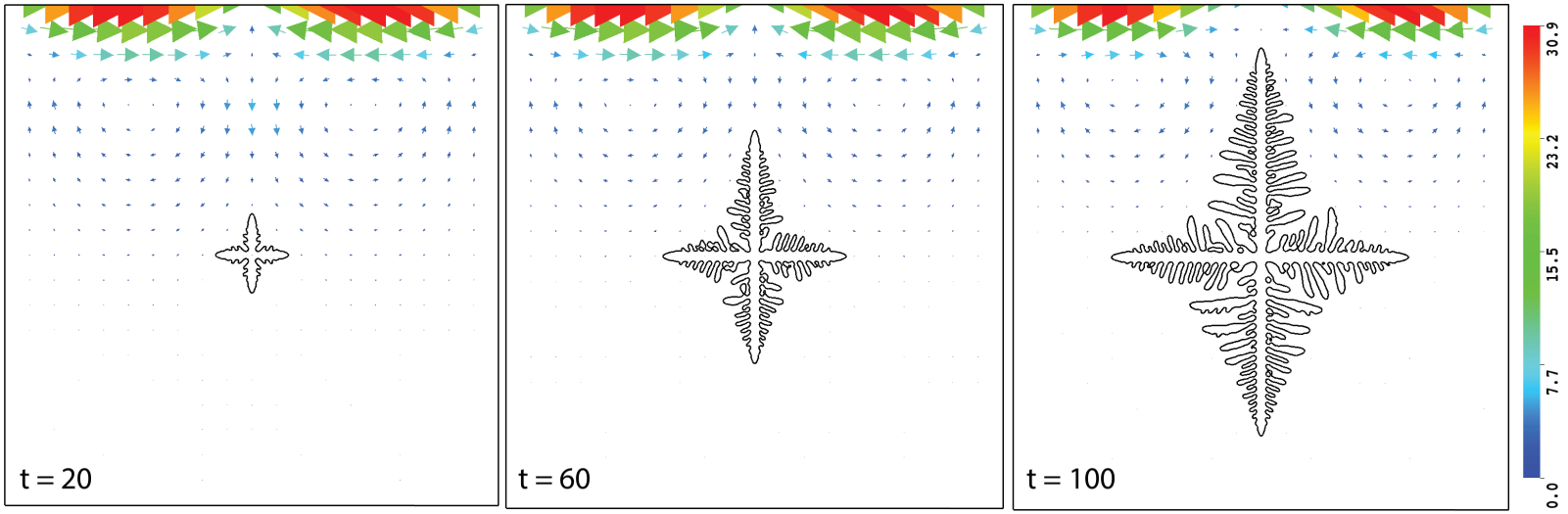

Figure 4.7: Evolution of binary alloy dendrite and the liquid melt velocity vectors representing Marangoni flow inside a cavity at t = 20, 60 and 100. Figure is rotated counterclockwise by 90°. Observe that the dendrite shape is biased and grows faster in the direction opposite to the flow.

three cases correspond to high Marangoni convection with $A = -4.5 \times 10^2$. The other three snapshots in the second column are the morphology of columnar dendrite for the low Marangoni convection with $A = 10^{-4}$. As dendrite grows vertically towards the top of the computational domain, the primary dendrite arms experiences flow moving downwards. This is apparent by looking at the direction of the flow at time $t = 220$. When velocity magnitude vector $\boldsymbol{\nu}$ is high, the convection-assisted growth results in the faster growth of primary arms of columnar dendrite. The dendrite grew faster for the case when $A = -4.5 \times 10^2$ as compared to the case when $A = -10^{-4}$. At time $t = 260$, the primary arms reach close to liquid melt where velocity vector is $\boldsymbol{\nu}$ is aligned perpendicular to primary arms. The secondary arms on the primary arms are inclined with velocity vector $\boldsymbol{\nu}$ such that its growth is accelerated. This behavior is apparent when for the case when $A = -4.5 \times 10^2$ at time $t = 260$. This uneven growth of the primary and secondary arms in the presence of Marangoni convection results in vastly different dendrite morphology. As a result, the spacing between primary and dendrite arms and the anisotropic growth is influenced. These effects have a bearing on the mechanical properties of the solidified alloy.

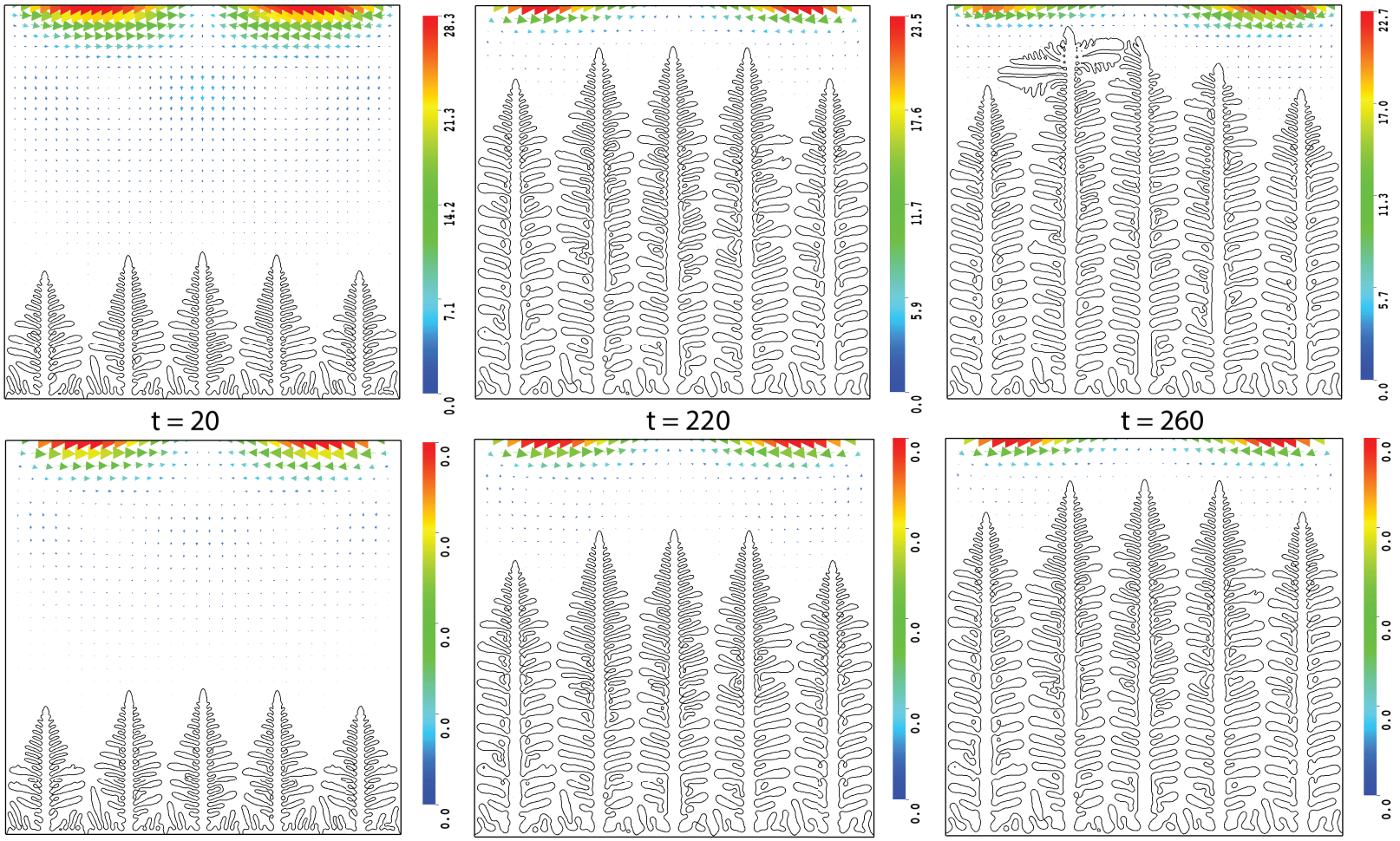

Figure 4.8: Evolution of columnar binary alloy dendrite and the liquid melt velocity vectors representing Marangoni flow in a cavity. Left three figures represent dendrite morphology at t = 100, 220, and 260 for $A = -4.5 \times 10^2$. Right three figures represent dendrite morphology at t = 100, 220 and 260 for $A = -10^{-4}$. Figure is rotated counterclockwise by 90°. Observe that the dendrite shape is biased and grows faster in the direction opposite to the flow.

5 CONCLUSIONS

In summary, various microstructural and multiscale analysis and modeling aspects underlying metal additive manufacturing have been modeled in this thesis. In the first part, a detailed development of the requisite numerical aspects of dendritic solidification theory, and the computational implementation of the corresponding phase-field formulations to model dendritic growth in pure metals and binary alloys is presented. A wide variety of physically relevant dendritic solidification patterns are modeled by solving the governing equations under various initial conditions and boundary conditions. To validate the numerical framework, the classical four-fold symmetric dendrite shape occurring in undercooled pure melt is simulated and numerically computed dendritic tip velocities is compared with the corresponding analytical values obtained using a Green's function approach. Further, this problem is used as a basis for performing error convergence studies of dendritic tip velocity and dendritic morphology (primal fields of temperature and order parameter). The distinguishing aspects of this work are - a unified treatment of both pure-metals and alloys; novel numerical error estimates of dendritic tip velocity; and the study of error convergence of the primal fields of temperature and the order parameter with respect to the numerical discretization.

In the second part, the meltpool dynamics of the laser powder bed fusion (LPBF) process are numerically modeled and connections are made to important dimensionless quantities influencing the thermo-fluidic evolution of the meltpool and its morphology. The simulation predictions were validated by comparing with available results from the literature and with experimental observations of the cooling rates available from our experimental collaborators. Using the dimensionless form of governing equations and the finite-element simulations, an important dimensionless quantity, interpreted as the heat absorbed by the metal powder and the

meltpool, is identified. Around sixty different cases of the LPBF process were simulated by varying the alloy type and the process conditions, and the simulation data was used to obtain an explicit form of the dimensionless heat absorbed in terms of the input dimensionless numbers using the method of linear least-squares regression. Using physics-based and statistical arguments, a linear model showing dependence of the heat absorbed on the Péclet number and the dimensionless power is established. The measure of advection inside the meltpool, meltpool morphology such as aspect ratio and volume, and solidification cooling rates are correlated with dimensionless heat absorbed and classical dimensionless numbers such as Péclet , Marangoni and Stefan numbers for different alloy materials. Such characterization of meltpool using classical dimensionless numbers and the impact of dimensionless power and Péclet number on the solidification cooling rates is a novel contribution of this work.

In the third part, a coupled numerical treatment of Navier-Stokes flow equations and a phase-field model of dendritic solidification is presented. A mix of different convection conditions is considered to investigate the impact of fluid flow in the liquid on the diffusion of heat and mass in pure metal and binary alloy solidification. In particular, fluid flow through a closed channel and Marangoni convection inside a cavity are used as representative fluid flow mechanisms. A wide variety of physically relevant dendritic solidification patterns such as equiaxed, aligned equiaxed dendrites, and columnar dendrites are considered in this work. It was found that primary and secondary dendrites arms grow significantly faster if they are aligned opposite to the direction of the liquid melt velocity. The magnitude of the temperature gradient in the meltpool during the laser powder bed fusion process determines the degree of re-circulation in the liquid melt. The growth of secondary dendrite arms of columnar dendrite under such conditions is non-uniform and overgrown than the case with dendrite growth in a low re-circulation meltpool. Further, the

impact of remelting of dendrite arms is investigated using the phase-field model and reversal of solid-liquid interface direction. Modeling and investigating the effect of fluid flow and remelting on the heat and mass diffusion-based anisotropic growth of dendrites, and its impact on the resulting microstructure evolution are the distinguishing aspects of this work.

2012. VisIt: An End-User Tool For Visualizing and Analyzing Very Large Data. `https://visit.llnl.gov`.

Abolhasani, Daniyal, SM Hossein Seyedkashi, Namhyun Kang, Yang Jin Kim, Young Yun Woo, and Young Hoon Moon. 2019. Analysis of melt-pool behaviors during selective laser melting of aisi 304 stainless-steel composites. *Metals* 9(8):876.

Ahsan, Faiyaz, Jafar Razmi, and Leila Ladani. 2022. Global local modeling of melt pool dynamics and bead formation in laser bed powder fusion additive manufacturing using a multi-physics thermo-fluid simulation. *Progress in Additive Manufacturing* 1–11.

Al-Rawahi, Nabeel, and Gretar Tryggvason. 2002. Numerical simulation of dendritic solidification with convection: two-dimensional geometry. *Journal of Computational Physics* 180(2):471–496.

———. 2004. Numerical simulation of dendritic solidification with convection: Three-dimensional flow. *Journal of Computational Physics* 194(2): 677–696.

Almgren, Robert F. 1999. Second-order phase field asymptotics for unequal conductivities. *SIAM Journal on Applied Mathematics* 59(6):2086–2107.

Anderson, Daniel M, Geoffrey B McFadden, and Adam A Wheeler. 2000. A phase-field model of solidification with convection. *Physica D: Nonlinear Phenomena* 135(1-2):175–194.

Ansari, Md Jonaet, Dinh-Son Nguyen, and Hong Seok Park. 2019. Investigation of slm process in terms of temperature distribution and melting pool size: Modeling and experimental approaches. *Materials* 12(8):1272.

Ansari, Peyman, Asif Ur Rehman, Fatih Pitir, Salih Veziroglu, Yogendra Kumar Mishra, Oral Cenk Aktas, and Metin U Salamci. 2021. Selective laser melting of 316l austenitic stainless steel: Detailed process understanding using multiphysics simulation and experimentation. *Metals* 11(7):1076.

Arndt, Daniel, Wolfgang Bangerth, Bruno Blais, Marc Fehling, Rene Gassmöller, Timo Heister, Luca Heltai, Uwe Köcher, Martin Kronbichler, Matthias Maier, Peter Munch, Jean-Paul Pelteret, Sebastian Proell, Konrad Simon, Bruno Turcksin, David Wells, and Jiaqi Zhang. 2021. The `deal.II` library, version 9.3. *Journal of Numerical Mathematics* 29(3):171–186.

Asztalos, Zsolt, Ioan Száva, Sorin Vlase, and Renáta-Ildikó Száva. 2022. Modern dimensional analysis involved in polymers additive manufacturing optimization. *Polymers* 14(19):3995.

Beckermann, C, and CY Wang. 1996. Equiaxed dendritic solidification with convection: Part iii. comparisons with nh 4 cl-h 2 o experiments. *Metallurgical and Materials Transactions A* 27:2784–2795.

Beckermann, Christoph, H-J Diepers, Ingo Steinbach, Alain Karma, and Xinglin Tong. 1999. Modeling melt convection in phase-field simulations of solidification. *Journal of Computational Physics* 154(2):468–496.

Ben-Jacob, Eshel, and Peter Garik. 1990. The formation of patterns in non-equilibrium growth. *Nature* 343(6258):523–530.

Bertsch, KM, G Meric De Bellefon, B Kuehl, and DJ Thoma. 2020. Origin of dislocation structures in an additively manufactured austenitic stainless steel 316l. *Acta Materialia* 199:19–33.

Bhagat, K. 2022a. Meltpool thermo-fluidics simulation framework for metal additive manufacturing. `https://github.com/cmmg/AMMeltpoolThermoFluidics`.

———. 2022b. Phase-field based dendritic modeling. `https://github.com/cmmg/dendriticGrowth`.

Bhagat, Kunal, and Shiva Rudraraju. 2022. Modeling of dendritic solidification and numerical analysis of the phase-field approach to model complex morphologies in alloys. *arXiv preprint arXiv:2210.14449*.

Bieterman, M, and I Babuška. 1982. The finite element method for parabolic equations. *Numerische Mathematik* 40(3):373–406.

Bluman, George W, and Sukeyuki Kumei. 2013. *Symmetries and differential equations*, vol. 81. Springer Science & Business Media.

Boettinger, William J, James A Warren, Christoph Beckermann, and Alain Karma. 2002. Phase-field simulation of solidification. *Annual review of materials research* 32(1):163–194.

Brent, AD, Vaughan R Voller, and KTJ Reid. 1988. Enthalpy-porosity technique for modeling convection-diffusion phase change: application to the melting of a pure metal. *Numerical Heat Transfer, Part A Applications* 13(3):297–318.

Burbelko, Andriy A, Edward Fraś, Wojciech Kapturkiewicz, and Daniel Gurgul. 2010. Modelling of dendritic growth during unidirectional solidification by the method of cellular automata. In *Materials science forum*, vol. 649, 217–222. Trans Tech Publ.

Caginalp, G. 1989. Stefan and hele-shaw type models as asymptotic limits of the phase-field equations. *Physical Review A* 39(11):5887.

Caginalp, Gunduz. 1986. An analysis of a phase field model of a free boundary. *Archive for Rational Mechanics and Analysis* 92(3):205–245.

Cardaropoli, Francesco, Vittorio Alfieri, Fabrizia Caiazzo, and Vincenzo Sergi. 2012. Dimensional analysis for the definition of the influence of

process parameters in selective laser melting of ti–6al–4v alloy. *Proceedings of the Institution of Mechanical Engineers, Part B: Journal of Engineering Manufacture* 226(7):1136–1142.

Chen, Chuanjun, and Xiaofeng Yang. 2019. Efficient numerical scheme for a dendritic solidification phase field model with melt convection. *Journal of Computational Physics* 388:41–62.

Chen, S, B Merriman, Smereka Osher, and P Smereka. 1997. A simple level set method for solving stefan problems. *Journal of Computational Physics* 135(1):8–29.

Chia, Hou Yi, Jianzhao Wu, Xinzhi Wang, and Wentao Yan. 2022. Process parameter optimization of metal additive manufacturing: a review and outlook. *Journal of Materials Informatics* 2(4):16.

Chorin, Alexandre Joel. 1997. A numerical method for solving incompressible viscous flow problems. *Journal of computational physics* 135(2): 118–125.

Cimolin, Flavio, and Marco Discacciati. 2013. Navier–stokes/forchheimer models for filtration through porous media. *Applied Numerical Mathematics* 72:205–224.

Collins, Joseph B, and Herbert Levine. 1985. Diffuse interface model of diffusion-limited crystal growth. *Physical Review B* 31(9):6119.

Curtis, WD, J David Logan, and WA Parker. 1982. Dimensional analysis and the pi theorem. *Linear Algebra and its Applications* 47:117–126.

Dantzig, Jonathan A, and Michel Rappaz. 2016. *Solidification: -revised & expanded*. EPFL press.

Davis, Stephen H. 1990. Hydrodynamic interactions in directional solidification. *Journal of Fluid Mechanics* 212:241–262.

DeWitt, Stephen, Shiva Rudraraju, David Montiel, W Beck Andrews, and Katsuyo Thornton. 2020. Prisms-pf: A general framework for phase-field modeling with a matrix-free finite element method. *npj Computational Materials* 6(1):1–12.

Dinovitzer, Malcolm, Xiaohu Chen, Jeremy Laliberte, Xiao Huang, and Hanspeter Frei. 2019. Effect of wire and arc additive manufacturing (waam) process parameters on bead geometry and microstructure. *Additive Manufacturing* 26:138–146.

Dong, Zhichao, Yabo Liu, Weibin Wen, Jingran Ge, and Jun Liang. 2018. Effect of hatch spacing on melt pool and as-built quality during selective laser melting of stainless steel: Modeling and experimental approaches. *Materials* 12(1):50.

Echebarria, Blas, Roger Folch, Alain Karma, and Mathis Plapp. 2004. Quantitative phase-field model of alloy solidification. *Physical Review E* 70(6):061604.

Fallah, V, M Amoorezaei, N Provatas, SF Corbin, and A Khajepour. 2012. Phase-field simulation of solidification morphology in laser powder deposition of ti–nb alloys. *Acta Materialia* 60(4):1633–1646.

Farzadi, A, Minh Do-Quang, S Serajzadeh, AH Kokabi, and Gustav Amberg. 2008. Phase-field simulation of weld solidification microstructure in an al–cu alloy. *Modelling and Simulation in Materials Science and Engineering* 16(6):065005.

Fayazfar, Haniyeh, Mehrnaz Salarian, Allan Rogalsky, Dyuti Sarker, Paola Russo, Vlad Paserin, and Ehsan Toyserkani. 2018. A critical review of powder-based additive manufacturing of ferrous alloys: Process parameters, microstructure and mechanical properties. *Materials & Design* 144: 98–128.

Feng, Xiaobing, and Andreas Prohl. 2004. Analysis of a fully discrete finite element method for the phase field model and approximation of its sharp interface limits. *Mathematics of computation* 73(246):541–567.

Fix, G. 1983. Phase field method for free boundary problems, in; free boundary problems, a. *Fasanao and M. Primicerio, eds., Pit-mann, London*.

Fox, Jason C, Shawn P Moylan, and Brandon M Lane. 2016. Effect of process parameters on the surface roughness of overhanging structures in laser powder bed fusion additive manufacturing. *Procedia Cirp* 45: 131–134.

Gan, Zhengtao, Orion L Kafka, Niranjan Parab, Cang Zhao, Lichao Fang, Olle Heinonen, Tao Sun, and Wing Kam Liu. 2021. Universal scaling laws of keyhole stability and porosity in 3d printing of metals. *Nature communications* 12(1):1–8.

Geng, Shaoning, Ping Jiang, Xinyu Shao, Gaoyang Mi, Han Wu, Yuewei Ai, Chunming Wang, Chu Han, Rong Chen, Wei Liu, et al. 2018. Effects of back-diffusion on solidification cracking susceptibility of al-mg alloys during welding: A phase-field study. *Acta Materialia* 160:85–96.

Ghosh, Supriyo, Li Ma, Nana Ofori-Opoku, and Jonathan E Guyer. 2017. On the primary spacing and microsegregation of cellular dendrites in laser deposited ni–nb alloys. *Modelling and simulation in materials science and engineering* 25(6):065002.

Gibou, Frédéric, Ronald Fedkiw, Russel Caflisch, and Stanley Osher. 2003. A level set approach for the numerical simulation of dendritic growth. *Journal of Scientific Computing* 19(1):183–199.

Gibson, Ian, David W Rosen, Brent Stucker, and Mahyar Khorasani. 2021. *Additive manufacturing technologies*, vol. 17. Springer.

Gong, Xibing, and Kevin Chou. 2015. Phase-field modeling of microstructure evolution in electron beam additive manufacturing. *Jom* 67(5):1176–1182.

Gonzalez-Ferreiro, B, Héctor Gómez, and Ignacio Romero. 2014. A thermodynamically consistent numerical method for a phase field model of solidification. *Communications in Nonlinear Science and Numerical Simulation* 19(7):2309–2323.

Gulati, Rahul, and Shiva Rudraraju. 2022. Spatio-temporal modeling of saltatory conduction in neurons using poisson-nernst–planck treatment and estimation of conduction velocity. *Brain Multiphysics*.

Gusarov, AV, I Yadroitsev, Ph Bertrand, and I Smurov. 2007. Heat transfer modelling and stability analysis of selective laser melting. *Applied Surface Science* 254(4):975–979.

Hellawell, A, Shan Liu, and SZ Lu. 1997. Dendrite fragmentation and the effects of fluid flow in castings. *Jom* 49(3):18–20.

Hu, Xianliang, Ruo Li, and Tao Tang. 2009. A multi-mesh adaptive finite element approximation to phase field models. *Communications in Computational Physics* 5(5):1012–1029.

Huang, Yong, Ming C Leu, Jyoti Mazumder, and Alkan Donmez. 2015. Additive manufacturing: current state, future potential, gaps and needs, and recommendations. *Journal of Manufacturing Science and Engineering* 137(1).

Hughes, Thomas JR. 2012. *The finite element method: linear static and dynamic finite element analysis*. Courier Corporation.

Islam, Zahabul, Ankur Kumar Agrawal, Behzad Rankouhi, Collin Magnin, Mark H Anderson, Frank E Pfefferkorn, and Dan J Thoma. 2022.

A high-throughput method to define additive manufacturing process parameters: Application to haynes 282. *Metallurgical and Materials Transactions A* 53(1):250–263.

Jiang, Tonghu, Shiva Rudraraju, Anindya Roy, Anton Van der Ven, Krishna Garikipati, and Michael L Falk. 2016. Multiphysics simulations of lithiation-induced stress in $li_{1+x}ti_2o_4$ electrode particles. *The Journal of Physical Chemistry C* 120(49):27871–27881.

Karma, Alain. 2001. Phase-field formulation for quantitative modeling of alloy solidification. *Physical Review Letters* 87(11):115701.

Karma, Alain, and Wouter-Jan Rappel. 1996. Phase-field method for computationally efficient modeling of solidification with arbitrary interface kinetics. *Physical review E* 53(4):R3017.

———. 1998. Quantitative phase-field modeling of dendritic growth in two and three dimensions. *Physical review E* 57(4):4323.

———. 1999. Phase-field model of dendritic sidebranching with thermal noise. *Physical review E* 60(4):3614.

Keller, Trevor, Greta Lindwall, Supriyo Ghosh, Li Ma, Brandon M Lane, Fan Zhang, Ursula R Kattner, Eric A Lass, Jarred C Heigel, Yaakov Idell, et al. 2017. Application of finite element, phase-field, and calphad-based methods to additive manufacturing of ni-based superalloys. *Acta materialia* 139:244–253.

Keshavarzkermani, Ali, Ehsan Marzbanrad, Reza Esmaeilizadeh, Yahya Mahmoodkhani, Usman Ali, Pablo D Enrique, Norman Y Zhou, Ali Bonakdar, and Ehsan Toyserkani. 2019. An investigation into the effect of process parameters on melt pool geometry, cell spacing, and grain refinement during laser powder bed fusion. *Optics & Laser Technology* 116:83–91.

Kessler, Daniel, and J-F Scheid. 2002. A priori error estimates of a finite-element method for an isothermal phase-field model related to the solidification process of a binary alloy. *IMA journal of numerical analysis* 22(2): 281–305.

Khairallah, Saad A, and Andy Anderson. 2014. Mesoscopic simulation model of selective laser melting of stainless steel powder. *Journal of Materials Processing Technology* 214(11):2627–2636.

King, Wayne E, Andrew T Anderson, Robert M Ferencz, Neil E Hodge, Chandrika Kamath, Saad A Khairallah, and Alexander M Rubenchik. 2015. Laser powder bed fusion additive manufacturing of metals; physics, computational, and materials challenges. *Applied Physics Reviews* 2(4): 041304.

Kobayashi, Ryo. 1993. Modeling and numerical simulations of dendritic crystal growth. *Physica D: Nonlinear Phenomena* 63(3-4):410–423.

Konda Gokuldoss, Prashanth, Sri Kolla, and Jürgen Eckert. 2017. Additive manufacturing processes: Selective laser melting, electron beam melting and binder jetting—selection guidelines. *materials* 10(6):672.

Kumar, Amitesh, and Subhransu Roy. 2009. Effect of three-dimensional melt pool convection on process characteristics during laser cladding. *Computational Materials Science* 46(2):495–506.

Letenneur, Morgan, Alena Kreitcberg, and Vladimir Brailovski. 2019. Optimization of laser powder bed fusion processing using a combination of melt pool modeling and design of experiment approaches: Density control. *Journal of Manufacturing and Materials Processing* 3(1):21.

Liu, Xiangbo, Fengye Tang, Wenyong Zhao, Jiasi Cai, and Yanhong Wei. 2022. Multi-phase field lattice boltzmann model of columnar-to-equiaxed

transition in entire welding molten pool. *Computational Materials Science* 204:111182.

Loginova, Irina, Gustav Amberg, and John Ågren. 2001. Phase-field simulations of non-isothermal binary alloy solidification. *Acta materialia* 49(4):573–581.

Lu, Shanping, Hidetoshi Fujii, and Kiyoshi Nogi. 2004. Sensitivity of marangoni convection and weld shape variations to welding parameters in o2–ar shielded gta welding. *Scripta Materialia* 51(3):271–277.

Makoana, Nkutwane Washington, Ina Yadroitsava, Heinrich Möller, and Igor Yadroitsev. 2018. Characterization of 17-4ph single tracks produced at different parametric conditions towards increased productivity of lpbf systems—the effect of laser power and spot size upscaling. *Metals* 8(7): 475.

Marshall, Guillermo. 1986. A front tracking method for one-dimensional moving boundary problems. *SIAM journal on scientific and Statistical Computing* 7(1):252–263.

Meyer, Gunter H. 1978. The numerical solution of stefan problems with front-tracking and smoothing methods. *Applied Mathematics and Computation* 4(4):283–306.

Min, Zhixian, Jun Shen, Zhourong Feng, Lingshui Wang, Lei Wang, and Hengzhi Fu. 2011. Effects of melt flow on the primary dendrite spacing of pb–sn binary alloy during directional solidification. *Journal of crystal growth* 320(1):41–45.

Mirihanage, Wajira U, Lars Arnberg, and Ragnvald H Mathiesen. 2012. In-situ observation of transient columnar dendrite growth in the presence of thermo-solutal convection. In *Iop conference series: Materials science and engineering*, vol. 33, 012033. IOP Publishing.

Mirkoohi, Elham, Jinqiang Ning, Peter Bocchini, Omar Fergani, Kuo-Ning Chiang, and Steven Y Liang. 2018. Thermal modeling of temperature distribution in metal additive manufacturing considering effects of build layers, latent heat, and temperature-sensitivity of material properties. *Journal of Manufacturing and Materials Processing* 2(3):63.

Mirkoohi, Elham, Daniel E Seivers, Hamid Garmestani, and Steven Y Liang. 2019. Heat source modeling in selective laser melting. *Materials* 12(13):2052.

Mohammadpour, Pardis, Alex Plotkowski, and Andre B Phillion. 2020. Revisiting solidification microstructure selection maps in the frame of additive manufacturing. *Additive Manufacturing* 31:100936.

Mondal, Sudeepta, Daniel Gwynn, Asok Ray, and Amrita Basak. 2020. Investigation of melt pool geometry control in additive manufacturing using hybrid modeling. *Metals* 10(5):683.

Mukherjee, T, V Manvatkar, A De, and T DebRoy. 2017. Dimensionless numbers in additive manufacturing. *Journal of Applied Physics* 121(6): 064904.

Mukherjee, T, HL Wei, A De, and Tarasankar DebRoy. 2018. Heat and fluid flow in additive manufacturing—part i: Modeling of powder bed fusion. *Computational Materials Science* 150:304–313.

Murakami, K, T Fujiyama, A Koike, and T Okamoto. 1983. Influence of melt flow on the growth directions of columnar grains and columnar dendrites. *Acta Metallurgica* 31(9):1425–1432.

N. Collier, V.M. Calo, L. Dalcin. 2013. PetIGA: High-performance isogeometric analysis. *arxiv* (1305.4452). Http://arxiv.org/abs/1305.4452.

Nabavizadeh, Seyed Amin, Mohsen Eshraghi, Sergio D Felicelli, Surendra N Tewari, and Richard N Grugel. 2020. The marangoni convection

effects on directional dendritic solidification. *Heat and Mass Transfer* 56: 1329–1341.

Neumann-Heyme, Hieram. 2017. Phase-field modeling of solidification and coarsening effects in dendrite morphology evolution and fragmentation. Ph.D. thesis, Technical University of Dresden, Dresden, Technical University of Dresden, Dresden. An optional note.

Ning, Fuda, Weilong Cong, Yingbin Hu, and Hui Wang. 2017. Additive manufacturing of carbon fiber-reinforced plastic composites using fused deposition modeling: Effects of process parameters on tensile properties. *Journal of Composite Materials* 51(4):451–462.

Noh, Jihun, Jinhwan Lee, Yejun Seo, Seongi Hong, Young-Sam Kwon, and Dongsik Kim. 2022. Dimensionless parameters to define process windows of selective laser melting process to fabricate three-dimensional metal structures. *Optics & Laser Technology* 149:107880.

Ohno, Munekazu, and Kiyotaka Matsuura. 2009. Quantitative phase-field modeling for dilute alloy solidification involving diffusion in the solid. *Physical Review E* 79(3):031603.

Plapp, Mathis, and Alain Karma. 2000. Multiscale finite-difference-diffusion-monte-carlo method for simulating dendritic solidification. *Journal of Computational Physics* 165(2):592–619.

Qian, MA, Wei Xu, Milan Brandt, and HP Tang. 2016. Additive manufacturing and postprocessing of ti-6al-4v for superior mechanical properties. *Mrs Bulletin* 41(10):775–784.

Ramirez, JC, C Beckermann, As Karma, and H-J Diepers. 2004. Phase-field modeling of binary alloy solidification with coupled heat and solute diffusion. *Physical Review E* 69(5):051607.

Rankouhi, B, KM Bertsch, G Meric de Bellefon, M Thevamaran, DJ Thoma, and K Suresh. 2020. Experimental validation and microstructure characterization of topology optimized, additively manufactured ss316l components. *Materials Science and Engineering: A* 776:139050.

Rankouhi, Behzad, Ankur Kumar Agrawal, Frank E Pfefferkorn, and Dan J Thoma. 2021. A dimensionless number for predicting universal processing parameter boundaries in metal powder bed additive manufacturing. *Manufacturing Letters* 27:13–17.

Rappaz, M, SA David, JM Vitek, and LA Boatner. 1990. Analysis of solidification microstructures in fe-ni-cr single-crystal welds. *Metallurgical transactions A* 21(6):1767–1782.

Rátkai, László, Tamás Pusztai, and László Gránásy. 2019. Phase-field lattice boltzmann model for dendrites growing and moving in melt flow. *npj Computational Materials* 5(1):113.

Ren, Jian-kun, Yun Chen, Yan-fei Cao, Ming-yue Sun, Bin Xu, and Dianzhong Li. 2020. Modeling motion and growth of multiple dendrites during solidification based on vector-valued phase field and two-phase flow models. *Journal of Materials Science & Technology* 58:171–187.

Rittinghaus, Silja-Katharina, Eric A Jägle, Manfred Schmid, and Bilal Gökce. 2022. New frontiers in materials design for laser additive manufacturing.

Robert, A, and T Debroy. 2001. Geometry of laser spot welds from dimensionless numbers. *Metallurgical and materials transactions B* 32(5):941–947.

Rojas, Roberto, Tomohiro Takaki, and Munekazu Ohno. 2015. A phase-field-lattice boltzmann method for modeling motion and growth of a dendrite for binary alloy solidification in the presence of melt convection. *Journal of Computational Physics* 298:29–40.

Rolchigo, Matthew R, Michael Y Mendoza, Peyman Samimi, David A Brice, Brian Martin, Peter C Collins, and Richard LeSar. 2017. Modeling of ti-w solidification microstructures under additive manufacturing conditions. *Metallurgical and Materials Transactions A* 48(7):3606–3622.

Rosam, Jan, Peter K Jimack, and Andy Mullis. 2007. A fully implicit, fully adaptive time and space discretisation method for phase-field simulation of binary alloy solidification. *Journal of Computational Physics* 225(2):1271–1287.

Rubinstein, L.I. 1971. The stefan problem, transl. math. *Monographs* 27: 327–3.

Rudraraju, Shiva, Derek E Moulton, Régis Chirat, Alain Goriely, and Krishna Garikipati. 2019. A computational framework for the morpho-elastic development of molluskan shells by surface and volume growth. *PLoS computational biology* 15(7):e1007213.

Ruzicka, MC. 2008. On dimensionless numbers. *Chemical Engineering Research and Design* 86(8):835–868.

Sahoo, Seshadev, and Kevin Chou. 2016. Phase-field simulation of microstructure evolution of ti–6al–4v in electron beam additive manufacturing process. *Additive manufacturing* 9:14–24.

Shen, Hongyao, Jinwen Yan, and Xiaomiao Niu. 2020. Thermo-fluid-dynamic modeling of the melt pool during selective laser melting for az91d magnesium alloy. *Materials* 13(18):4157.

Shevchenko, Natalia, O Roshchupkina, O Sokolova, and S Eckert. 2015. The effect of natural and forced melt convection on dendritic solidification in ga–in alloys. *Journal of Crystal Growth* 417:1–8.

Slavov, Vladimir, Stefka Dimova, and Oleg Iliev. 2003. Phase-field method for 2d dendritic growth. In *International conference on large-scale scientific computing*, 404–411. Springer.

Takaki, Tomohiro, Munekazu Ohno, Takashi Shimokawabe, and Takayuki Aoki. 2014. Two-dimensional phase-field simulations of dendrite competitive growth during the directional solidification of a binary alloy bicrystal. *Acta Materialia* 81:272–283.

Takaki, Tomohiro, Ryotaro Sato, Roberto Rojas, Munekazu Ohno, and Yasushi Shibuta. 2018. Phase-field lattice boltzmann simulations of multiple dendrite growth with motion, collision, and coalescence and subsequent grain growth. *Computational Materials Science* 147:124–131.

Thoma, DJ, C Charbon, GK Lewis, and RB Nemec. 1995. Directed light fabrication of iron-based materials. *MRS Online Proceedings Library Archive* 397.

Tourret, Damien, and Alain Karma. 2015. Growth competition of columnar dendritic grains: A phase-field study. *Acta Materialia* 82:64–83.

Tourret, Damien, Hong Liu, and Javier LLorca. 2022. Phase-field modeling of microstructure evolution: Recent applications, perspectives and challenges. *Progress in Materials Science* 123:100810.

Van Elsen, Maarten, Farid Al-Bender, and Jean-Pierre Kruth. 2008. Application of dimensional analysis to selective laser melting. *Rapid Prototyping Journal*.

Wang, CY, and Ch Beckermann. 1996. Equiaxed dendritic solidification with convection: Part i. multiscale/multiphase modeling. *Metallurgical and materials transactions A* 27:2754–2764.

Wang, X, PW Liu, Y Ji, Y Liu, MH Horstemeyer, and L Chen. 2019a. Investigation on microsegregation of in718 alloy during additive manufacturing via integrated phase-field and finite-element modeling. *Journal of Materials Engineering and Performance* 28(2):657–665.

Wang, Y Morris, Thomas Voisin, Joseph T McKeown, Jianchao Ye, Nicholas P Calta, Zan Li, Zhi Zeng, Yin Zhang, Wen Chen, Tien Tran Roehling, et al. 2018. Additively manufactured hierarchical stainless steels with high strength and ductility. *Nature materials* 17(1):63–71.

Wang, Zekun, and Moubin Liu. 2019. Dimensionless analysis on selective laser melting to predict porosity and track morphology. *Journal of Materials Processing Technology* 273:116238.

Wang, Zekun, Wentao Yan, Wing Kam Liu, and Moubin Liu. 2019b. Powder-scale multi-physics modeling of multi-layer multi-track selective laser melting with sharp interface capturing method. *Computational Mechanics* 63(4):649–661.

Wang, Zhenlin, Shiva Rudraraju, and Krishna Garikipati. 2016. A three dimensional field formulation, and isogeometric solutions to point and line defects using toupin's theory of gradient elasticity at finite strains. *Journal of the Mechanics and Physics of Solids* 94:336–361.

Wang, Zhijun, Junjie Li, Jincheng Wang, and Yaohe Zhou. 2012. Phase field modeling the selection mechanism of primary dendritic spacing in directional solidification. *Acta Materialia* 60(5):1957–1964.

Warren, James A, and William J Boettinger. 1995. Prediction of dendritic growth and microsegregation patterns in a binary alloy using the phase-field method. *Acta Metallurgica et Materialia* 43(2):689–703.

Weaver, Jordan S, Jarred C Heigel, and Brandon M Lane. 2022. Laser spot size and scaling laws for laser beam additive manufacturing. *Journal of Manufacturing Processes* 73:26–39.

Wei, PS, CN Ting, JS Yeh, Tarasankar DebRoy, FK Chung, and GH Yan. 2009. Origin of wavy weld boundary. *Journal of Applied Physics* 105(5): 053508.

Wesner, Eugenia, Abhik Choudhury, Anastasia August, Marco Berghoff, and Britta Nestler. 2012. A phase-field study of large-scale dendrite fragmentation in al–cu. *Journal of Crystal Growth* 359:107–121.

Wu, Jiahzu, Xiaoqiang Zheng, Yi Zhang, Song Ren, Cunhong Yin, Yang Cao, and Dabin Zhang. 2022. Modeling of whole-phase heat transport in laser-based directed energy deposition with multichannel coaxial powder feeding. *Additive Manufacturing* 59:103161.

Yang, Xiaoshan, Jinna Liu, Xiufang Cui, Guo Jin, Zhe Liu, Yanbo Chen, and Xiangru Feng. 2019. Effect of remelting on microstructure and magnetic properties of fe-co-based alloys produced by laser additive manufacturing. *Journal of Physics and Chemistry of Solids* 130:210–216.

Yarin, Leonid P. 2012. *The pi-theorem: applications to fluid mechanics and heat and mass transfer*, vol. 1. Springer Science & Business Media.

Yasuda, Hideyuki, Kohei Morishita, Noriaki Nakatsuka, Tomohiro Nishimura, Masato Yoshiya, Akira Sugiyama, Kentaro Uesugi, and Akihisa Takeuchi. 2019. Dendrite fragmentation induced by massive-like δ–γ transformation in fe–c alloys. *Nature communications* 10(1):3183.

Yuan, Lang, and Peter D Lee. 2010. Dendritic solidification under natural and forced convection in binary alloys: 2d versus 3d simulation. *Modelling and simulation in Materials Science and Engineering* 18(5):055008.

Yuan, T, Z Luo, and S Kou. 2016. Grain refining of magnesium welds by arc oscillation. *Acta Materialia* 116:166–176.

Yue, Chen, Shaoning Geng, Lingyu Guo, Chu Han, and Ping Jiang. 2022. Dendrite remelting during arc oscillation welding of magnesium alloys: A phase-field study. *Applied Physics A* 128(5):437.

Zhang, Qingyu, Hui Fang, Hua Xue, Shiyan Pan, Markus Rettenmayr, and Mingfang Zhu. 2017. Interaction of local solidification and remelting during dendrite coarsening-modeling and comparison with experiments. *Scientific Reports* 7(1):17809.

Zhu, Chang-sheng, Sheng Xu, Li Feng, Dan Han, and Kai-ming Wang. 2019. Phase-field model simulations of alloy directional solidification and seaweed-like microstructure evolution based on adaptive finite element method. *Computational Materials Science* 160:53–61.